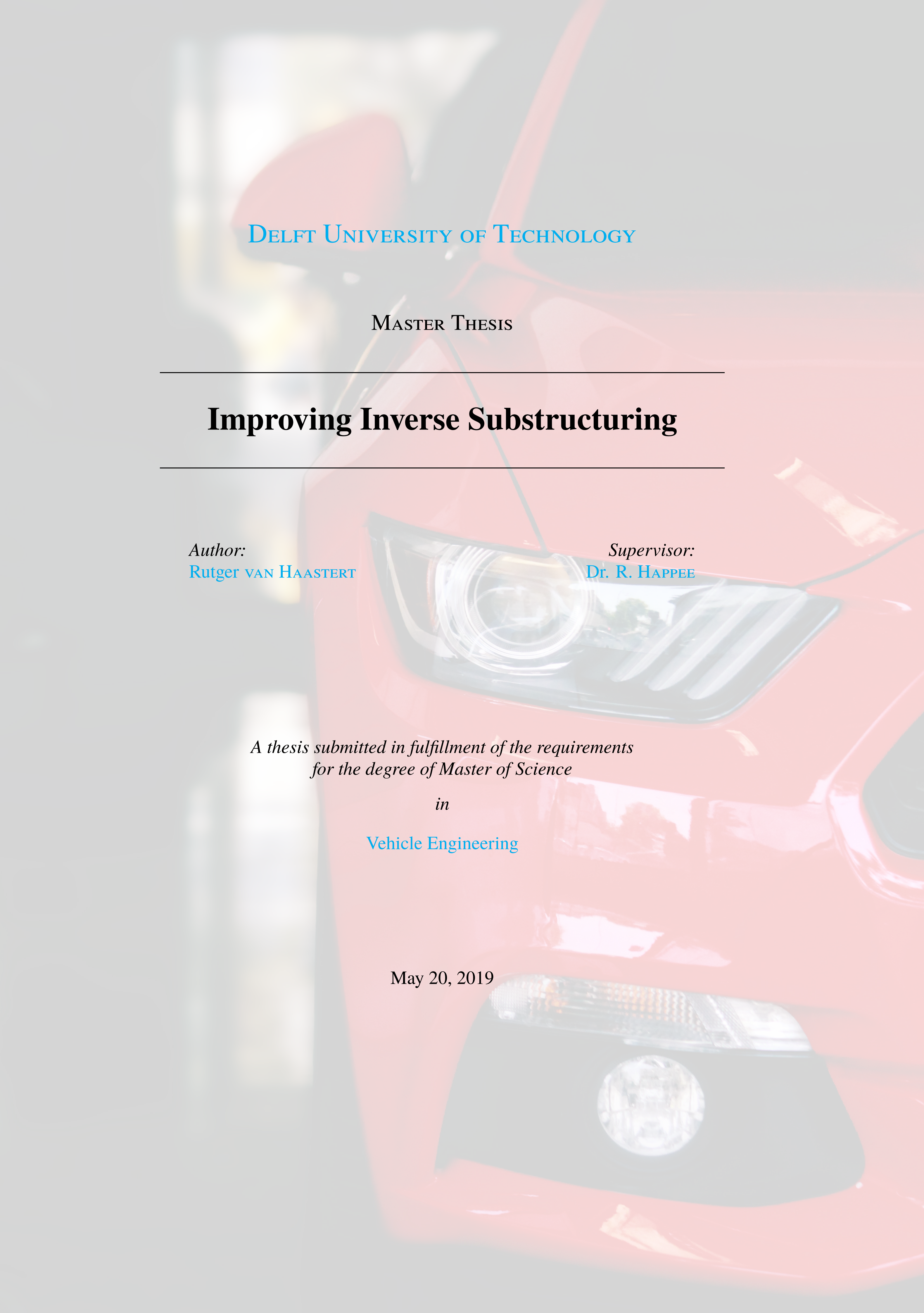

DELFT UNIVERSITY OF TECHNOLOGY

MASTER THESIS

---

# Improving Inverse Substructuring

---

*Author:*
Rutger VAN HAASTERT

*Supervisor:*
Dr. R. HAPPEE

*A thesis submitted in fulfillment of the requirements*
*for the degree of Master of Science*

*in*

Vehicle Engineering

May 20, 2019

“*If you want to find the secrets of the universe, think in terms of energy, frequency and vibration.* ”

Nikola Tesla

DELFT UNIVERSITY OF TECHNOLOGY

# *Abstract*

Mechanical, Maritime and Materials Engineering
Vehicle Engineering

Master of Science

**Improving Inverse Substructuring**

by Rutger van Haastert

The electrification of drive trains in current and next generation vehicles require vibration dampers that possess different dynamic properties than its internal combustion engine counterparts. This makes research in automotive vibration damping a hot topic. Research in this field often contains the practice of Frequency Based Substructuring (FBS) in which dynamics of individual components can be used to predict dynamics of an assembly or vice versa. A method to incorporate vibration dampers in FBS is the practice of Full Decoupling but this can be a time consuming and cumbersome exercise so the alternative method of Inverse Substructuring was developed. This approach is quicker and simpler but suffers from shortcomings as underestimating stiffness and neglecting some DoF relations. In this thesis an improvement on this technique is proposed by making use of the geometrical shape of the vibration isolator. This results in better prediction of the dynamics of the vibration isolator in most directions however the dynamicist should make a decision if this simpler method of Improved Inverse Substructuring is more suitable for the application over Full Decoupling.

# *Acknowledgements*

A little over a year ago I was searching for a graduation project to finish my master studies in vehicle engineering at TU Delft. During a coffee break with a friend we were discussing possibilities and he mentioned Maarten van der Seijs (a friend of his) as one of the founders of a company in automotive technology. Two emails later I visited this company, VIBES.Technology, and was welcomed to work on a project for the coming year. My daily supervisor at VIBES became Eric Pasma, a guy I already came across a few times during my studies. A project topic was chosen and I started this journey in the realm of experimental dynamics.

The process of graduating can be seen as a bike race and as a bike racer myself I know that winning a race cannot be done alone. Along the route signallers are required to keep you on track and if you have a flat tire your mechanic provides a spare wheel. Team-mates protect you from the wind and the Director Sportif gives you advice on tactical decisions. However the climbing of mountains must be done alone, and there were some hills along this course.

Luckily I finished the race but I could not have done it without my signallers Maarten (2x), Dennis, Daniel, Julie, Steven, Michael and Hilde. Also the mechanics Henri, Mathieu, Mahmoud and Jelle provided me with the tools that made my race much more enjoyable. Sometimes a bike race is miserable and shared misery is half misery so I am very glad I had team-mates in the same race to share this with: Tom, Thom, Wouter and Nooshin. Lastly, the Director Sportif Eric deserves a big thank you for providing the tactics for tackling this race.

# Contents

**Abstract** **5**

**1 Introduction** **15**

**2 Theory** **17**

2.1 What, why and how . . . . . 17

2.1.1 What: Dynamic stiffness . . . . . 17

2.1.2 Why: Electrification of the drive train . . . . . 18

2.1.3 How: experimental testing . . . . . 18

2.2 Constructing FRFs from impact testing . . . . . 19

2.2.1 Practical considerations . . . . . 20

2.3 Experimental Dynamic Substructuring . . . . . 20

2.3.1 Frequency based substructuring . . . . . 22

Primal assembly . . . . . 22

Dual assembly . . . . . 23

The use of EDS/FBS on resilient elements . . . . . 25

2.3.2 Interface modelling . . . . . 25

Brief history . . . . . 26

State of the art: Virtual Point transformation . . . . . 26

2.4 State of the art methods in EDS . . . . . 28

2.4.1 Full decoupling . . . . . 28

2.4.2 Inverse substructuring . . . . . 30

Assumption 1: The isolator has negligible mass . . . . . 30

Assumption 2: The structure is coupled in a special topology . . . . . 31

2.5 Proposition on improvement on inverse substructuring . . . . . 32

2.5.1 Proposition for including crosscouplings . . . . . 33

2.5.2 Proposition for including Isolator Mass . . . . . 35

**3 Example** **37**

3.1 A simple system . . . . . 37

3.1.1 Varying Mass . . . . . 39

Observation . . . . . 39

Explanation . . . . . 40

3.1.2 Varying Stiffness . . . . . 40

Observation . . . . . 40

Explanation . . . . . 41

3.1.3 Varying Loss Factor . . . . . 41

Observation . . . . . 41

Explanation . . . . . 41

3.1.4 Summary . . . . . 42

3.2 Dynamic substructuring: Full Decoupling and Inverse Substructuring . . . . . 42

Full Decoupling . . . . . 42

Inverse substructuring . . . . . 43

3.2.1 Axial stiffness . . . . . . . . . . . . . . . . . . . . . . . . . . . . 43
Observation . . . . . . . . . . . . . . . . . . . . . . . . . . . . 43
Explanation . . . . . . . . . . . . . . . . . . . . . . . . . . . . 44
3.3 Adding mass to the isolator . . . . . . . . . . . . . . . . . . . . . . . . 44
3.3.1 Varying mass ratio for transfer receptance . . . . . . . . . . . . 46
Observation . . . . . . . . . . . . . . . . . . . . . . . . . . . . 46
Explanation . . . . . . . . . . . . . . . . . . . . . . . . . . . . 46
3.3.2 Varying mass ratio for driving point receptance . . . . . . . . . . 47
Observation . . . . . . . . . . . . . . . . . . . . . . . . . . . . 47
Explanation . . . . . . . . . . . . . . . . . . . . . . . . . . . . 47

**4 Practice 49**
4.1 Introduction . . . . . . . . . . . . . . . . . . . . . . . . . . . . . . . 49
4.2 Measuring the dynamic properties of the Isolator . . . . . . . . . . . . . 49
4.2.1 General setup . . . . . . . . . . . . . . . . . . . . . . . . . . . 49
4.2.2 Used materials . . . . . . . . . . . . . . . . . . . . . . . . . . . 50
4.2.3 Campaign 1: Dynamic stiffness of the crosses . . . . . . . . . . . . 51
4.2.4 Campaign 2: Roving measurement of the isolator . . . . . . . . . . 51
4.2.5 Campaign 3: Dynamics of the A structure . . . . . . . . . . . . . . 52
4.2.6 Campaign 4: Measurement of the validation structure . . . . . . . . 52
4.3 Data Processing . . . . . . . . . . . . . . . . . . . . . . . . . . . . . . 53
4.4 Results . . . . . . . . . . . . . . . . . . . . . . . . . . . . . . . . . . 55
4.4.1 Dynamics of the Transmission Simulators . . . . . . . . . . . . . . 55
4.4.2 Dynamics of the rubber vibration isolator . . . . . . . . . . . . . . 55
4.4.3 Dynamics of the A-structure . . . . . . . . . . . . . . . . . . . . . 57
4.4.4 Comparing FD, InvSub, and ImInvSub to a validation measurement . 58
4.4.5 Observations for translational input in x and y direction . . . . . . . . 59
Inverse substructuring overestimates accelerance . . . . . . . . . . . 60
Missing dynamics in substructuring . . . . . . . . . . . . . . . . . . 60
Resonance peak shifts of inverse substructuring . . . . . . . . . . . . 61
Dynamics solely found in ImInvSub . . . . . . . . . . . . . . . . . . 61
Differences for low frequencies . . . . . . . . . . . . . . . . . . . . 61
4.4.6 Observations for translational input in z direction . . . . . . . . . . . 62
Inaccurate results for substructuring . . . . . . . . . . . . . . . . . . 62
4.4.7 Observations for rotational input . . . . . . . . . . . . . . . . . . . 63
Inverse Substructuring overestimates accelerance response in x and y direction . . . . . . . . . . . . . . . . . . . . . . 64
Improved Inverse Substructuring over estimates accelerance response in z direction . . . . . . . . . . . . . . . . . . . . . 64
4.5 Discussion . . . . . . . . . . . . . . . . . . . . . . . . . . . . . . . . . 65
4.5.1 Practical . . . . . . . . . . . . . . . . . . . . . . . . . . . . . . . 65
Imperfect impacts . . . . . . . . . . . . . . . . . . . . . . . . . . . 65
Imperfect sensor mounting . . . . . . . . . . . . . . . . . . . . . . . 65
Bookkeeping errors . . . . . . . . . . . . . . . . . . . . . . . . . . . 66
Physical connection between substructures . . . . . . . . . . . . . . 66
Stiffness of sensor mounting . . . . . . . . . . . . . . . . . . . . . . 66
Influence of sensor cables . . . . . . . . . . . . . . . . . . . . . . . 67
Suspension of the object for testing . . . . . . . . . . . . . . . . . . 67
4.5.2 Theoretical . . . . . . . . . . . . . . . . . . . . . . . . . . . . . . 67
Virtual point: Sensor consistency . . . . . . . . . . . . . . . . . . . 67
Virtual point: Impact consistency . . . . . . . . . . . . . . . . . . . 68

Virtual point: Rigid transformation matrices . . . 68
Nonlinearity of the rubber material . . . 68
Repeating the experiment . . . 68
Signal to noise ratio for low frequencies . . . 68
Matrix inversions on experimental data . . . 69
Different shapes of isolators . . . 69

**5 Conclusions 71**
5.1 Improved Inverse Substructuring does improve the prediction of coupled dynamics in most directions over Inverse Substructuring . . . 71
5.2 ImInvSub can only be implemented with care . . . 71

**A Properties and modelling of Rubber 73**
A.1 Properties and modelling of Rubber . . . 73
A.1.1 A brief history . . . 73
A.1.2 Strain rate dependent stiffness . . . 74
A.1.3 Non linear stress-strain relation . . . 74
A.1.4 Effects of temperature and frequency . . . 74
A.1.5 Stress softening . . . 75
A.1.6 Viscoelastic models . . . 76
The complex modulus model . . . 76
Spring-dash pot representation . . . 77
A.1.7 Hyperelastic models . . . 78

**B Construction of the 12x12 FRF matrix 81**

# Symbols and Abbreviations

| | |
|---|---|
| $\mathbf{B}$ | signed Boolean matrix |
| $\mathbf{C}$ | viscous damping matrix |
| $\mathbf{f}$ | applied forces |
| $\mathbf{g}$ | interface forces/moments |
| $\mathbf{K}$ | stiffness matrix |
| $\mathbf{L}$ | Boolean localisation matrix |
| $\mathbf{m}$ | generalised/virtual point loads |
| $\mathbf{M}$ | mass matrix |
| $\mathbf{q}$ | generalised/virtual point motion |
| $\mathbf{R}$ | modal reduction/IDM matrix |
| $t$ | time |
| $\mathbf{T}$ | virtual point transformation matrix |
| $\mathbf{u}$ | dynamic displacements/rotations |
| $\mathbf{Y}$ | admittance FRF matrix |
| $\mathbf{Z}$ | impedance matrix |
| $\mathbf{0}/\mathbf{I}$ | null/identity matrix |

| | |
|---|---|
| **CAE** | **C**omputer-**A**ided **E**ngineering |
| **DAS** | **D**ata **A**cquisition **S**ystem |
| **DoF** | **D**egree **o**f **F**reedom |
| **DS** | **D**ynamic **S**ubstructuring |
| **FBS** | **F**requency **B**ased **S**ubstructuring |
| **FE** | **F**inite **E**lement |
| **FD** | **F**ull **D**ecoupling |
| **FRF** | **F**requency **R**esponse **F**unction |
| **IDM** | **I**nterface **D**isplacement **M**ode |
| **InvSub** | **Inv**erse **Sub**structuring |
| **ImInvSub** | **Im**proved **Inv**erse **Sub**structuring |
| **IRF** | **I**mpulse **R**esponse **F**unction |
| **ICE** | **I**nternal **C**ombustion **E**ngine |
| **ICE** | **I**nverse Substructuring |
| **NVH** | **N**oise **V**ibration (and) **H**arshness |
| **VP** | **V**irtual **P**oint |

# Chapter 1

# Introduction

Vehicle costumers have an increasing expectation for luxury, which can set a vehicle ahead of its competition. Noise, vibration and harshness (NVH) have a strong influence on our perception of luxury, so it can be seen that vehicle manufacturers are very concerned with sound and vibration engineering. In NVH engineering, an engineer aims to tweak the sound of certain parts of a vehicle to the desired sounds. Often the endeavour of the NVH engineer is to remove unwanted noise and vibration. A way to isolate the vehicle costumer from unwanted vibrations is to dissipate the vibration energy before it reaches its senses and a way to achieve this is by making use of rubber vibration dampers between the vibration source and the driver. In this thesis, the focus is on determining the dynamic properties on rubber vibration dampers between the engine subframe and the chassis.

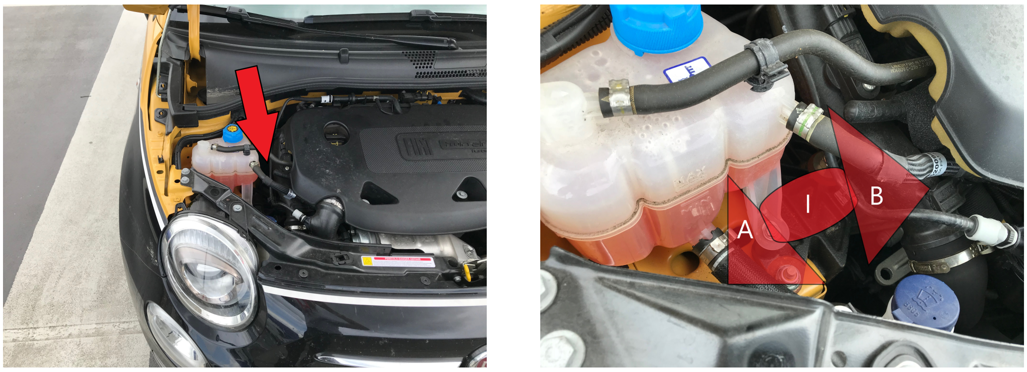

FIGURE 1.1: Location of rubber vibration damper in the vehicle. On the right: A is the chassis frame, B the engine subframe and I the isolator.

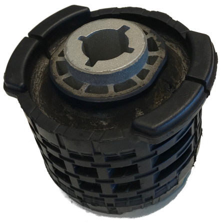

FIGURE 1.2: A rubber vibration isolator removed from the assembly.

Driven by the need for sustainable transportation, vehicles are shifting from internal combustion engines to electric alternatives. For NVH engineering, this has two consequences.

The first consequence is that noises previously masked by the ICE are now relatively louder. As a second consequence, one can say that electric engines produce more tonal vibrations in a higher frequency band, so vibration analysis for higher frequencies is required. This makes research on dynamic properties of rubber vibration dampers a hot topic.

As it turns out, determining dynamic properties in a higher frequency range is more challenging. New methods are still developed today and the state of the art relies on a combination of experimental dynamic substructuring techniques. The state of the art method does suffer from certain flaws, so a proposition for improving this method is made and tested in theory and practice.

# Chapter 2

# Theory

To improve the current state of the art methods in determining the dynamic properties on resilient elements, some theory needs to be mastered. Section 2.1 discusses what property this research aims to acquire, why this is important in this day and age and how this property can be obtained. In the following sections, key mathematical principles and practical considerations are discussed. Thereafter the current state of the are methods for determining dynamic properties are explained to conclude with a proposition on an improvement on the state of the art. This proposition will be validated in chapter 3 on computer models and in chapter 4 on a real life test case.

## 2.1 What, why and how

This section aims to answer the questions: What does one require to know of the resilient element, why is this research required and why is it now a hot topic and how is this required information obtained? The answers to these questions lie in the following subsections.

### 2.1.1 What: Dynamic stiffness

The interesting property of a vibration isolator is dynamic stiffness $\mathbf{Z}(\omega)$. The dynamic stiffness is a frequency dependent property that is built up from the physical properties of mass, stiffness and damping and by so it can relate a harmonic force to a displacement as seen in equation 2.2.

$$\mathbf{Z}(\omega) = -\omega^2\mathbf{M} + \omega\mathbf{C} + \mathbf{K} \tag{2.1}$$

With $\omega$ is frequency and $\mathbf{M}$, $\mathbf{C}$ and $\mathbf{K}$ the systems mass, damping and stiffness matrix respectively.

$$\mathbf{Z}(\omega) = \frac{\mathbf{f}(\omega)}{\mathbf{u}(\omega)} \tag{2.2}$$

To save dynamic stiffness information of a system containing multiple degrees of freedom, a matrix notation is used. For a 4 degree of freedom system, we denote the stiffness from node to node by the subscripts:

$$\mathbf{Z}(\omega) = \begin{bmatrix} Z_{11} & Z_{12} & Z_{13} & Z_{14} \\ Z_{21} & Z_{22} & Z_{23} & Z_{24} \\ Z_{31} & Z_{32} & Z_{33} & Z_{34} \\ Z_{41} & Z_{42} & Z_{43} & Z_{44} \end{bmatrix} \tag{2.3}$$

The dynamic stiffness values are determined per measured frequency point, so a 3D matrix emerges as shown in figure 2.1.

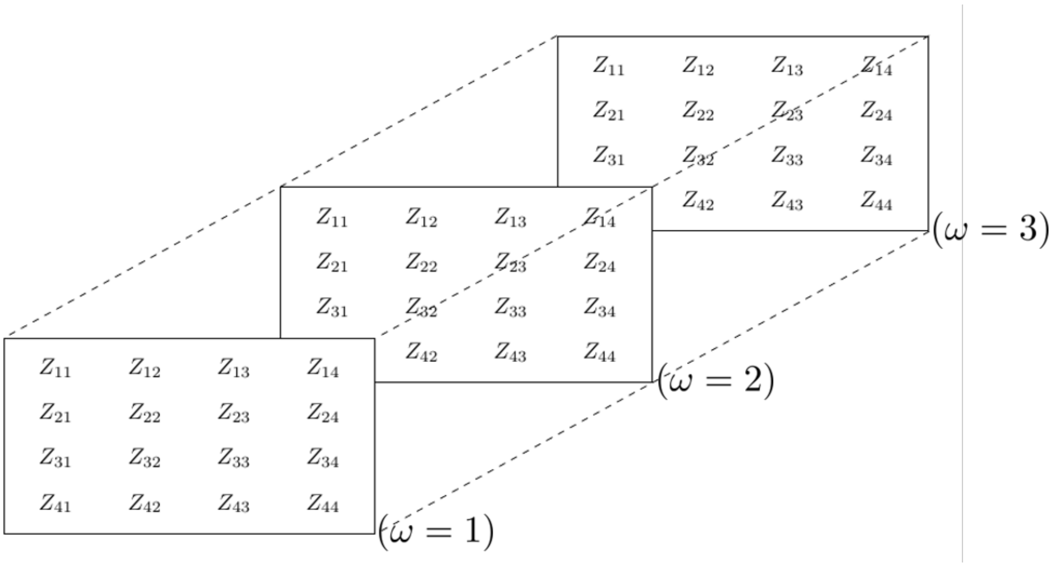
$Z_{11}$ $Z_{12}$ $Z_{13}$ $Z_{14}$
$Z_{21}$ $Z_{22}$ $Z_{23}$ $Z_{24}$
$Z_{31}$ $Z_{32}$ $Z_{33}$ $Z_{34}$
$Z_{41}$ $Z_{42}$ $Z_{43}$ $Z_{44}$
$(\omega = 1)$
$(\omega = 2)$
$(\omega = 3)$

FIGURE 2.1: The 3D stiffness matrix with the frequency dependency shown in in-paper-axis

### 2.1.2 Why: Electrification of the drive train

In recent years vehicles are shifting from the internal combustion engine (ICE) to electric alternatives. Not only are electric motors quieter in general but they also generate a very different sound and vibration. Due to the nature of the combustion, ICEs exhibit a pattern of harmonic orders and possess a natural frequency in the 50-200 Hertz range. Humans do not perceive this as unpleasant sound per se. In contrast, an electric engine create sounds and vibrations in the kiloHertz range with more fluent sine waves at odd harmonic rations which are generally perceived as very unpleasant. Due to this new type of vibrations, new measuring methods are developed. As it turns out, measuring dynamic properties gets more challenging in higher frequency regions so this is an active field of research today.

### 2.1.3 How: experimental testing

There exist two methods to acquire the dynamic stiffness **Z** of a structure: numerically and experimentally. Numerical analysis can be preferred in the case of running computer simulations of a measurement. To compute the dynamic stiffness, the system matrices **M**, **C** and **K** are used.

In the case of real life testing, experimental methods are often preferred. Two main methods can be distinguished which are separated by the requirements of the needed testing equipment. The first branch utilizes an electric or hydraulic shaker apparatus to excite the structure. The shaker apparatus is a device that can be set to excite the test object with a given amplitude and frequency. By measuring the response (in force or acceleration) of the test object, the dynamic stiffness can be computed. Two methods are the 'direct' and 'indirect' method [22].

By using a shaker for dynamic stiffness measurements, one has to consider some practical disadvantages:

- The frequency range is up to 300 Hz [22]. Measurements in the kHz range are not possible.

- Obtaining measurements in different directions is time consuming because for every direction the test object has to be removed from the measurement setup and placed in the correct position.
- The shaker apparatus is not infinite stiff which will influence the measurement.

The second branch utilizes an impact hammer to excite the structure. This overcomes the practical problems induced by the shaker but can only be used on light structures. Heavy structures need too much excitation energy to distinguish a measurement signal from noise, but in the application of measuring dynamic properties on resilient elements, the measurement setup is accepted as a light structure. In impact testing, one obtains the receptance matrix **Y**, often called the Frequency Response Function (FRF). This FRF relates the impact to the measured response as:

$$\mathbf{Y}(\omega) = \frac{\mathbf{u}(\omega)}{\mathbf{f}(\omega)} \tag{2.4}$$

In which **u** is the measured displacement and **f** is the exerted force by the tip of the impact hammer. As can be seen in equation 2.2, by simply inverting this FRF matrix, one obtains the dynamic stiffness matrix: $\mathbf{Y}(\omega)^{-1} = \mathbf{Z}(\omega)$. For detailed information on how to construct an FRF matrix from impact testing, consult section 2.2.

## 2.2 Constructing FRFs from impact testing

A Frequency Response Function (FRF) relates an excitation of a test structure to its response. In experimental impact testing, this means relating the impact of an impact hammer to a response of an accerelerometer. The force exerted by the impact hammer is measured by a load cell on the tip and the acceleration is measured by an accelerometer. If not accelerance but displacement is required, one is able to integrate accelerance twice in time to obtain displacement: $\iint \ddot{\mathbf{u}} = \mathbf{u}$.

The force and acceleration signals are routed to a data acquisition system (DAS). This DAS accepts the voltage versus time signals and performs spectral analysis to convert the time signal to the frequency domain by means of a Fourier transform. The results are send to a computer for further analysis and investigation. A typical measurement setup is depicted in figure 2.2.

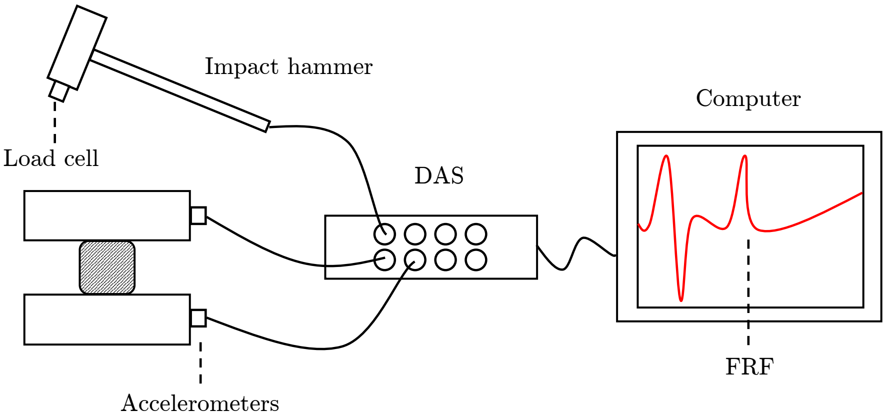

Figure 2.2: A typical measurement setup for determining FRFs of a test structure using impact testing.

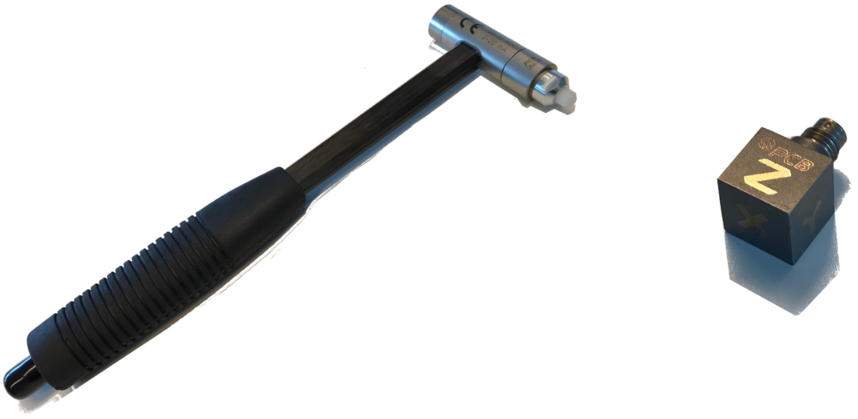

FIGURE 2.3: Left: an impact hammer with a load cell on the tip. Right: An accelerometer suited for adhering to a test structure.

As mentioned, this FRFs are stored in a matrix $\mathbf{Y}(\omega)$. This matrix contains as many rows as there are sensor channels (three channels per accelerometer for a triaxial unit) and as many columns as impacts. This matrix is three dimensional with on the third axis the response per frequency point. An example for a measurement with four impacts and four sensor channels is shown in figure 2.4.

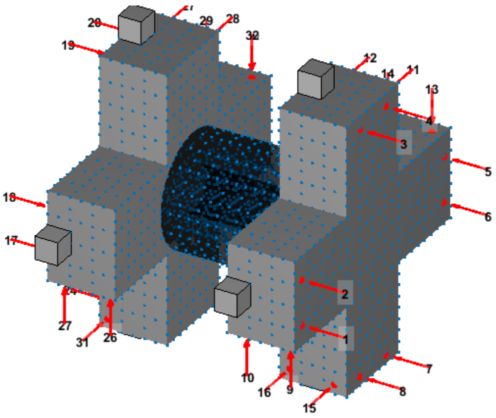

$$\mathbf{Y}(\omega) = \begin{array}{cc} & \text{Impacts} \longrightarrow \\ \Big\downarrow & \begin{bmatrix} Y_{11} & Y_{12} & Y_{13} & Y_{14} \\ Y_{21} & Y_{22} & \enclose{circle}{Y_{23}} & Y_{24} \\ Y_{31} & Y_{32} & Y_{33} & Y_{34} \\ Y_{41} & Y_{42} & Y_{43} & Y_{44} \end{bmatrix}_{(\omega)} \\ \text{Sensors} & \end{array}$$

FIGURE 2.4: The cubes on the structure are accelerometers. The red arrows are impacts by an impact hammer. For display purposes, just a 4 DoF FRF matrix is shown on the right, relating the impacts to sensors in the frequency domain. The circled value is the response of sensor(channel) 2 on impact 3.

### 2.2.1 Practical considerations

Because impact testing is handwork conducted by a human being, every impact is different. Also the sensors are placed by hand which can differ slightly from the intended place. In preparing a measurement some practical aspects need te be considered. These are discussed in section 4.5.

## 2.3 Experimental Dynamic Substructuring

Dynamic substructuring (DS) is a collection of techniques to perform dynamic analysis on systems by dividing these into subsystems. This approach has four advantages over handling an entire problem at once [8] [17]:

1. It allows evaluating the dynamic behaviour of structures that are too large or complex to be analysed as a whole.
2. By analysing the subsystems, local dynamic behaviour can be recognized more easily.
3. Subsystems can be modelled in the domain that is most appropriate.
4. Substructures models of different development groups can be shared and combined without exposing all modelling details

DS originates from the desire to analyse complex systems but being unable to because of limited resources. The problem is split into smaller problems of the separate components and its interfaces. The original idea of decomposing a complex problem can be brought back to around 100 BC when Emperor Julius Caesar used his famous divide and conquer technique to take power of the French part of Europe. However, for sake of scope of this document we stick to engineering applications. In that case, Schwarz [18] proposed a procedure based on domain decomposition in 1890. Domain composition in this context is the process of subdividing the solution of a large system into smaller problems whose solutions can be used to produce a solver for the whole system of equations that results from discretizing on the entire domain [21].

Fast forwarding to the 1960s, the first dynamic substructuring techniques were proposed by Gladwell. His methods are known by the name of 'Component-mode synthesis' [1]. A major step was taken by Crowley who looked into frequency based coupling techniques called SMURF. This method was later rewritten by Jetmundsen [5]. In 2008 De Klerk [8] provided an overview of historical methods and classified them in a general framework. His work provides the example on which the substructuring notation is based in this document.

DS can be performed in multiple domains including the physical, frequency and time domain which are related as in figure 2.5. In the physical domain, a system is represented by its mass, stiffness and damping distributions which are stored in its **M**, **K** and **C** matrices. If we consider a discrete dynamic system, one can write an equilibrium between the external forces and the internal forces by stating equation 2.5.

$$\mathbf{M}\ddot{\mathbf{u}}(t) + \mathbf{C}\dot{\mathbf{u}}(t) + \mathbf{K}\mathbf{u}(t) = \mathbf{f}(t) \tag{2.5}$$

In this equation **M**, **C** and **K** are mass, damping and stiffness matrices. **u** is the set of displacements for all the degrees of freedom of the system and **f** represents the external forces. The system matrices **M**, **C** and **K** are typically obtained by finite element modelling. From this physical domain it is possible to convert to other domains if they suite the application better. If one is interested in the response in the time domain, a time integration can be conducted to construct functions that display amplitude over time (for example the response of an impulse in time; an impulse response function (IRF)). However, in vibration analysis, one is interested in the structures response to a harmonic load. A more convenient domain to assess this behaviour is the frequency domain. By assuming a linear, time-invariant and steady state system, one can rewrite equation 2.5 in the frequency domain by using a Fourier transform:

$$\mathbf{M}\ddot{\mathbf{u}}(\omega) + \mathbf{C}\dot{\mathbf{u}}(\omega) + \mathbf{K}\mathbf{u}(\omega) = \mathbf{f}(\omega) \tag{2.6}$$

By knowing that $\dot{\mathbf{u}}(\omega) = j\omega\mathbf{u}(\omega)$ and $\ddot{\mathbf{u}}(\omega) = -\omega^2\mathbf{u}(\omega)$, one can rewrite this as:

$$\left[\omega^2\mathbf{M} + j\omega\mathbf{C} + \mathbf{K}\right]\mathbf{u}(\omega) = \mathbf{f}(\omega) \tag{2.7}$$

In which $\left[\omega^2\mathbf{M} + j\omega\mathbf{C} + \mathbf{K}\right]$ can be written in one matrix $\mathbf{Z}(\omega)$, the dynamic stiffness matrix. As explained in section 2.1.1 this is our desired property. The dynamic stiffness matrix is the inverse of the experimentally obtained frequency response function $\mathbf{Y}(\omega)$. For a detailed explanation on how this $\mathbf{Y}(\omega)$ (and by inversion: $\mathbf{Z}(\omega)$) is obtained, see section 2.2.

In theory, the same information is stored in the three domains, however sometimes one domain is more suited for the occasion than the others. Regardless of domain choice, two conditions must be satisfied at all times[8] regarding coupled systems:

1. Compatibility of the substructures' displacements at the interface.
2. Force equilibrium on the substructures' interface degrees of freedom.

These conditions form the basis of experimental dynamic substructuring, and by expressing these conditions mathematically in the domain of choice, one can analyse the dynamic behaviour of components and assemblies. In the scope of obtaining dynamic stiffness by experiment, the frequency is the domain of choice.

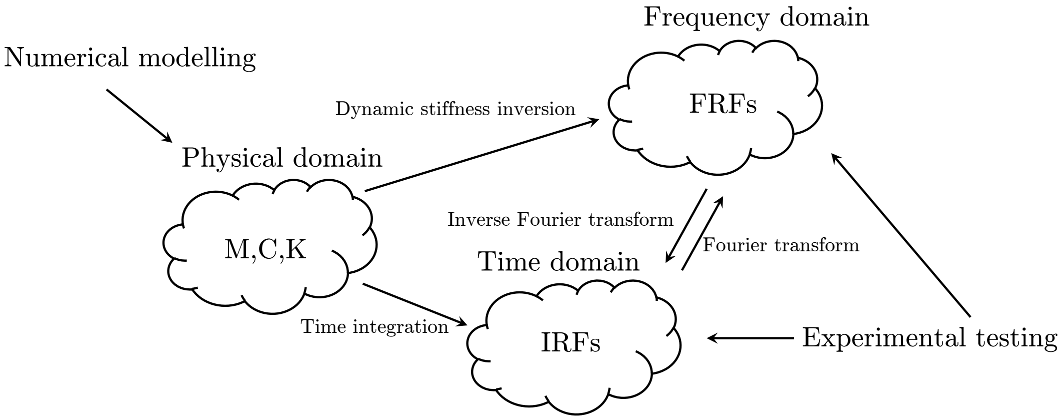

FIGURE 2.5: Relation between the physical, frequency and time domain in the context of dynamic substructuring.

### 2.3.1 Frequency based substructuring

There are multiple ways to Rome, and multiple methods to couple substructures in the frequency domain. Two methods are discussed in this subsection. The first method is the dual assembly which starts with the receptance matrices $\mathbf{Y}(\omega)$. From here on, a frequency dependency is not always explicitly expressed for better readability. This $\mathbf{Y}$ can be experimentally measured, so the dual assembly is applied when measured frequency response functions are available. The second method is the primal assembly in which the impedance matrices $\mathbf{Z}$ of the substructures are coupled. A $\mathbf{Z}$ matrix can be found from for example a finite element model. The relation between $\mathbf{Y}$ and $\mathbf{Z}$ is $\mathbf{Z} = \mathbf{Y}^{-1}$, so one can obtain the dynamic stiffness of a structure, simply by inverting the measured FRF matrix. It should be mentioned that a matrix is not always invertible so particular techniques are more suitable for solving certain problems [16].

#### Primal assembly

When one has access to the impedance (or dynamic stiffness) matrices $\mathbf{Z}$, the primal assembly is the way to go. A practical use case can be models created by Finite Element Method in CAD software from which the **Z** matrices can be extracted. The procedure to couple subsystems in the primal assembly is explained hereafter.

Firstly, one defines the system of equations to be:

$$\mathbf{ZLq} = \mathbf{f} + \mathbf{g} \tag{2.8}$$

$$\mathbf{L}^T\mathbf{g} = \mathbf{0} \tag{2.9}$$

In equation 2.8 and 2.9 **f** resembles the external forces and **g** the interface forces between the substructures. **L** is a localisation matrix mapping the physical DoFs of the system on a set of generalized DoF **q** as follows:

$$\mathbf{u} = \mathbf{Lq} \Rightarrow \begin{cases} u_1^A & = & q_1 \\ u_2^A & = & q_2 \\ u_3^A & = & q_3 \\ u_4^A & = & q_4 \end{cases} \quad \text{with} \quad \mathbf{L} \triangleq \begin{bmatrix} I & 0 & 0 \\ 0 & I & 0 \\ 0 & I & 0 \\ 0 & 0 & I \end{bmatrix} \tag{2.10}$$

If equation 2.8 is multiplied by $\mathbf{L}^T$, one sees:

$$\mathbf{L}^T\mathbf{ZLq} = \mathbf{L}^T\mathbf{f} \tag{2.11}$$

of which $\mathbf{L}^T\mathbf{ZL} = \hat{\mathbf{Z}}$ is the assembled impedance matrix for the generalised coordinates. Simply said, the primal coupling method comes down to adding overlapping dynamic stiffness matrix parts.

### Dual assembly

Experimental Frequency based substructuring (FBS) is a method of DS which derives the admittance of an assembled system $\mathbf{Y}^{AB}$ from the separate admittances of two subsystems $\mathbf{Y}^A$ and $\mathbf{Y}^B$. In the dual assembly method, one starts with the receptance matrix **Y**.

$$\mathbf{Y}(\omega) = \frac{\mathbf{u}(\omega)}{\mathbf{f}(\omega)} \tag{2.12}$$

In this section a brief example of frequency based substructuring is described. If one has two substructures $A$ and $B$ of which the FRF-matrix can be measured, the FRF of the assembly $AB$ can be calculated as shown in figure 2.6. However, it is also possible to measure the FRF of the assembly $AB$ and subtract the FRF of a substructure, for example $A$. This leaves the FRF of substructure $B$. This decoupling will prove to be very useful in the scope of measuring dynamic properties on resilient elements.

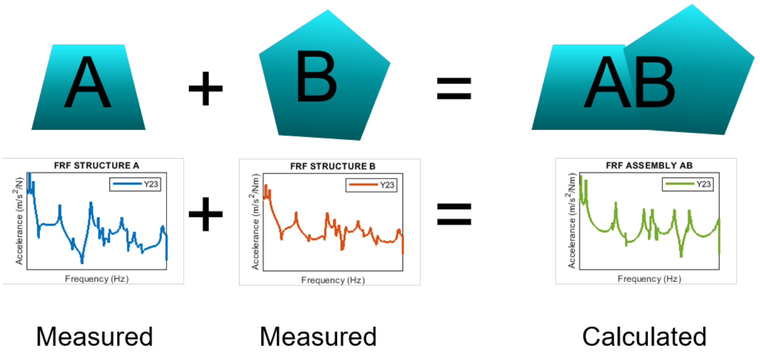

FIGURE 2.6: The FRF of the assemby can be mathematically calculated without ever physically couple the two substructures.

The equation to couple the FRFs of structure $A$ $\mathbf{Y}^A$ and structure $B$ $\mathbf{Y}^B$ is:

$$\left(\mathbf{Y}^{A|B}-\mathbf{Y}^{A|B}\mathbf{B}^T\left(\mathbf{B}\mathbf{Y}^{A|B}\mathbf{B}^T\right)^{-1}\mathbf{B}\mathbf{Y}^{A|B}\right)\mathbf{f}=\mathbf{u} \tag{2.13}$$

In this equation $\mathbf{Y}^{A|B}$ a matrix containing the uncoupled FRFs, $\mathbf{B}$ is a bookkeeping matrix which is explained below. The coupled FRF matrix is found to be:

$$\mathbf{Y}^{AB}=\left(\mathbf{Y}^{A|B}-\mathbf{Y}^{A|B}\mathbf{B}^T\left(\mathbf{B}\mathbf{Y}^{A|B}\mathbf{B}^T\right)^{-1}\mathbf{B}\mathbf{Y}^{A|B}\right) \tag{2.14}$$

The procedure is as follows. The first step is to measure the FRF-matrices of $A$ and $B$ from figure 2.7.

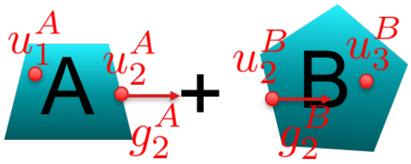

FIGURE 2.7: Substructure $A$ and $B$, with four degrees of freedom. $U_2^A$ and $U_2^B$ are DoFs on the interface, $g_2^A$ and $g_2^B$ are forces on the interface.

$$\mathbf{Y}^A=\begin{bmatrix}Y_{11}^A & Y_{12}^A\\ Y_{21}^A & Y_{22}^A\end{bmatrix}\quad\text{and}\quad\mathbf{Y}^B=\begin{bmatrix}Y_{22}^B & Y_{23}^A\\ Y_{23}^A & Y_{33}^A\end{bmatrix} \tag{2.15}$$

The next step is to relate these FRFs to the assembly forces and displacements.

$$\begin{bmatrix}Y_{11}^A & Y_{12}^A & 0 & 0\\ Y_{21}^A & Y_{22}^A & 0 & 0\\ 0 & 0 & Y_{22}^B & Y_{23}^A\\ 0 & 0 & Y_{32}^B & Y_{33}^A\end{bmatrix}\left(\begin{bmatrix}\mathbf{f}_1^A\\ \mathbf{f}_2^A\\ \mathbf{f}_2^B\\ \mathbf{f}_3^B\end{bmatrix}+\begin{bmatrix}0\\ \mathbf{g}_2^A\\ \mathbf{g}_2^B\\ 0\end{bmatrix}\right)=\begin{bmatrix}\mathbf{u}_1^A\\ \mathbf{u}_2^A\\ \mathbf{u}_2^B\\ \mathbf{u}_3^B\end{bmatrix}=\mathbf{u} \tag{2.16}$$

With $\mathbf{f}^{(s)}$ as the external force vector and $\mathbf{g}^{(s)}$ is the vector of connecting forces with other substructures. In this equation 2.16 it is assumed that the sensors on either side of the interface are in the same geometric position and that the impact forces are also on the same position and in the same direction. In finite element modelling this can be a fair assumption, however in experimental modelling this cannot be guaranteed. To overcome this practical problem, some solutions are proposed in section 2.3.2.

The next step is to formulate two conditions that an assembled system must comply to:

1. There must be continuity on the interface. So displacements of DoFs on the interface on $A$ must also be on the connecting interface on $B$. In this example this translates to $U_2^A=U_2^B$.
2. There must be force equilibrium on the DoFs on the interface. In our example this translates to $g_2^A=-g_2^B$.

With these conditions in mind, it is helpful to introduce a 'bookkeeping' matrix $\mathbf{B}$ which keeps track of what degrees of freedom are on the interface and impose the conditions on the system. For this example the $\mathbf{B}$ matrix is:

$$\mathbf{B}=\begin{bmatrix}0 & \mathbf{I} & -\mathbf{I} & 0\end{bmatrix} \tag{2.17}$$

So it is possible to write a system of equations:

$$\mathbf{u}_2^A - \mathbf{u}_2^B = 0 \tag{2.18}$$

$$\mathbf{B}\mathbf{u} = 0 \tag{2.19}$$

$$\mathbf{B} = \begin{bmatrix} 0 & \mathbf{I} & -\mathbf{I} & 0 \end{bmatrix} \tag{2.20}$$

If equation 2.18 is substituted in equation 2.19 and solve for $\lambda$ one obtains equation 2.21.

$$\lambda = -\left(\mathbf{B}\mathbf{Y}^{A|B}\mathbf{B}^T\right)^{-1}\mathbf{B}\mathbf{Y}^{A|B}\mathbf{f} \tag{2.21}$$

And if this is substituted back in equation 2.18, one can find equation 2.22.

$$\left(\mathbf{Y}^{A|B} - \mathbf{Y}^{A|B}\mathbf{B}^T\left(\mathbf{B}\mathbf{Y}^{A|B}\mathbf{B}^T\right)^{-1}\mathbf{B}\mathbf{Y}^{A|B}\right)\mathbf{f} = \mathbf{u} \tag{2.22}$$

Of which the left expression between the brackets is the coupled FRF of the assemby $AB$.

$$\mathbf{Y}^{AB} = \left(\mathbf{Y}^{A|B} - \mathbf{Y}^{A|B}\mathbf{B}^T\left(\mathbf{B}\mathbf{Y}^{A|B}\mathbf{B}^T\right)^{-1}\mathbf{B}\mathbf{Y}^{A|B}\right) \tag{2.23}$$

**The use of EDS/FBS on resilient elements**

One can asks themselves, why bother with EDS and FBS for measuring dynamic properties on resilient elements in the first place? Why not place accelerometers on the resilient element, excite the structure by impact and measure the response? Multiple reasons prevent from this to be feasible. The reason lies in the nature of an impact on a soft object. One can imagine that hitting a soft object with a hammer will result in a longer contact time than hitting a hard material. The duration of the impact will be longer. This lesser perfect impact will excite the test structure up till lower frequencies. A visual example is shown in figure 2.8.

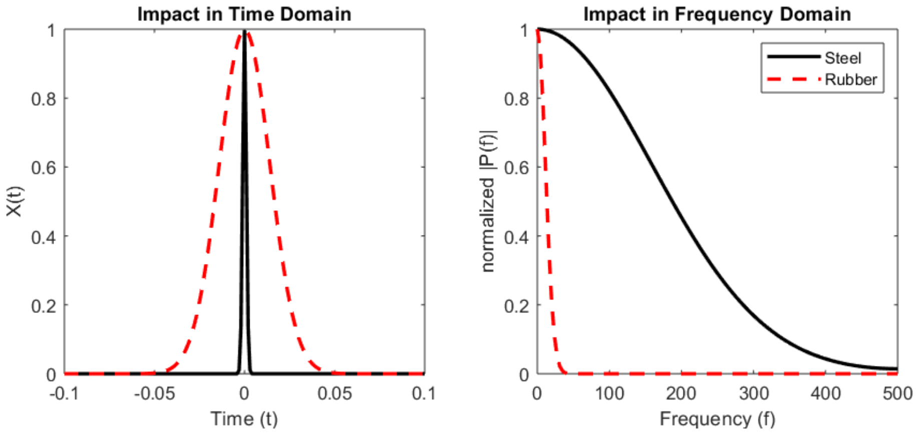

FIGURE 2.8: An example of an impact on steel and rubber in the time and frequency domain.

This can be understood mathematically by examining how the time signal is converted to the frequency domain by the Fourier transform. Secondly, it is often not possible to excite and measure a vibration isolator in all necessary direction because of its geometrical shape.

## 2.3.2 Interface modelling

DS is a wonderful engineering tool of which the techniques are formulated in a straightforward way. The biggest challenge in DS lies in the determining of the dynamics at the interface between the substructures [19]. To couple substructures properly, a complete and accurate model of the dynamics at the interface is required. From section 2.3 one learns that DS requires two conditions to be satisfied, namely:

- There must be continuity on the interface.
- There must be force equilibrium on the interface.

Which are mathematically described in equation 2.18 and 2.19. These conditions are imposable on point connections but unfortunately in the real world, joints are usually welded or bolted which are better represented by a line or surface connection. Modelling continuous connections is not feasible since one needs (in theory) an infinite amount of DoFs so usually a surface or line connection is represented by a set of discretized nodes, thus losing information on for example the rotation on the interface.

In a finite element analysis, one can impose a sufficient number of nodes over a large area so that any rotational coupling is implicitly accounted for. In experimental analysis it is harder to produce a method that will account for the desired six DoF measurement (three translational and three rotational). Translational accelerometers are readily available, but rotational sensors are still exotic [4]. Also, it is often not possible to place sensors directly on the interface between substructures. To overcome these obstacles, multiple methods are presented in section 2.3.2. In section 2.3.2 a more elaborate explanation is written on the state of the art method of introducing a Virtual Point (VP) on the interface of which the dynamics are calculated using multiple translational accelerometers placed nearby.

### Brief history

An alternative to using rotational sensors is calculating rotational DoFs by mathematics, which can be separated in two branches.

The first branch is based on global vibration modes of a system and are closely related to component mode synthesis techniques known from numerical modelling. In this branch one finds the *system equivalent reduction and expansion* or SEREP procedure [13] in which the translational motion of tri-axial sensors is combined to calculate rotational data. The advantage of this method is that the mode identification has a smoothing effect on the FRFs and thereby avoiding numerical instabilities. A disadvantage is that the global modes have to calculated by building a finite element model or perform modal analysis. The second branch is not based on global vibration modes but is a frequency based approach. An advantage of using FRFs directly is that the measurement data contains the residual terms from higher order modes. To include the rotational DoF data implicitly, multiple connection points on the interface are coupled which got the name *equivalent multiple point connection* or EMPC. A disadvantage is that overdetermination of the problem can lead to numerical instabilities. Recently a combination of CMS and EMPC is proposed including the concept of interface displacement modes [4].

### State of the art: Virtual Point transformation

In section 2.3.1 it is implicitly assumed that the sensors on either side of the interface are in exactly the same geometric position and directions when the substructures are coupled. It is also assumed that the forces on the interface are in the same spot and direction. These assumptions are required for FBS. Often it is not possible to measure directly on the interface between the substructures due to space restrictions. However, it is possible to project the measurements and impacts on a set of generalized displacements $\mathbf{q}$ and forces $\mathbf{m}$ to create collocated DoFs on the interface between the substructures using a Virtual Point (VP) transformation.

With the VP transformation, a virtual point is created using a set of measured DoF nearby that defines the 6 DoF ($x, y, z, \theta_x, \theta_y$ and $\theta_z$) of this virtual point. The first step is to project measured displacements $\mathbf{u}$ and forces $\mathbf{f}$ on a set of generalised displacements $\mathbf{q}$ and forces $\mathbf{m}$ by using interface deformation mode (IDM) matrices $\mathbf{R}_u$ and $\mathbf{R}_f$.

$$\mathbf{u} = \mathbf{R}_u\mathbf{q} \quad \text{and} \quad \mathbf{m} = \mathbf{R}_u^T\mathbf{f} \tag{2.24}$$

These IDMs contain geometric properties relating the position of the physical sensors to the virtual point. A row in a $\mathbf{R}$ matrix is constructed as:

$$\mathbf{R}^i = \left[\mathbf{e}^T | (\mathbf{r}^i \times \mathbf{e})^T\right] \tag{2.25}$$

In which $\mathbf{e}$ resembles the direction of a displacement DoF $\mathbf{u}^i$ and $\mathbf{r}^i$ is the distance from the physical sensor and the virtual point calculated as $\mathbf{r}^i = \mathbf{p}^i - \mathbf{p}_{vp}$ with $\mathbf{p}^i$ the location of the physical sensor and $\mathbf{p}_v p$ the location of the virtual point. To relate the measured FRF $\mathbf{Y}_{uf}$ to the calculated FRF in the virtual point $\mathbf{Y}_{qm}$, transformation matrices are constructed from the IDMs as seen in equation 2.26. These $\mathbf{T}$ matrices transform the measured FRFs to the virtual FRFs as seen in equation 2.27.

$$\mathbf{T}_u = \left(\mathbf{R}_u^T\mathbf{R}_u\right)^{-1}\mathbf{R}_u^T \quad \text{and} \quad \mathbf{T}_f^T = \mathbf{R}_f\left(\mathbf{R}_f^T\mathbf{R}_f\right)^{-1} \tag{2.26}$$

$$\mathbf{Y}_{qm} = \mathbf{T}_u\mathbf{Y}_{uf}\mathbf{T}_f^T \tag{2.27}$$

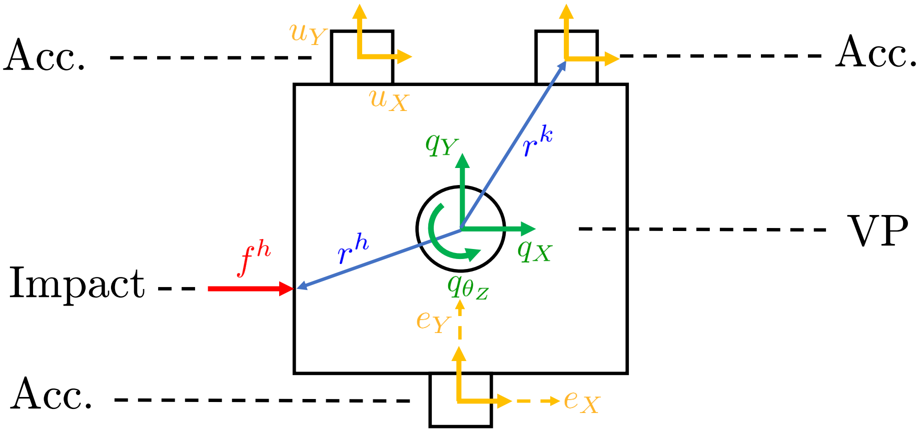

FIGURE 2.9: Visual representation of entities required to construct the virtual point transformation

In figure 2.9 accelerometers are placed on a structure with a hole in the middle. The structure will be coupled by a bolt through this hole so a description of the dynamics at this hole is required, but placing a sensor here is not possible. By using the entities depicted in the figure, it is possible to project the dynamics in the accelerometers surrounding the interface, on the interface creating a Virtual Point. By constructing VPs on the interface between substructures, one is able to couple them using FBS.

## 2.4 State of the art methods in EDS

Two dominant methods for determining the dynamic properties of resilient elements using FBS, impact testing and VP transformation exist today: full decoupling and inverse substructuring. Full decoupling exploits knowledge on the dynamic stiffness on structures surrounding the resilient element, while inverse substructuring is based on two assumptions that enables the use of a mathematical trick to determine the full dynamic stiffness matrix. Both methods are described hereafter.

### 2.4.1 Full decoupling

For the full decoupling method, one has a measurement setup as depicted in 2.10. This setup consists of three main components: $A$, $I$ and $B$. $A$ and $B$ are steel (or another stiff material) crosses glued to the test object (resilient element) $I$. The red arrows in figure 2.10 resemble impacts, the cubes are accelerometers. Ideally, the assembly would be floating in space, with no connections to other structures that could influence the measurement. Since this is not possible, the structure is suspended in low stiffness springs. If the eigenfrequency of the is lower than the first eigenfrequency of the structure itself, the influence of the connection can be neglected [11].

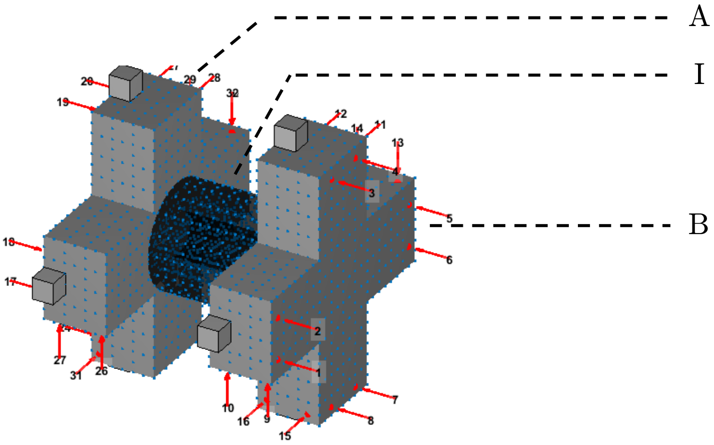

Figure 2.10: Measurement setup for the full decoupling method.

By exciting and measuring this assembly consisting of $A$, $I$ and $B$, the receptance matrix $\mathbf{Y}^{AIB}$ is obtained of which $\mathbf{Z}^{AIB}$ is calculated by inverting the receptance as shown in section 2.1.1. This matrix will be composed as follows:

$$\mathbf{Z}^{AIB} = \begin{bmatrix} \mathbf{Z}^{I}_{11} + \mathbf{Z}^{A}_{11} & \mathbf{Z}^{I}_{12} \\ \mathbf{Z}^{I}_{21} & \mathbf{Z}^{I}_{22} + \mathbf{Z}^{B}_{22} \end{bmatrix} \tag{2.28}$$

This $Z^{AIB}$ from equation 2.28 can be derived by following the primal assembly procedure described in section 2.3.1. A short recap example for this structure is shown hereafter. If one assumes cross $A$ and the resilient element $I$ coupled using a virtual point transformation with generalized displacements $\mathbf{q}$ and forces $\mathbf{m}$, one can write:

$$\begin{bmatrix} \mathbf{Z}^{A}_{11} & 0 & 0 \\ 0 & \mathbf{Z}^{I}_{11} & \mathbf{Z}^{I}_{12} \\ 0 & \mathbf{Z}^{I}_{21} & \mathbf{Z}^{I}_{22} \end{bmatrix} \begin{bmatrix} \mathbf{q}^{A}_{1} \\ \mathbf{q}^{I}_{1} \\ \mathbf{q}^{I}_{2} \end{bmatrix} = \begin{bmatrix} \mathbf{m}^{A}_{1} + \mathbf{g}^{A}_{1} \\ \mathbf{m}^{I}_{1} + \mathbf{g}^{I}_{1} \\ \mathbf{m}^{I}_{2} \end{bmatrix} \tag{2.29}$$

in which $\mathbf{g}$ resemble the interface forces and the subscripts$_1$ and $_2$ declare on which side of the isolator the property in question is located. The properties are sketched in figure 2.11.

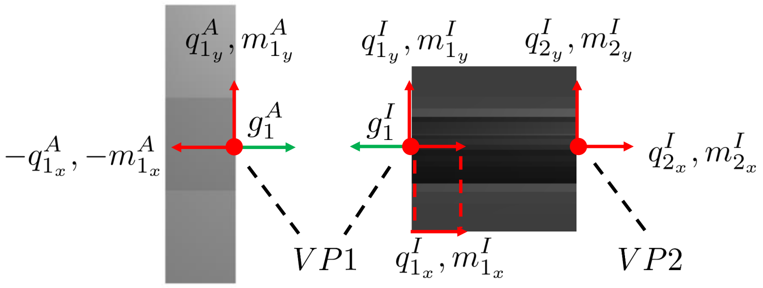

FIGURE 2.11: Sideview of the uncoupled structures $A$ (left) and $I$ (right). Two virtual points, $VP1$ and $VP2$ are defined on the interfaces between the substructures.

By imposing the the requirement of compatibility of displacements, one can state $\mathbf{q}_1^A = \mathbf{q}_1^I$. Define $\mathbf{q}_1^{AI} \triangleq \mathbf{q}_1^A = \mathbf{q}_1^I$ to write:

$$\begin{bmatrix} \mathbf{Z}_{11}^A & 0 \\ \mathbf{Z}_{11}^I & \mathbf{Z}_{12}^I \\ \mathbf{Z}_{21}^I & \mathbf{Z}_{22}^I \end{bmatrix} \begin{bmatrix} \mathbf{q}_1^{AI} \\ \mathbf{q}_2^I \end{bmatrix} = \begin{bmatrix} \mathbf{m}_1^A + \mathbf{g}_1^A \\ \mathbf{m}_1^I + \mathbf{g}_1^I \\ \mathbf{m}_2^I \end{bmatrix} \tag{2.30}$$

And by also imposing the second condition, the condition of equilibrium of forces on the interface $\mathbf{g}_1^A = -\mathbf{g}_1^I$, one can simplify:

$$\begin{bmatrix} \mathbf{Z}_{11}^A + \mathbf{Z}_{11}^I & \mathbf{Z}_{12}^I \\ \mathbf{Z}_{21}^I & \mathbf{Z}_{22}^I \end{bmatrix} \begin{bmatrix} \mathbf{q}_1^{AI} \\ \mathbf{q}_2^I \end{bmatrix} = \begin{bmatrix} \mathbf{m}_1^I + \mathbf{m}_1^A \\ \mathbf{m}_2^I \end{bmatrix} \tag{2.31}$$

In which:

$$\begin{bmatrix} \mathbf{Z}_{11}^A + \mathbf{Z}_{11}^I & \mathbf{Z}_{12}^I \\ \mathbf{Z}_{21}^I & \mathbf{Z}_{22}^I \end{bmatrix} = \mathbf{Z}^{AI} \tag{2.32}$$

With $\mathbf{Z}^{AI}$ being the coupled dynamic stiffness matrix of the two components $A$ and $I$. By following the same procedure to couple component $B$, one obtains equation 2.28. In this matrix $\mathbf{Z}^{AIB}$ the off-diagonal terms represent the dynamic transfer stiffness while the diagonal terms are the dynamic driving point stiffness. It is clear that the off-diagonal terms are solely a property of the isolator, but the diagonal terms also have a term containing the stiffness of the surrounding structures $A$ and $B$. In figure 2.6 it is shown that by obtaining FRFs of components, the FRF of the assembly can be calculated. The full decoupling exploits the fact that it is also possible to subtract the dynamics of a component from a measured structure, shown in figure 2.12.

Obviously, to execute this method one requires the dynamic stiffness matrices of the surrounding structures. This $\mathbf{Z}^A$ and $\mathbf{Z}^B$ can be obtained in two ways: numerically or experimentally.

Numerically, it is possible to obtain the dynamic stiffness by making use of the system matrices as shown in equation 2.7, if these are available. Another approach is to just use the weight and the rotational inertia from the structure, which are highly likely to be available from CAD software [4]. $\mathbf{Z}$ is obtained by equation 2.33.

$$\mathbf{Z} = -\omega^2 \mathbf{M} = \begin{bmatrix} m\mathbf{I} & -m \times \mathbf{r}_{V,G} \\ m \times \mathbf{r}_{V,G} & \Theta_V \end{bmatrix} \tag{2.33}$$

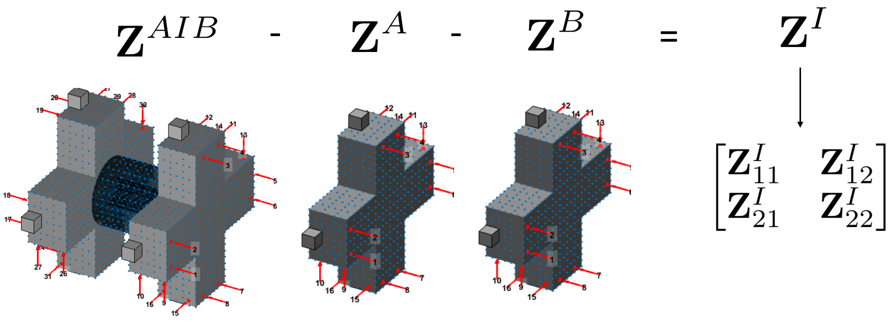
$\mathbf{Z}^{AIB}$ - $\mathbf{Z}^{A}$ - $\mathbf{Z}^{B}$ = $\mathbf{Z}^{I}$
$\begin{bmatrix} \mathbf{Z}^I_{11} & \mathbf{Z}^I_{12} \\ \mathbf{Z}^I_{21} & \mathbf{Z}^I_{22} \end{bmatrix}$

FIGURE 2.12: By subtracting the dynamic stiffness matrices of structure $A$ and $B$, only the properties of the isolator remain.

In which $m$ is the mass of the cross, $\mathbf{I}$ is an 3 by 3 identity matrix, $r_{V,G}$ a direction vector from the virtual point $V$ to the center of gravity $G$ and $\Theta_V$ the rotational inertia around the virtual point which is calculated by:

$$\Theta_V = \Theta_C + m(|\mathbf{r}_{V,G}|^2\mathbf{I} - \mathbf{r}_{V,G}\mathbf{r}^T_{V,G}) \tag{2.34}$$

in which $\Theta_C$ is the rotational inertia around the center of gravity which is commonly available from CAD software. The virtual point is located in the center on the interface where the crosses will be bonded with the resilient element.

The second way to obtain $\mathbf{Z}$ is by experiment. This is done by physically decoupling the crosses and follow the procedure described in 2.3.1. This method produces promising results [4] however the requirement to obtain the dynamic stiffness of the surrounding structures $A$ and $B$ can be experienced as a disadvantage to using this method. The next state of the art method, inverse substructuring, does not require knowledge of the dynamics of the surrounding components.

### 2.4.2 Inverse substructuring

Inverse substructuring is a method of determining the dynamic stiffness of a resilient element by making clever use of two assumptions. The first assumption is that the rubber isolator should have negligible mass. The second assumption states that the structure is coupled in a special topology in which a DoF on one side only has influence on the same DoF on the other side of the isolator. If these assumptions hold, the inverse substructuring states:

$$\mathbf{Z}^I_{11} = -\mathbf{Z}^I_{12} = -\mathbf{Z}^I_{21} = \mathbf{Z}^I_{22} \tag{2.35}$$

As seen in equation 2.28, the off diagonal terms $\mathbf{Z}^I_{12}$ and $\mathbf{Z}^I_{21}$ can be perfectly measured and using 2.35 the full dynamic stiffness matrix can be calculated. However, this assumes the two facts of negligible mass and the special topology, which are discussed hereafter.

#### Assumption 1: The isolator has negligible mass

This assumptions rises from the fact that by equating equation 2.35, the virtual point displacements on either side of the isolator are in phase so no internal resonances occur.

### Assumption 2: The structure is coupled in a special topology

The second assumption on inverse substructuring is that the resilient element connect the surrounding components $A$ and $B$ in a special topology. This special topology prescribes that a DoF on one side only influences the same DoF on the other side, as depicted in figure 2.13.

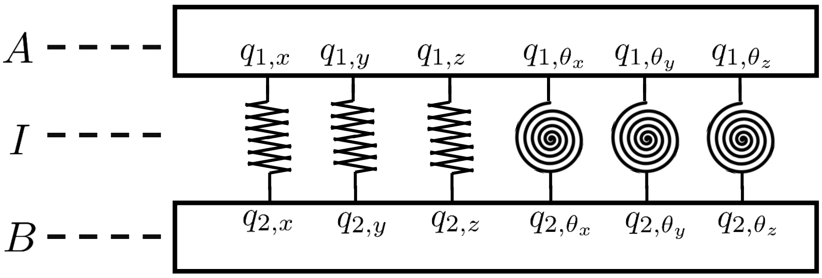

FIGURE 2.13: The special topology required for the assumption on inverse substructuring.

This assumption is in place to guarantee a matrix in which the four quadrants are block diagonal. To illustrate this phenomenon, a simple example involving two DoF on $A$ and two DoF on $B$ is closely examined, see figure 2.14.

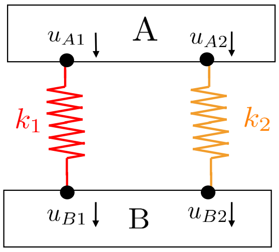

$$\begin{bmatrix} k_1 & 0 & -k_1 & 0 \\ 0 & k_2 & 0 & -k_2 \\ -k_1 & 0 & k_1 & 0 \\ 0 & -k_2 & 0 & k_2 \end{bmatrix} \begin{bmatrix} u_{A1} \\ u_{A2} \\ u_{B1} \\ u_{B2} \end{bmatrix} = \begin{bmatrix} F_{A1} \\ F_{A2} \\ F_{B1} \\ F_{B2} \end{bmatrix}$$

FIGURE 2.14: A simpler 4 DoF example on inverse substructuring. (left). The corresponding stiffness matrix of the system. (right)

If one splits the stiffness matrix of the simplified system in four quadrants, distinguishing the driving point stiffness and the dynamic transfer stiffness, on sees figure 2.15, assuming $k_1$ and $k_2$ to be dynamic stiffness.

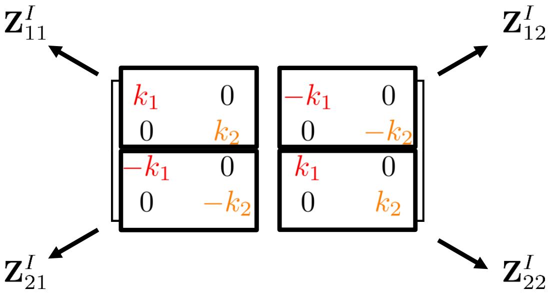

FIGURE 2.15: The stiffness matrix of a simplified system divided into four quadrants defining driving point- and transfer stiffness.

It is clear that the inverse substructuring equation 2.35 perfectly holds:

$$\begin{array}{ccccccc} \mathbf{Z}^I_{11} & = & -\mathbf{Z}^I_{12} & = & -\mathbf{Z}^I_{21} & = & \mathbf{Z}^I_{22} \\ \begin{bmatrix} k_1 & 0 \\ 0 & k_2 \end{bmatrix} & = & -\begin{bmatrix} -k_1 & 0 \\ 0 & -k_2 \end{bmatrix} & = & -\begin{bmatrix} -k_1 & 0 \\ 0 & -k_2 \end{bmatrix} & = & \begin{bmatrix} k_1 & 0 \\ 0 & k_2 \end{bmatrix} \end{array}$$

## 2.5 Proposition on improvement on inverse substructuring

It is a fact that the assumption on the special topology is invalid [2]. In [2] it is concluded, after validation with shaker tests, that cross couplings exists. Specifically named is the coupling between the radial directions and the rotation around the axis perpendicular to it. This phenomenon makes the equation 2.35 untrue. However, if one examines what occurs when cross couplings are present, it is possible to determine the driving point stiffness matrices from the unaffected transfer stiffness. If one takes the simplified example from section 2.4.2 and assume cross couplings, one sees figure 2.16.

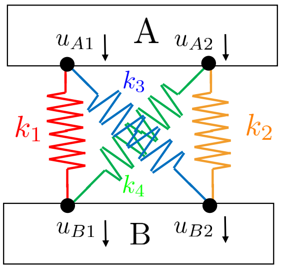

$$\begin{bmatrix} k_1+k_3 & 0 & -k_1 & -k_3 \\ 0 & k_2+k_4 & -k_4 & -k_2 \\ -k_1 & -k_4 & k_1+k_4 & 0 \\ -k_3 & -k_2 & 0 & k_2+k_3 \end{bmatrix} \begin{bmatrix} u_{A1} \\ u_{A2} \\ u_{B1} \\ u_{B2} \end{bmatrix} = \begin{bmatrix} F_{A1} \\ F_{A2} \\ F_{B1} \\ F_{B2} \end{bmatrix}$$

FIGURE 2.16: The simplified topology with cross couplings present. (left) The stiffness matrix of the system. (right)

If one again divide this stiffness matrix in quadrants, it shows:
This has the consequence that equation 2.35 does not hold:
This is just an arbitrary 4 DoF example. In section 2.5.1 a proposition is to determine the off diagonal values by making an educated guess using the geometry of the isolator.

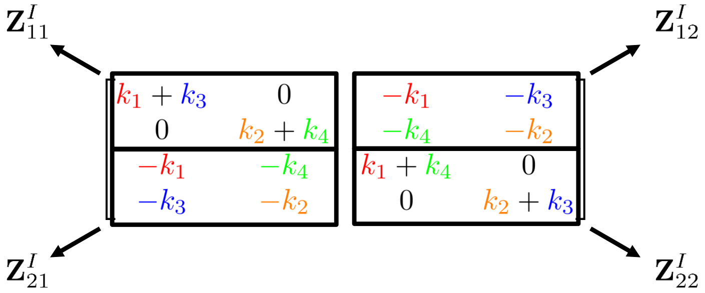
$\mathbf{Z}^I_{11}$
$\mathbf{Z}^I_{12}$
$\mathbf{Z}^I_{21}$
$\mathbf{Z}^I_{22}$
$k_1+k_3$ 0
0 $k_2+k_4$
$-k_1$ $-k_4$
$-k_3$ $-k_2$
$-k_1$ $-k_3$
$-k_4$ $-k_2$
$k_1+k_4$ 0
0 $k_2+k_3$

FIGURE 2.17: The simplified topology with cross couplings present. (left) The stiffness matrix of the system. (right)

$$\mathbf{Z}^I_{11} \neq -\mathbf{Z}^I_{12} \neq -\mathbf{Z}^I_{21} \neq \mathbf{Z}^I_{22}$$

$$\begin{bmatrix} k_1+k_3 & 0 \\ 0 & k_2+k_4 \end{bmatrix} \neq -\begin{bmatrix} -k_1 & -k_3 \\ -k_4 & -k_2 \end{bmatrix} \neq -\begin{bmatrix} -k_1 & -k_4 \\ -k_3 & -k_2 \end{bmatrix} \neq \begin{bmatrix} k_1+k_4 & 0 \\ 0 & k_2+k_3 \end{bmatrix}$$

### 2.5.1 Proposition for including crosscouplings

A solution to include crosscouplings in the description of the dynamic stiffness is to make an assumption of the shape of the isolator and make use of the known dynamics of this geometric shape. The shape of the isolator in this thesis resembles the most of a beam element. If one defines a beam with two nodes with six DoF each, as in figure 2.18, one can relate these DoF in multiple ways. Often used is the Euler Bernouilli beam theory for calculating loads and deflections for all degrees of freedom.

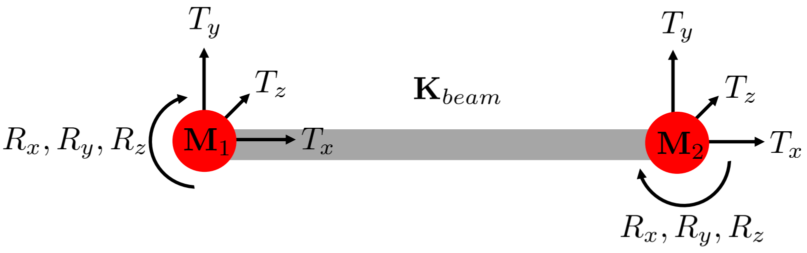
$T_y$
$T_z$
$\mathbf{K}_{beam}$
$T_y$
$T_z$
$R_x, R_y, R_z$
$\mathbf{M}_1$
$T_x$
$\mathbf{M}_2$
$T_x$
$R_x, R_y, R_z$

FIGURE 2.18: 2x6 DoF Euler Bernoulli beam

The stiffness matrix of a EB-beam element has the following sparsity pattern:

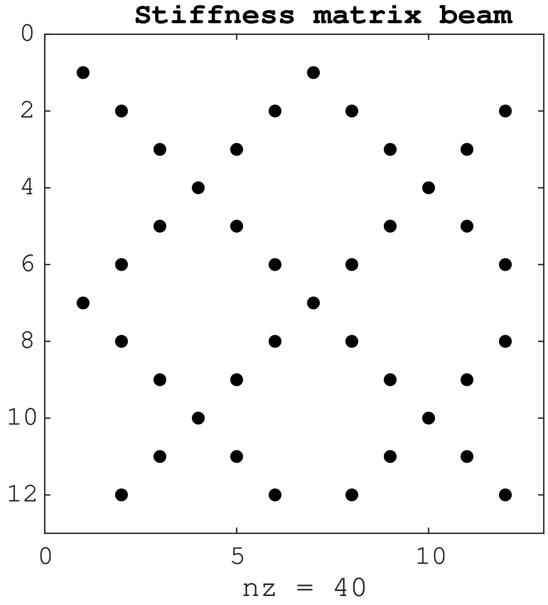

FIGURE 2.19: Sparsity pattern of a 2x6 DoF Euler Bernoulli beam

It is clear that in a EB-beam not only diagonal relations between DoF exist, but some DoF are coupled with other DoF. The $\mathbf{K}$ matrix is built from four quadrants $\mathbf{K}_{1,1}$, $\mathbf{K}_{1,2}$, $\mathbf{K}_{2,1}$ and $\mathbf{K}_{2,2}$ as follows:

$$\mathbf{K} = \frac{E}{L}\begin{bmatrix} \mathbf{K}_{1,1} & \mathbf{K}_{1,2} \\ \mathbf{K}_{2,1} & \mathbf{K}_{2,2} \end{bmatrix} \tag{2.36}$$

With:

$$\mathbf{K}_{1,1} = \begin{bmatrix} A & 0 & 0 & 0 & 0 & 0 \\ 0 & \frac{12I_z}{L^2} & 0 & 0 & 0 & \frac{6I_z}{L} \\ 0 & 0 & \frac{12I_y}{L^2} & 0 & \frac{-6I_y}{L} & 0 \\ 0 & 0 & 0 & GJ & 0 & 0 \\ 0 & 0 & \frac{-6I_y}{L} & 0 & 4I_y & 0 \\ 0 & \frac{6I_z}{L} & 0 & 0 & 0 & 4I_z \end{bmatrix} \tag{2.37}$$

$$\mathbf{K}_{1,2} = \begin{bmatrix} -A & 0 & 0 & 0 & 0 & 0 \\ 0 & \frac{-12I_z}{L^2} & 0 & 0 & 0 & \frac{6I_z}{L} \\ 0 & 0 & \frac{-12I_y}{L^2} & 0 & \frac{-6I_y}{L} & 0 \\ 0 & 0 & 0 & -GJ & 0 & 0 \\ 0 & 0 & \frac{6I_y}{L} & 0 & 2I_y & 0 \\ 0 & \frac{-6I_z}{L} & 0 & 0 & 0 & 2I_z \end{bmatrix} \tag{2.38}$$

$$\mathbf{K}_{2,1} = \begin{bmatrix} -A & 0 & 0 & 0 & 0 & 0 \\ 0 & \frac{-12I_z}{L^2} & 0 & 0 & 0 & \frac{-6I_z}{L} \\ 0 & 0 & \frac{-12I_y}{L^2} & 0 & \frac{6I_y}{L} & 0 \\ 0 & 0 & 0 & -GJ & 0 & 0 \\ 0 & 0 & \frac{-6I_y}{L} & 0 & 2I_y & 0 \\ 0 & \frac{6I_z}{L} & 0 & 0 & 0 & 2I_z \end{bmatrix} \tag{2.39}$$

$$\mathbf{K}_{2,2} = \begin{bmatrix} A & 0 & 0 & 0 & 0 & 0 \\ 0 & \frac{12I_z}{L^2} & 0 & 0 & 0 & \frac{-6I_z}{L} \\ 0 & 0 & \frac{12I_y}{L^2} & 0 & \frac{6I_y}{L} & 0 \\ 0 & 0 & 0 & GJ & 0 & 0 \\ 0 & 0 & \frac{6I_y}{L} & 0 & 4I_y & 0 \\ 0 & \frac{-6I_z}{L} & 0 & 0 & 0 & 4I_z \end{bmatrix} \tag{2.40}$$

With parameters $A$ = cross sectional area of the interface, $I_{xyz}$ = moment of inertia around $x, y, z$ axes, $L$ = length of the interface, $G$ = the shear modulus of elasticity, $J$ = the polar moment of inertia $E = E_c(1 + \eta j)$ = Young's Modulus of the material with $E_c$ is the Young's Modulus coefficient and $\eta$ the Loss Factor.

From the stiffness matrix for a beam, and the geometry of the rubber isolator, one can conclude that all cross couplings are equal and can be opposite, as presented in the full element stiffness matrices in 3.5. So one can account for cross couplings in the $\mathbf{Z}^I$ matrix by taking the transfer coupling stiffnessess (which are unaffected by the transmission simulators) and correct these values with the correct sign and add them to the $\mathbf{Z}^I$ matrix on the correct places following the bernouilli beam scheme. One can just use one value of the transfer crosscouplings for this procedure. For example:

$$\mathbf{Z}^I_{12}(5,1) \rightarrow \mathbf{Z}^I_{11}(5,1), \quad \mathbf{Z}^I_{11}(1,5), \quad \mathbf{Z}^I_{22}(4,2), \quad \mathbf{Z}^I_{22}(2,4) \tag{2.41}$$

And

$$-\mathbf{Z}^I_{12}(5,1) \rightarrow \mathbf{Z}^I_{11}(2,4), \quad \mathbf{Z}^I_{11}(4,2), \quad \mathbf{Z}^I_{22}(1,5), \quad \mathbf{Z}^I_{22}(5,1) \tag{2.42}$$

In which the arrow means 'substitute for'.

### 2.5.2 Proposition for including Isolator Mass

As suggested by [3], a way to incorperate the isolator mass in inverse substructuring is by addind a correction term to the dynamic stiffness matrix. Firstly, the weight of the isolator is simply weighed on a scale to obtain $\mathbf{M}_I$. To correct for the mass one applies the following correction to $\mathbf{Z}^I$ obtained by inverse substructuring:

$$\mathbf{Z}^I = \begin{bmatrix} -\text{diag}\left(\mathbf{Z}^{AIB}_{12}\right) & \text{diag}\left(\mathbf{Z}^{AIB}_{12}\right) \\ \text{diag}\left(\mathbf{Z}^{AIB}_{12}\right) & -\text{diag}\left(\mathbf{Z}^{AIB}_{12}\right) \end{bmatrix} - \omega^2 \begin{bmatrix} \mathbf{M}_r & 0 \\ 0 & \mathbf{M}_r \end{bmatrix} \tag{2.43}$$

However, research in [3] concluded that including the isolator mass does not yield significantly better results and is not included in this thesis.

# Chapter 3

# Example

In this chapter a simple system is constructed to do basic analysis. This exercise is vital to get an understanding on the dynamics in multi DoF systems. The influence of the system matrices on the frequency response is examined and the difference between Full Decoupling and Inverse Substructuring on a basic system is checked.

## 3.1 A simple system

To gain insight in the frequency response of complex systems, it is essential to have knowledge on the influence of different factors on these systems. A way to gain this knowledge is by creating a simple system and vary some parameters which are to be expected to be the most influential on the frequency response. This simple system consists of two masses $m1$ and $m2$ connected by an interface $I$. The model consists of 12 Degrees of Freedom; Per mass there are three translational degrees of freedom and three rotational degrees of freedom.

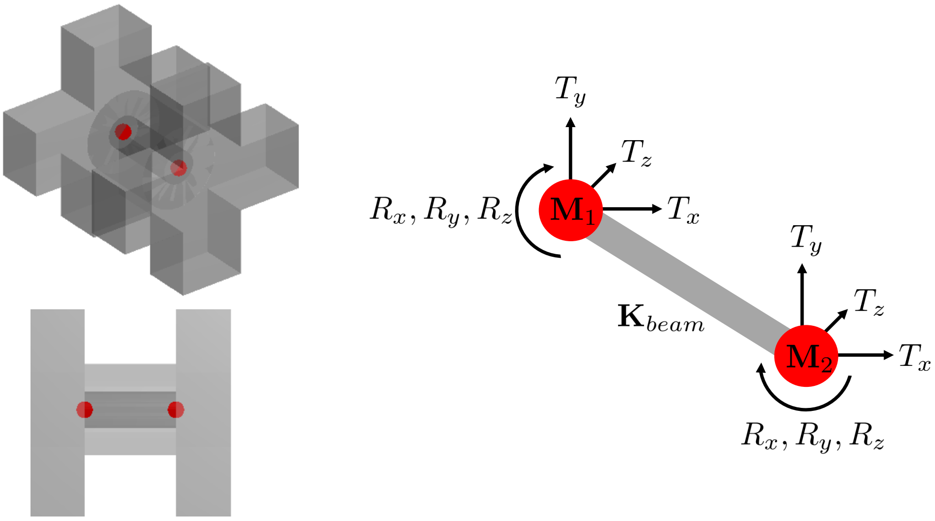

FIGURE 3.1: Simple model of the crosses and isolator system with two times 6 DoF connected by a beam element.

The interface is modelled as a massless beam element with six DoF on each end with a complex stiffness component (structural damping). The expression for dynamic stiffness is:

$$\mathbf{Z}(\omega) = -\omega^2\mathbf{M} + \mathbf{K} \tag{3.1}$$

With system matrices $\mathbf{M}$ and $\mathbf{K}$:

$$\mathbf{M} = \begin{bmatrix} \mathbf{M}_1 & \mathbf{0} \\ \mathbf{0} & \mathbf{M}_2 \end{bmatrix} \tag{3.2}$$

With:

$$\mathbf{M}_1 = \begin{bmatrix} m_1 & 0 & \cdots & \cdots & \cdots & 0 \\ & m_1 & \ddots & & & \vdots \\ & & m_1 & \ddots & & \vdots \\ & & & 0.4 m_1 r^2 & \ddots & \vdots \\ & \text{Sym.} & & & 0.4 m_1 r^2 & 0 \\ & & & & & 0.4 m_1 r^2 \end{bmatrix} \tag{3.3}$$

and $\mathbf{M}_2$ dito (replace $m_1$ for $m_2$). The stiffness matrix is:

$$\mathbf{K} = \frac{E}{L} \begin{bmatrix} \mathbf{K}_{1,1} & \mathbf{K}_{1,2} \\ \mathbf{K}_{2,1} & \mathbf{K}_{2,2} \end{bmatrix} \tag{3.4}$$

With:

$$\mathbf{K}_{1,1} = \begin{bmatrix} A & 0 & 0 & 0 & 0 & 0 \\ 0 & \frac{12 I_z}{L^2} & 0 & 0 & 0 & \frac{6 I_z}{L} \\ 0 & 0 & \frac{12 I_y}{L^2} & 0 & \frac{-6 I_y}{L} & 0 \\ 0 & 0 & 0 & GJ & 0 & 0 \\ 0 & 0 & \frac{-6 I_y}{L} & 0 & 4 I_y & 0 \\ 0 & \frac{6 I_z}{L} & 0 & 0 & 0 & 4 I_z \end{bmatrix} \tag{3.5}$$

$$\mathbf{K}_{1,2} = \begin{bmatrix} -A & 0 & 0 & 0 & 0 & 0 \\ 0 & \frac{-12 I_z}{L^2} & 0 & 0 & 0 & \frac{6 I_z}{L} \\ 0 & 0 & \frac{-12 I_y}{L^2} & 0 & \frac{-6 I_y}{L} & 0 \\ 0 & 0 & 0 & -GJ & 0 & 0 \\ 0 & 0 & \frac{6 I_y}{L} & 0 & 2 I_y & 0 \\ 0 & \frac{-6 I_z}{L} & 0 & 0 & 0 & 2 I_z \end{bmatrix} \tag{3.6}$$

$$\mathbf{K}_{2,1} = \begin{bmatrix} -A & 0 & 0 & 0 & 0 & 0 \\ 0 & \frac{-12 I_z}{L^2} & 0 & 0 & 0 & \frac{-6 I_z}{L} \\ 0 & 0 & \frac{-12 I_y}{L^2} & 0 & \frac{6 I_y}{L} & 0 \\ 0 & 0 & 0 & -GJ & 0 & 0 \\ 0 & 0 & \frac{-6 I_y}{L} & 0 & 2 I_y & 0 \\ 0 & \frac{6 I_z}{L} & 0 & 0 & 0 & 2 I_z \end{bmatrix} \tag{3.7}$$

$$\mathbf{K}_{2,2} = \begin{bmatrix} A & 0 & 0 & 0 & 0 & 0 \\ 0 & \frac{12 I_z}{L^2} & 0 & 0 & 0 & \frac{-6 I_z}{L} \\ 0 & 0 & \frac{12 I_y}{L^2} & 0 & \frac{6 I_y}{L} & 0 \\ 0 & 0 & 0 & GJ & 0 & 0 \\ 0 & 0 & \frac{6 I_y}{L} & 0 & 4 I_y & 0 \\ 0 & \frac{-6 I_z}{L} & 0 & 0 & 0 & 4 I_z \end{bmatrix} \tag{3.8}$$

With parameters $A$ = cross sectional area of the interface, $I_{xyz}$ = moment of inertia around $x, y, z$ axes, $L$ = length of the interface, $G$ = the shear modulus of elasticity, $J$ = the polar moment of inertia $E = E_c(1 + \eta j)$ = Young's Modulus of the material with $E_c$ is the Young's Modulus coefficient and $\eta$ the Loss Factor. For clarity, the visualized sparsity patterns of the system are seen in figure 3.2.

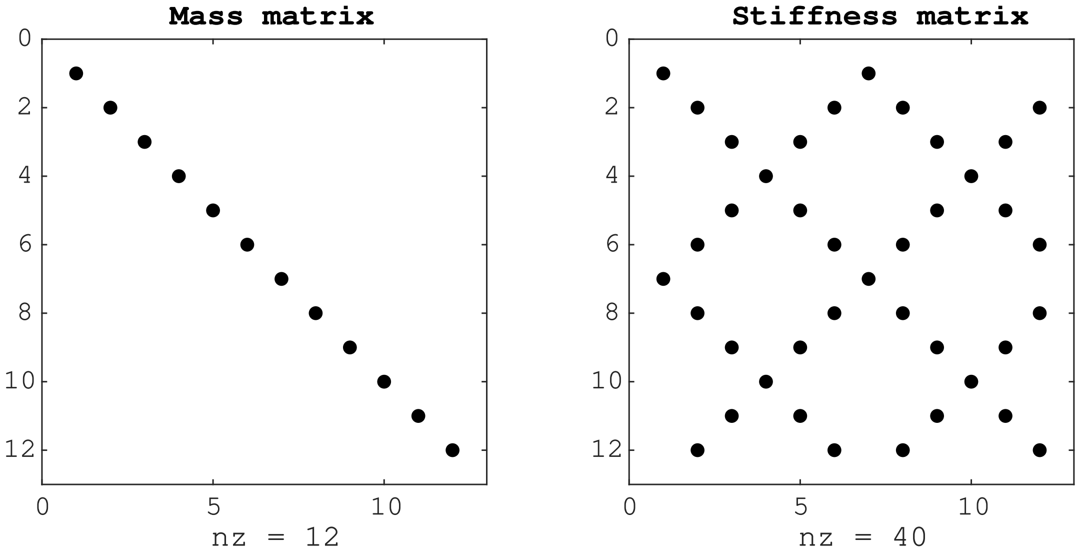

FIGURE 3.2: Sparsity pattern of the 12x12 Mass- and Stiffness matrix.

### 3.1.1 Varying Mass

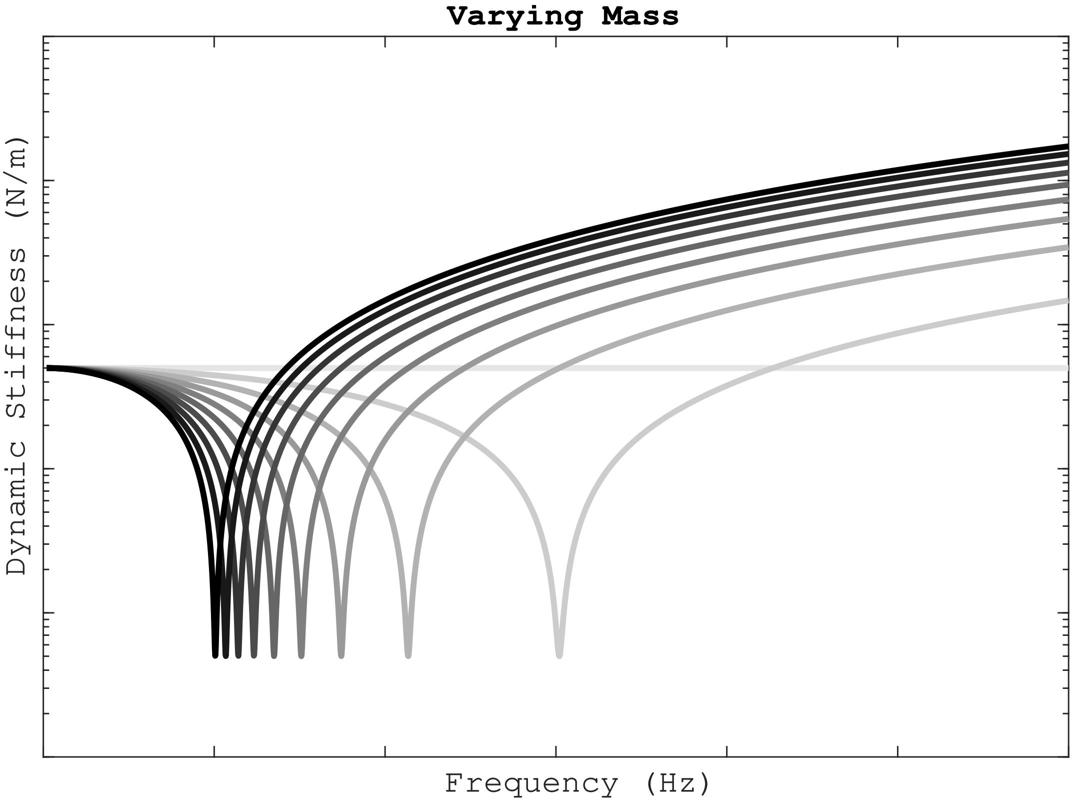

FIGURE 3.3: Dynamic stiffness response of varying mass

**Observation**

Static Dynamic stiffness, the stiffness at 0 Hz, does not change with changing mass. The resonance peak frequency does increase with decreasing mass. With $m_1 = 0$, the dynamic stiffness is a flat line. The dynamic stiffness for frequencies higher than resonance will never be the same for different mass. The dynamic stiffness will keep rising for higher frequencies regardless of mass.

### Explanation

When equation 3.1 is observed, most phenomena can be explained. Firstly, for the static stiffness $\omega = 0$, so $\mathbf{Z}(0) = \mathbf{K}$ is not dependent on mass. The increasing stiffness of the resonance peak is caused by the fact that a resonance occurs at $\omega_n = \sqrt{k/m_1}$, with $k$ and $m_1$ the stiffness in the DoF. With an decreasing mass, $\omega_n$ will rise. For $m_1 = 0$, 3.1 becomes $\mathbf{Z}(\omega) = \mathbf{K}$, so not dependent on frequency and will display a flat line in this spectrum with $\mathbf{K}$ as magnitude. At higher frequencies, the difference between dynamic stiffness for different mass will linearly scale with said mass. At frequencies hiogher than resonance, the dynamic stiffness will keep increasing. This is the typical mass line where the stiffness matrix $\mathbf{K}$ is relatively irrelevant and the $\mathbf{Z}$ is mostly determined by $-\omega^2\mathbf{M}$ because of high $\omega$.

## 3.1.2 Varying Stiffness

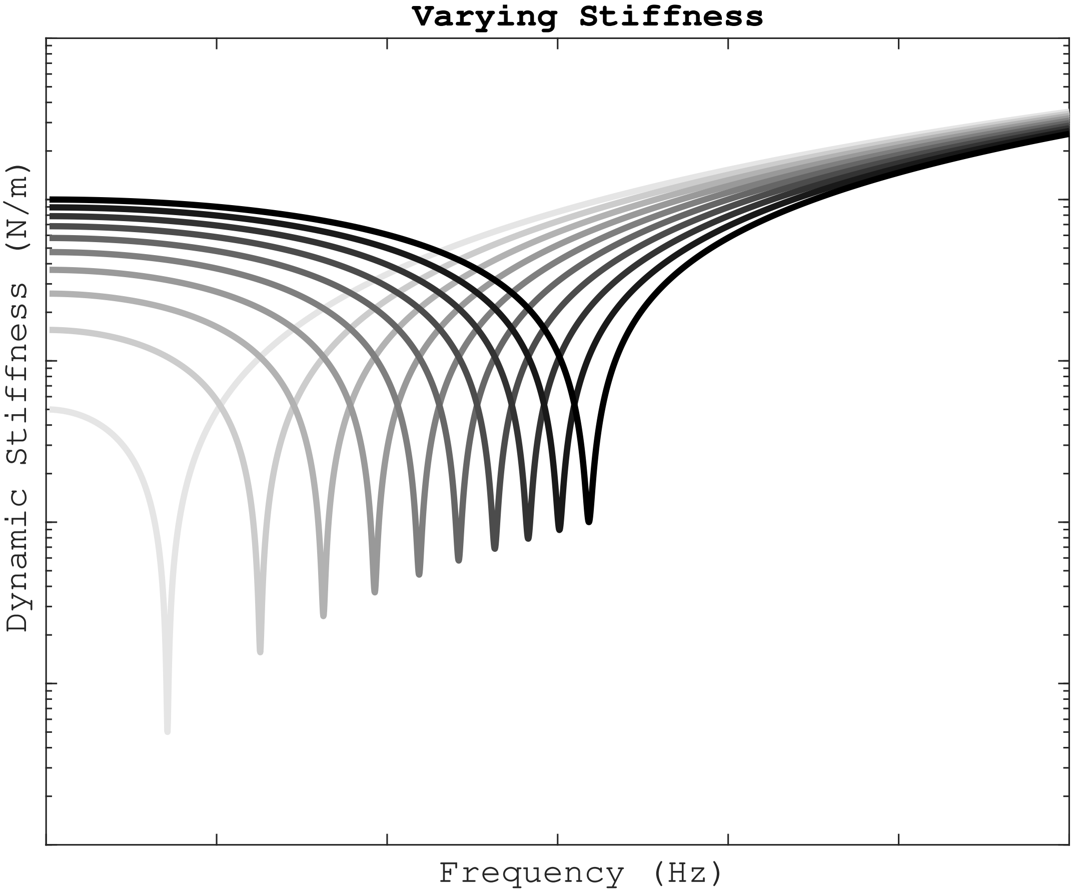

FIGURE 3.4: Dynamic stiffness response of varying stiffness

### Observation

The resonance frequency increases with an increase in stiffness. The resonance peak will bounce up at a higher dynamic stiffness for an increase in stiffness. Static stiffness will increase with increasing $\mathbf{K}$ matrix. At higher frequencies all frequency responses converge to the same value regardless of stiffness matrix.

**Explanation**

The resonance frequency increases with stiffness because of the resonance frequency is calculated by $\sqrt{k_1/m}$. The resonance peak is also at a higher frequency so if one examines equation 3.1, one can see that for an increasing **K**, the value of **Z** will also increase.

### 3.1.3 Varying Loss Factor

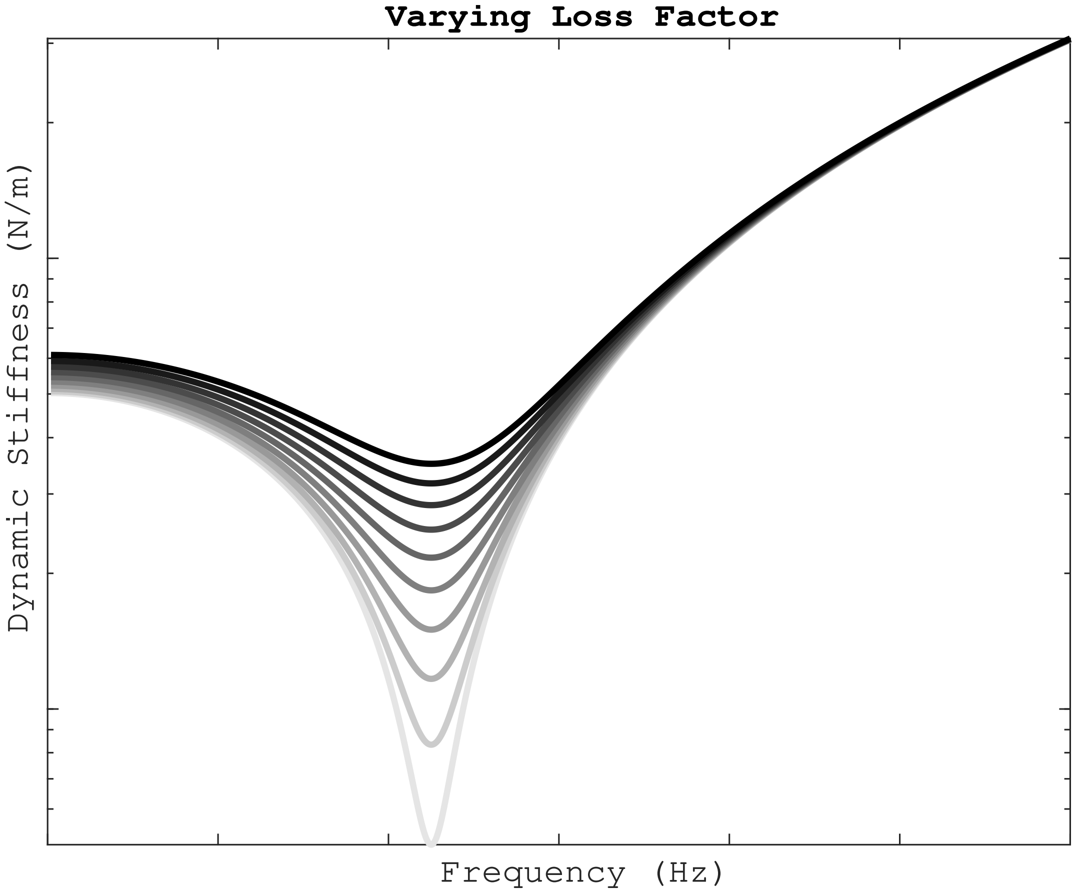

FIGURE 3.5: Dynamic stiffness response of varying mass

**Observation**

The static stiffness decreases with decreasing loss factor. The resonance frequency is not frequency dependent. The amplitude of the resonance is greatly reduced by an increase in loss factor. Also the sharpness of the peak is reduced. At higher frequencies, the dynamic stiffness is not influenced by a varying loss factor.

**Explanation**

The loss factor $\eta$ is introduced as a material property that influences the complex Young's modulus $E = E_{coff}(1 + \eta j)$ with $j = \sqrt{-1}$. This complex $E$ in turn creates a complex **K** matrix. For a more in depth discussion on this phenomenon and how it causes a damping effect, see [15]. It is important to note that absolute values are plotted in figure 3.5.

### 3.1.4 Summary

In this graph 3.6 four lines are plotted. In blue is a baseline, and the three remaining lines change one system matrix at a time. By glancing over this figure one can quickly figure out how the different building blocks of $\mathbf{Z}(\omega)$ influence a frequency response.

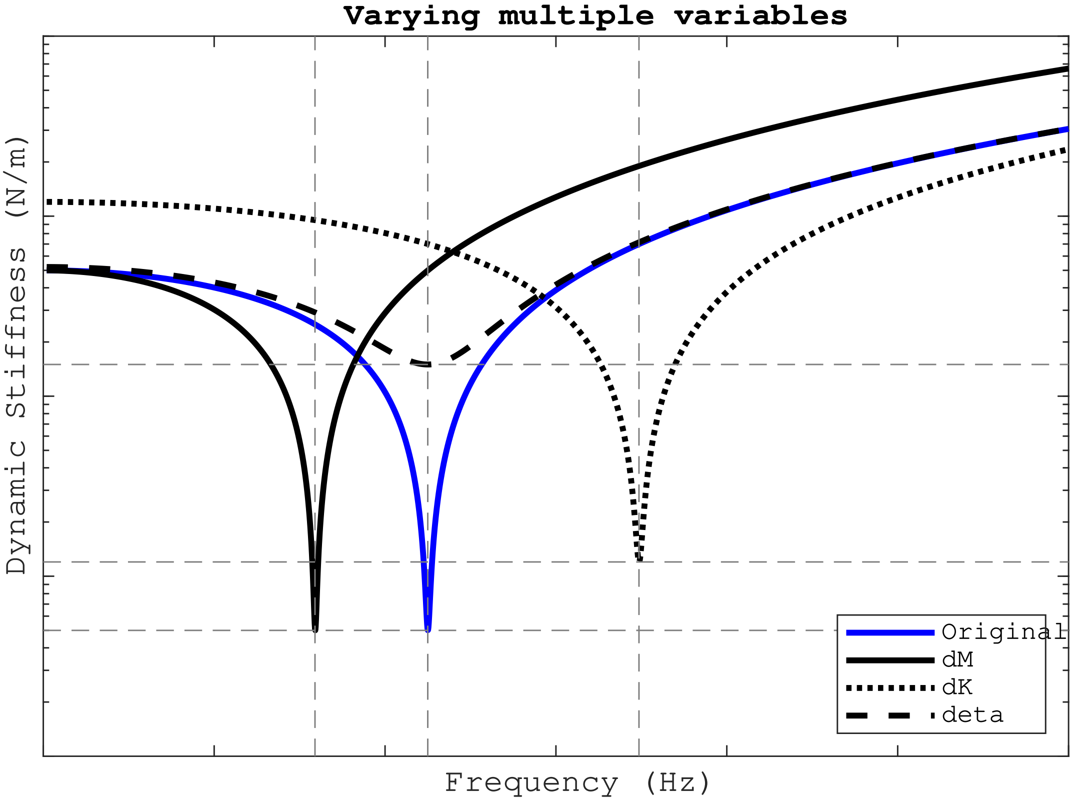

FIGURE 3.6: Dynamic stiffness response with multiple parameters varied.

## 3.2 Dynamic substructuring: Full Decoupling and Inverse Substructuring

Now there is knowledge on the simple system but how do the two substructuring techniques compare on this simple system. A quick recap for this simple system is now given and the the results are compared.

#### Full Decoupling

To perform full decoupling on the assembly, the dynamic stiffnessess of the three substructures $A$, $I$ and $B$ are required. For this simple system, these can be calculated by hand. For substructure A:

$$\mathbf{Z}^A = -\omega^2 \mathbf{M_1} + \mathbf{K}^A \tag{3.9}$$

Since it is assumed that the substructure behaves like a rigid body one can say $\mathbf{K}^A = 0$. For subsystem $B$, the same holds:

$$\mathbf{Z}^B = -\omega^2 \mathbf{M_2} \tag{3.10}$$

The full decoupling procedure takes place as follows:

$$\mathbf{Z}^{AIB} - \mathbf{Z}^{A} - \mathbf{Z}^{B} = \mathbf{Z}^{I}_{FD} \tag{3.11}$$

Or in more detail:

$$\begin{bmatrix} \mathbf{Z}^{A}_{11} + \mathbf{Z}^{I}_{11} & \mathbf{Z}^{I}_{12} \\ \mathbf{Z}^{I}_{21} & \mathbf{Z}^{B}_{22} + \mathbf{Z}^{I}_{22} \end{bmatrix} - \begin{bmatrix} \mathbf{Z}^{A}_{11} & 0 \\ 0 & \mathbf{Z}^{B}_{22} \end{bmatrix} = \begin{bmatrix} \mathbf{Z}^{I}_{11} & \mathbf{Z}^{I}_{12} \\ \mathbf{Z}^{I}_{21} & \mathbf{Z}^{I}_{22} \end{bmatrix} = \mathbf{Z}^{I}_{FD} \tag{3.12}$$

Where the subscript $_{FD}$ indicates the dynamic stiffness is obtained by full decoupling.

### Inverse substructuring

For inverse substructuring, one does not compute the dynamic stiffness of the substructures $A$ and $B$ but claim that the transfer stiffness $\mathbf{Z}^{I}_{12}$ and $\mathbf{Z}^{I}_{21}$ are not dependent on these substructures and when $A$ and $B$ are decoupled the driving point stiffness is equal but opposite. In equations:

$$\mathbf{Z}^{AIB}_{12} = \mathbf{Z}^{I}_{12} \quad \text{and} \quad \mathbf{Z}^{I}_{12} = -\mathbf{Z}^{I}_{11} \tag{3.13}$$

This way the full $\mathbf{Z}^{I}_{INV}$ matrix can be created without knowledge of dynamic properties of $A$ and $B$. In the next subsections the results of fully decoupling and inverse substructuring are compared for the simple model.

## 3.2.1 Axial stiffness

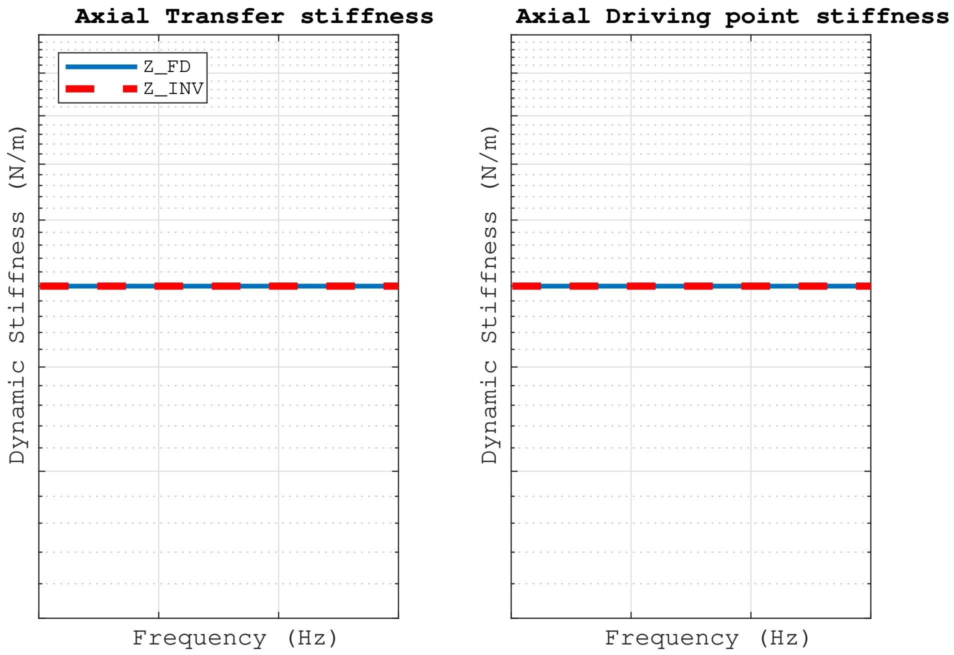

FIGURE 3.7: Dynamic stiffness response with multiple parameters varied.

### Observation

For axial transfer stiffness, the dynamic stiffness for the full decoupling method and the inverse substructuring method is a flat line in the frequency domain. The full decoupling stiffness and the inverse substructuring stiffness is equal. The same holds for the driving point stiffness.

**Explanation**

Firstly the driving point stiffness is examined. The dynamic stiffness is calculated by equation 2.2. If one fills this equation in for $\mathbf{Z}_{12}^{FD}$ with the system matrices 3.3 and 3.5 after the decoupling procedure described in 3.11, one finds for the axial direction:

$$\mathbf{Z}_{11}^{FD} = -\omega^2(\mathbf{M}_1 - m_1) + A = A \tag{3.14}$$

Which is obviously not frequency dependent and has a constant value of A. If one then examines the axial stiffness for the inverse substructuring method by using the same system matrices from section 3.1, one finds:

$$\mathbf{Z}_{11}^{INV} = -\mathbf{Z}_{12} = -(-\omega^2(0-0) - A) = A \tag{3.15}$$

Which is also not frequency dependent and has a constant value of A.

For the transfer stiffness, the system matrix from equations 3.6 and 3.3 are used to find that for the full decoupling:

$$\mathbf{Z}_{12}^{FD} = -\omega^2 0 + A) = A \tag{3.16}$$

and

$$\mathbf{Z}_{12}^{INV} = \mathbf{Z}_{12} = \mathbf{Z}_{12}^{FD} = -(-\omega^2(0-0) - A) = A \tag{3.17}$$

## 3.3 Adding mass to the isolator

To create a more complex model, mass is added to the isolator subsystem as shown in figure 3.8. This will convert the system from 12 DoF to 18 Dof with the following system matrices:

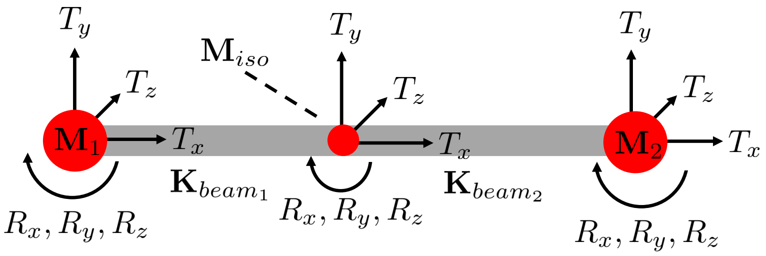

FIGURE 3.8: Simple model of the crosses and isolator system with three times 6 DoF connected by two beam elements.

$$\mathbf{M} = \begin{bmatrix} \mathbf{M}_1 & \mathbf{0} & \mathbf{0} \\ \mathbf{0} & \mathbf{M}_{iso} & \mathbf{0} \\ \mathbf{0} & \mathbf{0} & \mathbf{M}_2 \end{bmatrix} \tag{3.18}$$

With $\mathbf{M}_1$ is equal to equation 3.3 and $\mathbf{M}_2$ dito (replace $m_1$ for $m_2$). If one assumes a point mass in the centre of the isolator, $\mathbf{M}_{iso}$ is:

$$\mathbf{M}_{iso} = \begin{bmatrix} m_{iso} & 0 & \cdots & \cdots & \cdots & 0 \\ & m_{iso} & \ddots & & & \vdots \\ & & m_{iso} & \ddots & & \vdots \\ & & & m_{iso} & \ddots & \vdots \\ & \text{Sym.} & & & m_{iso} & 0 \\ & & & & & m_{iso} \end{bmatrix} \tag{3.19}$$

As can be seen in figure 3.8, the masses and isolator subsytem are connected by two beam elements. This 18 DoF $\mathbf{K}$ matrix will take the form of:

$$\mathbf{K} = \frac{E}{L} \begin{bmatrix} \mathbf{K}_{1,1}^{(1)} & \mathbf{K}_{1,2}^{(1)} & 0 \\ \mathbf{K}_{2,1}^{(1)} & \mathbf{K}_{2,2}^{(1)} + \mathbf{K}_{2,2}^{(2)} & \mathbf{K}_{2,3}^{(2)} \\ 0 & \mathbf{K}_{3,2}^{(2)} & \mathbf{K}_{3,3}^{(2)} \end{bmatrix} \tag{3.20}$$

Where the superscript $^{(1)}$ or $^{(2)}$ indicates if the partial stiffness matrix is part of $\mathbf{K}_{beam1}$ or $\mathbf{K}_{beam2}$. In equation 3.20 $\mathbf{K}_{1,1}^{(1)}$, $\mathbf{K}_{1,2}^{(1)}$, $\mathbf{K}_{2,1}^{(1)}$ and $\mathbf{K}_{2,2}^{(1)}$ are equal to equation 3.5 and 3.6 respectively, as well as $\mathbf{K}_{2,2}^{(2)}$, $\mathbf{K}_{2,3}^{(2)}$, $\mathbf{K}_{3,2}^{(2)}$ and $\mathbf{K}_{3,3}^{(2)}$.

It is interesting to examine what the influence of isolator mass is on the frequency response, and to inspect if it creates a difference in this frequency response for transfer and driving point stiffness when the two substructuring techniques are applied.

For research on structures with more than two nodes, the receptance notation $\mathbf{Y}$ is preferred over the dynamic stiffness $\mathbf{Z}$ notation, since the dynamic stiffness only comprises element behaviour. Usually $\mathbf{Z}$ is a sparse matrix whereas $\mathbf{Y}$ is generally a full matrix. In figure 3.9, the difference for the system discussed in this section is visualized.

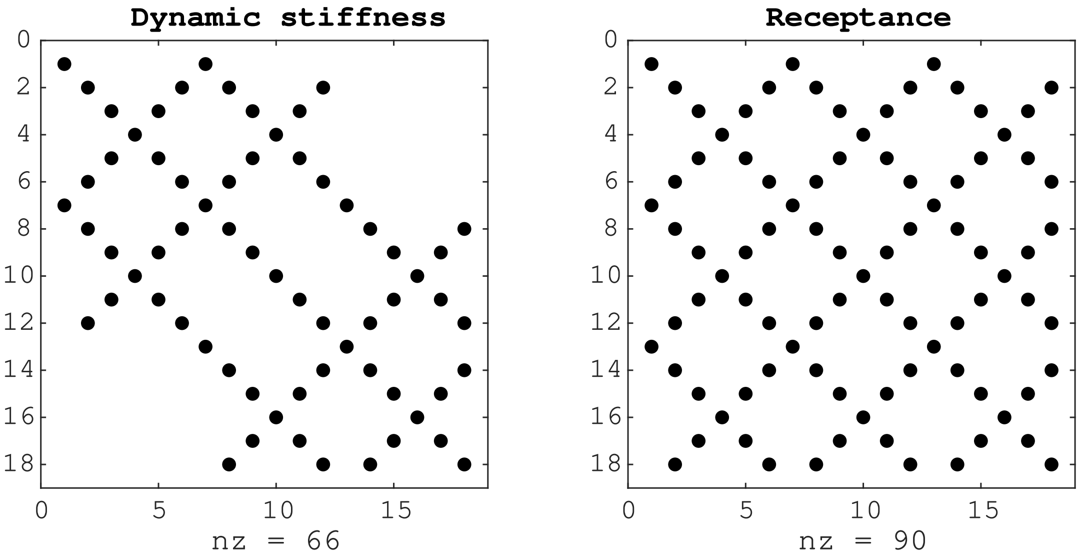

FIGURE 3.9: Sparsity pattern of the 18x18 Stiffness and Receptance Matrix.

**Misschioen nog iets meer in depth hierover? bijlage?**

### 3.3.1 Varying mass ratio for transfer receptance

In figure 3.10 and 3.11 the influence of the mass of the isolator can be discerned for transfer and driving point receptance.

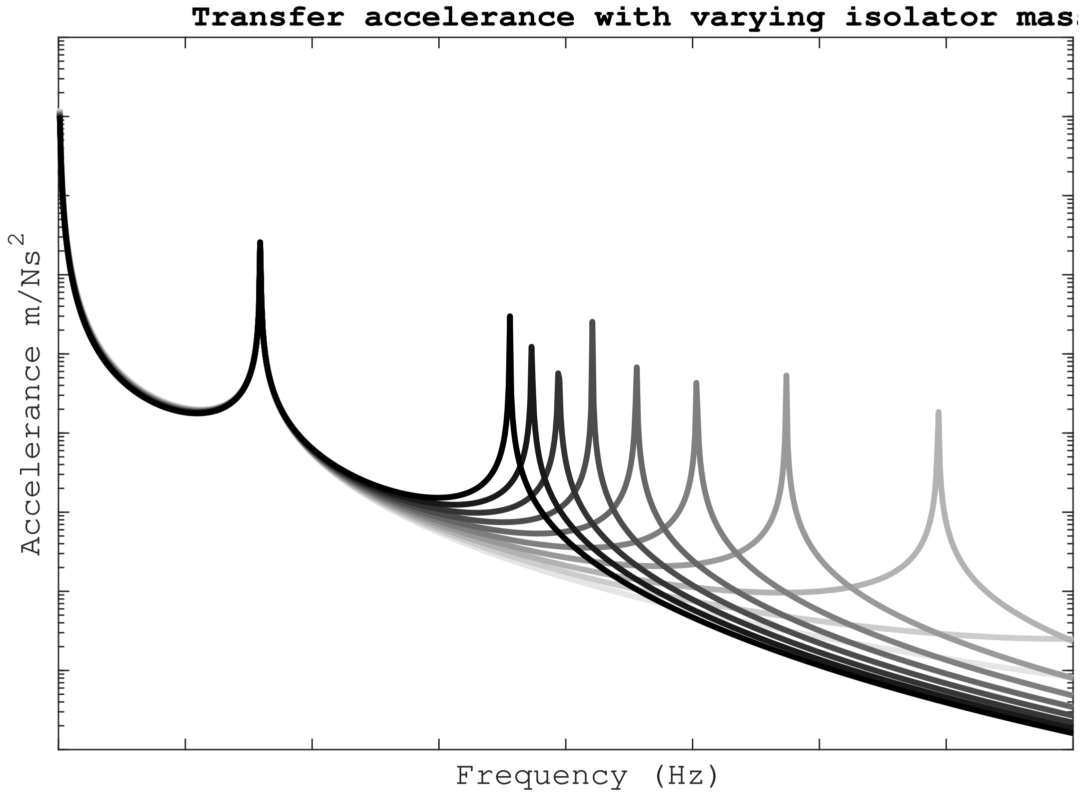

FIGURE 3.10: Transfer receptance with varying isolator mass. The lighter the line, the lighter the isolator mass.

**Observation**

As expected, the first resonance peak is not influenced by isolator mass. The higher the isolator mass, the lower the second resonance frequency. No antiresonance is visible. After the second resonance frequency, the accelerance slowly decreases, however, for a lighter mass, the accelerance is higher.

**Explanation**

The fact that the isolator mass does not influence the first resonance peak can be explained by the mode shape at the frequency of the first resonance peak. In this mode shape, $M_1$ and $M_2$ are moving equal but opposite in axial direction creating an equal but opposite force on the point mass of $M_{iso}$, which in turn makes $M_{iso}$ stationary. A stationary mass does not influence the frequency response. The moving of the second resonance peak can also be explained by the mode shape. In this mode shape, $M_1$ and $M_2$ are stationary and the $M_{iso}$ oscillates back and forth in axial direction. By constant stiffness, a higher mass will lower the resonance frequency. The absence of antiresonances can be explained by inspecting the accelerance equation 3.21.

$$\mathbf{Y}(\omega) = \frac{\mathbf{u}(\omega)}{\mathbf{f}(\omega)} \tag{3.21}$$

Antiresonance, where **Y** approaches zero, is caused by **u**, the displacement, going to zero. This will never happen for transfer stiffness in this system.

The lighter isolator mass keeps the accelerance at a higher value for higher frequencies because the lighter the isolator mass, the less energy is absorbed at this point and is transferred from $M_1$ to $M_2$.

### 3.3.2 Varying mass ratio for driving point receptance

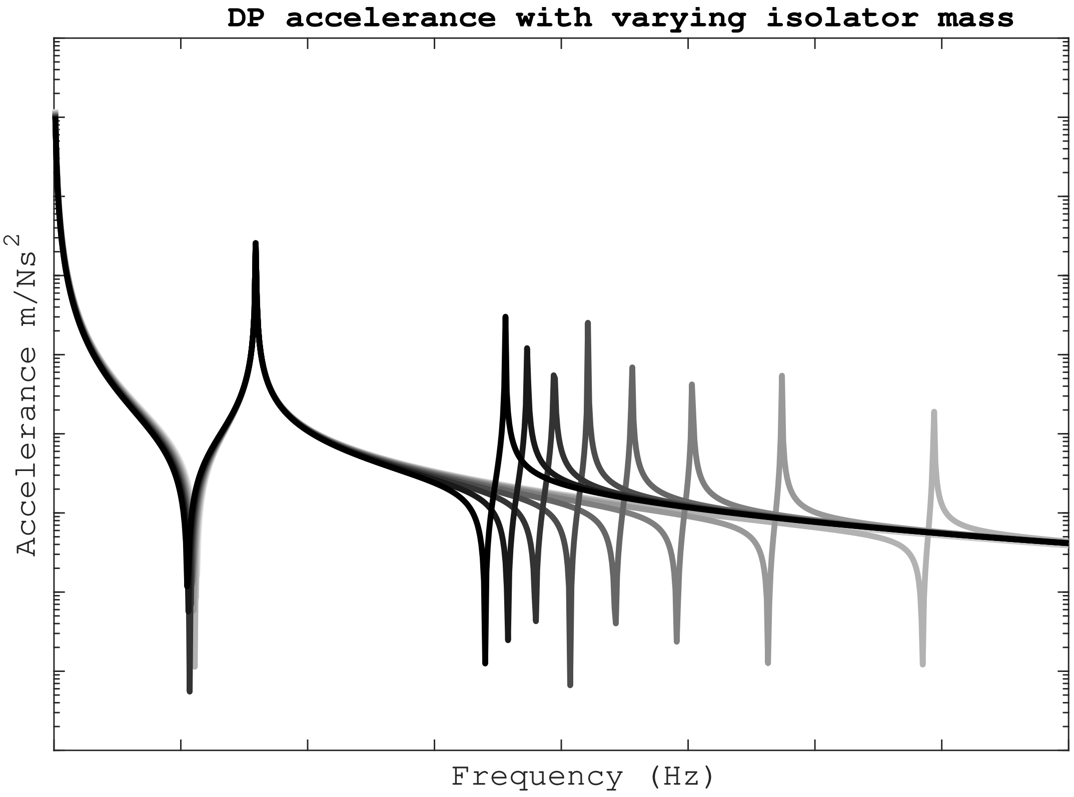

FIGURE 3.11: Driving point receptance with varying isolator mass. The lighter the line, the lighter the isolator mass.

**Observation**

As expected, the first resonance peak is not influenced by isolator mass. The higher the isolator mass, the lower the second resonance frequency. Antiresonance is visible. After the second resonance frequency, the accelerance slowly decreases and converges to one value for varying mass.

**Explanation**

In this case the first resonance-antiresonance pair is not influenced by the isolator mass as well. This can also be explained by the mode shapes as in section 3.3.1. The same explanation for the second resonance-antiresonance pair, where the $M_{iso}$ oscillates between the stationary $M_1$ and $M_2$ also holds. Different in this graph is the antiresonances which do occur for driving point FRFs.

# Chapter 4

# Practice

## 4.1 Introduction

With the basic knowledge from chapter 3 a grounded experiment can be conducted. In this experiment, four measurement campaigns are carried out to compare the method of Full Decoupling of the substructures **A** , **I** and **B**, the Inverse Substructuring method and the Improved Inverse Substructuring method. In section 4.2, the general setup of the measurement campaigns are explained, the results are shown in section 4.4 and a discussion on the practice is held in 4.5.

Firstly, a measurement campaign is conducted to determine the dynamic properties of the Isolator by FD, InvSub and ImInvSub. Secondly, these properties are plugged into a validation structure to see if the propositions on improvement of inverse substructuring have any effects.

## 4.2 Measuring the dynamic properties of the Isolator

### 4.2.1 General setup

To measure the dynamic stiffness properties of rubber isolators, it is clamped between two aluminium crosses manufactured by a water jet cutter. The center sinkhole for the M10 nut is milled. The rubber isolator is placed between the aluminium crosses, and the washer and nut are screwed on the thread. The nut is secured using a torque wrench set to 15Nm. This is the maximum reliable torque that the torque wrench can measure.

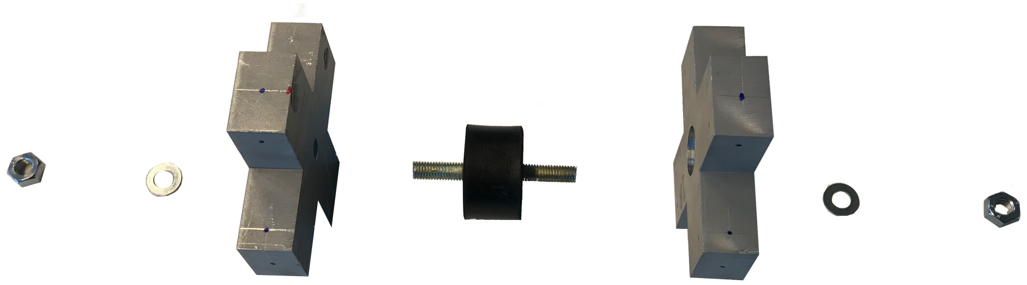

FIGURE 4.1: Exploded view from the assembled **AIB** system with from left to right: nut-washer-transmission simulator-ruber isolator-transmission simulator-washer-nut.

To measure the response to an impact, sensors are adhered to the structure on four places as seen in figure 4.2.

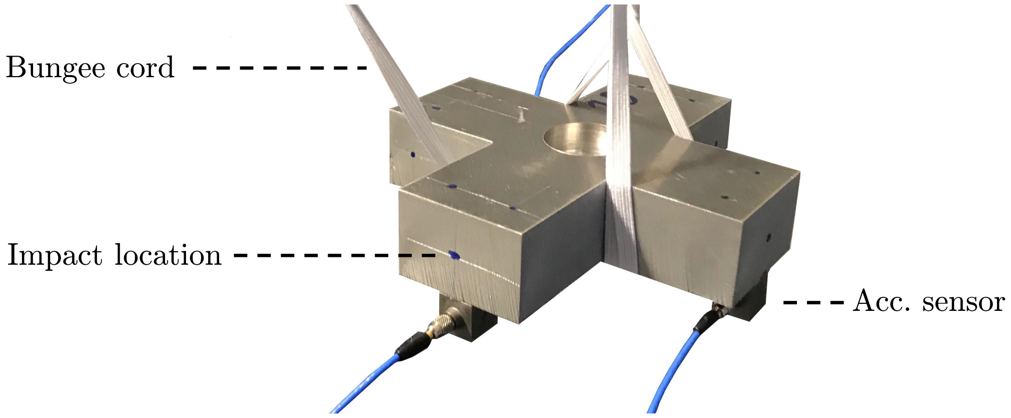

Figure 4.2: Single transmission simulator (TS) cross hanged from a bungee cord. Three sensors are adhered the TS and impact locations are visible.

The structure is struck with an impact hammer with a force measurement sensor on pre-marked locations on the structure to measure a response to a known input.

### 4.2.2 Used materials

**Transmission simulators** The transmission isolators are water jet-cut crosses from aluminium. The nut hole is sunk with a mill. On this transmission simulators, the 32 impact locations are marked by permanent marker.

**Vibration isolator** The vibration isolator is rubber with a depth of 50 mm and a length of 30 mm.

**Fastening** To perform measurements on the characteristics of the vibration isolator, it must be mounted to the transmission simulators. These TMs are fastened to the vibration isolator by a washer and M10 nut by use of a calibrated torque wrench every measurement campaign to rule out inconsistencies caused by fastening torque.

Figure 4.3: Materials to fasten transmission simulator to the vibration isolator From left to right: Nut, washer and calibrated torque wrench.

For measuring the frequency response of solely the assembly of transmission simulators and vibration isolator, it must be mechanically decoupled from its environment or be in 'free-free' conditions. Free free conditions are very achievable in computer simulations however in practice some considerations must be made. The method used in this experiment is suspending the assembly **AIB** from low stiffness bungee cords where the free-free resonance frequency of the assembly **AIB** is separated from the rigid body mode frequencies of the suspension setup. A rule of thumb is that these ratios should be apart by minimum a factor of 10 [10]. In this experiment, the free-free resonance frequency is in the multi kHz range, and the rigid body mode frequency is $\pm 2$ Hz, so these frequencies are separated sufficiently.

Lastly, the sensors need to be adhered to the transmission simulators. Multiple adherents can be used, such as loctite, xc60 or bee wax. In this case a sensor mount with loctite is used. The easy removal of the sensors is a good characteristic for the roving measurement setup of the second campaign as explained in 4.2.4.

**Sensors and Data acquisition** The sensors used are PCB356 A32 piezo electric accelerometers and the impact hammer is a PCB086 modal hammer. Both sensors and hammer are connected to a Müller-BBM PAK MKII data acquisition system.

**Software** A measurement campaign consists of three steps: Preparation, Measurement and Analysis. For the first two steps the in-house developed application DIRAC is used. In this software, the engineer prepares a measurement by loading a CAD file from the measurement setup in the software and placing impact- and sensor locations on the object. When this is completed, the 'Measure' module is started. During the measurement DIRAC will share live feedback about the model quality, using the sensor specifications and the geometry of the experiment.

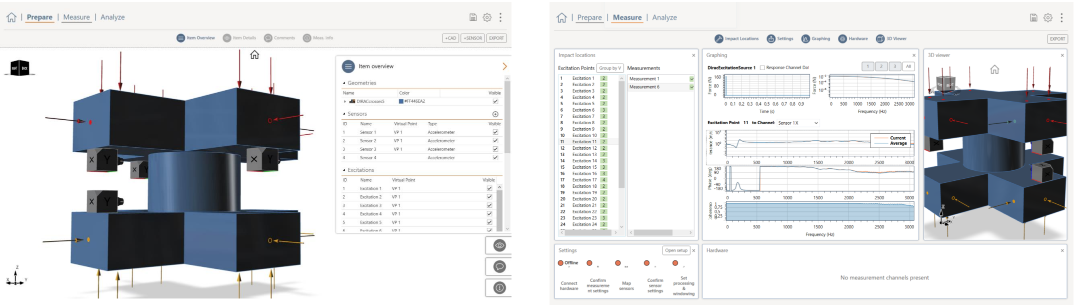

FIGURE 4.4: Screenshots of the DIRAC software (Alpha Version 0.1.0.107).
Left: The Prepare module. Right: The Measure module.

The DIRAC software is also capable of performing analysis on the measurements. However, it is in the Alpha development phase, so the data is exported to MATLAB and analysed by the VIBES toolbox for MATLAB add-on. In the VIBES toolbox, the impacts and sensors are converted to virtual points and the FRFs are created.

### 4.2.3 Campaign 1: Dynamic stiffness of the crosses

To perform the full decoupling method in dynamic substructuring, the dynamics of all but one structure is required to be known. In this research, the assembled system **AIB** is measured, and the crosses **A** and **B** are measured separately so these dynamics can be subtracted from the assembled system to obtain the dynamics of solely **I**, the isolator.

Three sensors are used, as seen in figure 4.2. Sixteen impact are exerted on the structure. Using the nine response channels and sixteen input channels, a virtual point is created at the heart of the interface of the cross with the (non present) isolator to form a 6x6 FRF matrix.

### 4.2.4 Campaign 2: Roving measurement of the isolator

In this measurement campaign the transmission simulators and vibration isolator are assembled. The sensors are placed on the transmission simulator as can be seen in figure 4.2. 16 impacts on side **A** are performed to measure driving point stiffness, and 16 impacts on side **B** are performed to measure transfer stiffness. Then the sensors are removed from transmission simulator **A** and placed on **B** to repeat the measurement.

### 4.2.5 Campaign 3: Dynamics of the A structure

For validation, the rubber isolator dynamics using different substructuring techniques are plugged into a validation structure. To make use of substructuring techniques, the dynamics of all individual components of the assembly are required. This means that the A-frame is measured separately. Three sensors are used to create a Virtual point on the future interface between the rubber isolator and this A-structure, while one sensor will be used for validation of the different substructuring methods. This will result in a 6x9 FRF matrix with the first 6x6 entries consisting of Virtual Point channels and refchannels, and the last three channels will be real sensor channels excited by virtual refchannels of the virtual point as can be seen in figure 4.6

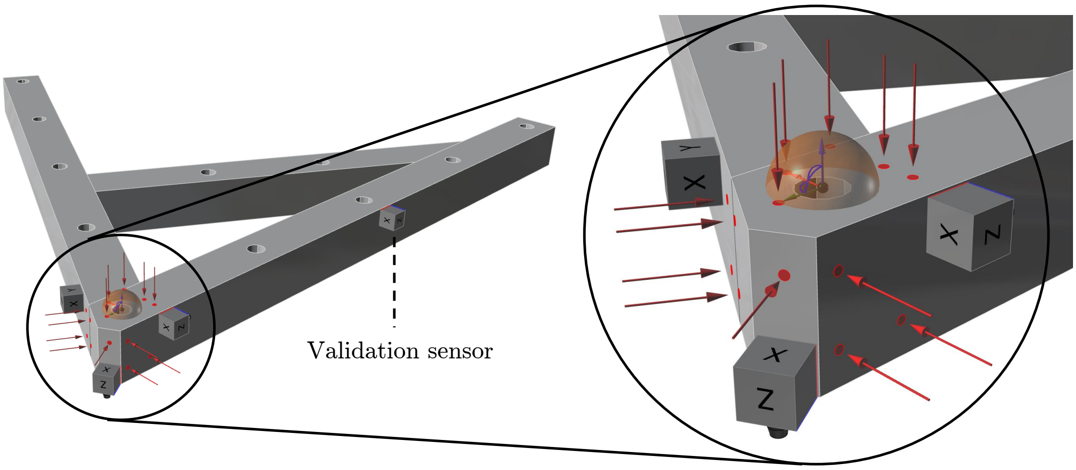

FIGURE 4.5: Left: The A-structure with the validation sensor on the far end. Right: Zoomed in view on the impacts and sensors used for creating the virtual point, visualized by an orange ball.

$$
\mathbf{Y}^{Astruct} = \begin{array}{cl}
\overbrace{\begin{array}{cccccc} T_x & T_y & T_z & R_x & R_y & R_z \end{array}}^{\text{Six Virtual RefChannels}} & \\
\left[\begin{array}{cccccc} \; & \; & \; & \; & \; & \; \\ & & & & & \\ & & & & & \\ & & & & & \\ & & & & & \\ & & & & & \\ & & & & & \\ & & & & & \\ & & & & & \end{array}\right] &
\begin{array}{l}
\left.\begin{array}{c} T_x \\ T_y \\ T_z \\ R_x \\ R_y \\ R_z \end{array}\right\} \text{Six Virtual Channels} \\
\left.\begin{array}{c} T_x \\ T_y \\ T_z \end{array}\right\} \text{Three real Sensor Channels}
\end{array}
\end{array}
$$

FIGURE 4.6: FRF matrix of the A structure built from virtual and real channels.

### 4.2.6 Campaign 4: Measurement of the validation structure

Lastly, a validation measurement is carried out by impacting a transmission simulator attached to the rubber isolator attached to the A-structure. The three components are measured separately so this assembly can be fully reconstructed using dynamic substructuring and compared with a validation measurement where the different components are connected in the real world.

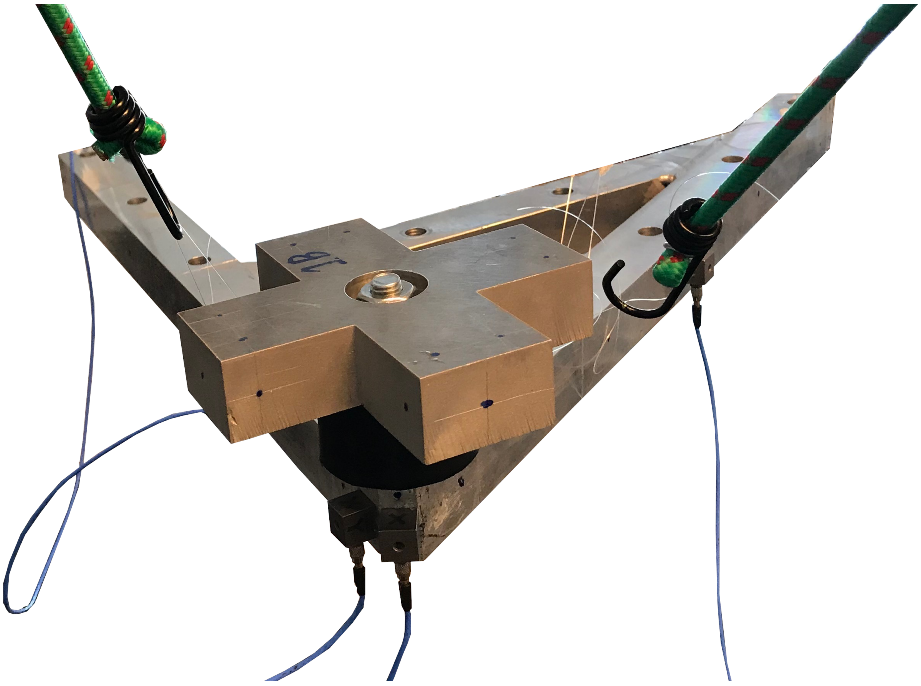

FIGURE 4.7: The validation measurement assembly

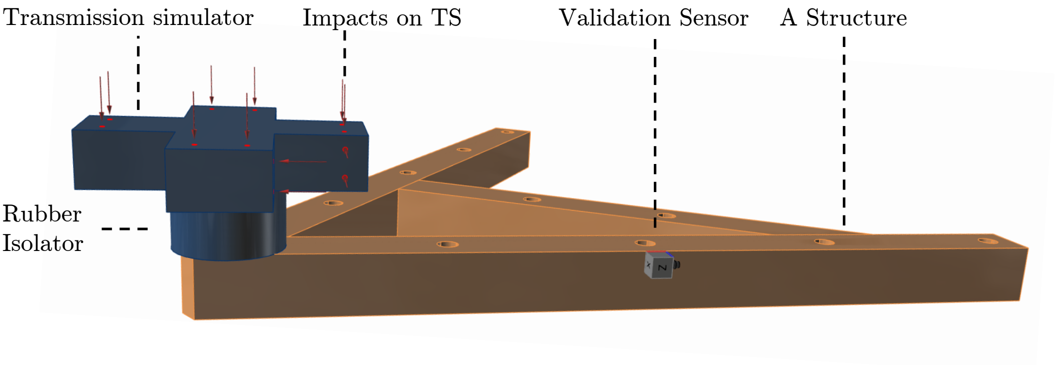

FIGURE 4.8: The assembly for the validation measurement as built prior to the experiment.

## 4.3 Data Processing

Classical FRFs can be exported from DIRAC in .mat format for use in MATLAB in combination with the VIBES toolbox for MATLAB. The FRFs are not directly suited for use in this toolbox, so a converting script is utilised to create FRFMatrix objects since this object type is used heavily in processing data in the VIBES toolbox. From the Classical FRF data, a virtual point transformation is performed to make decoupling of substructures possible.

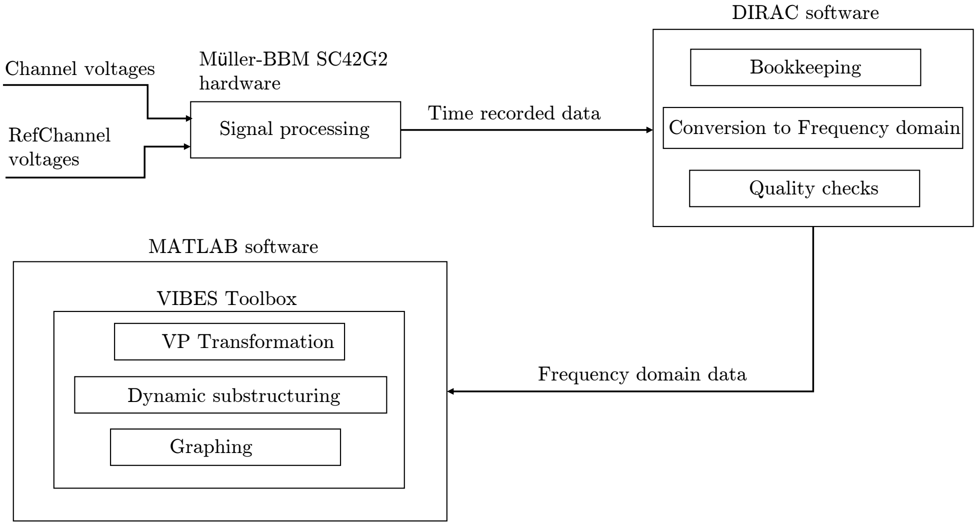
DIRAC software
Müller-BBM SC42G2 hardware
Channel voltages
Bookkeeping
Signal processing
Time recorded data
RefChannel voltages
Conversion to Frequency domain
Quality checks
MATLAB software
VIBES Toolbox
VP Transformation
Frequency domain data
Dynamic substructuring
Graphing

FIGURE 4.9: The dataflow from the sensors (channel voltages) and impacthammer (refchannels) to the graphing

The accelerometer sensors connect to the Müller-BBM signal processing box with three wires, one for each direction (x,y and z). The voltages in these wires range from 0-10V which change due to the piezoelectric effect. On the tip of the impact hammer, a load cell is placed. This load cell is connected to the same signal processing unit. This box converts these voltages in directional accelerations or impact forces and sends this data to a personal computer over an Ethernet cable.

DIRAC software then handles the rest of the signal processing. This means to a conversion the frequency domain and signal conditioning.

The frequency domain data is imported in Matlab and the VIBES toolbox to create VirtualPoints. The first step is to convert the structured data from Dirac to a format suitable for the VIBES toolbox. Then the location of the VPs are determined. The correct channels of the measurement are allocated to the correct VP by means of an interface deformation matrix and the VP FRF matrix is calculated. This is reviewed more in depth in section 2.3.2, but quickly recapped here. The measured FRF matrix Ymeasured is transformed in the virtual point FRF matrix Y virtual by means of two transformation matrices: Tu to transform the displacments of the sensors to the virtual point and Tf to transform the forces exerted by the impact hammer to virtual forces on the virtual point location. These transformation matrices are built from geometric information that relate the position of the sensors and impacts to the location of the virtual point.

$$\mathbf{Y}_{virtual} = \mathbf{T}_u \mathbf{Y}_{measured} \mathbf{T}_f^T \tag{4.1}$$

$$\mathbf{T}_u = \left(\mathbf{R}_u^T \mathbf{R}_u\right)^{-1} \mathbf{R}_u^T \quad \text{and} \quad \mathbf{T}_f^T = \mathbf{R}_f \left(\mathbf{R}_f^T \mathbf{R}_f\right)^{-1} \tag{4.2}$$

In which

$$\mathbf{R}^i = \left[\mathbf{e}^T | (\mathbf{r}^i \times \mathbf{e})^T\right] \tag{4.3}$$

Where **e** and **r** are the geometric properties as depicted in figure 2.9.

## 4.4 Results

In this subsection the results of the experimental measurements are discussed. In 4.4.1 and 4.4.2 the quality of the measurements are shown. In 4.4.4 the three substructuring methods are compared to a validation measurement.

### 4.4.1 Dynamics of the Transmission Simulators

To conclude that the measurements were performed correctly the dynamic stiffness of the crosses (transmission simulators: from now on TS) is inspected. One does expect this aluminium TS to be so stiff to not show any dynamic behaviour in the frequency of interest. If one checks the equation for dynamic stiffness **Z** it is expected that only the mass of the TS is of influence which is a flat line in the frequency domain.

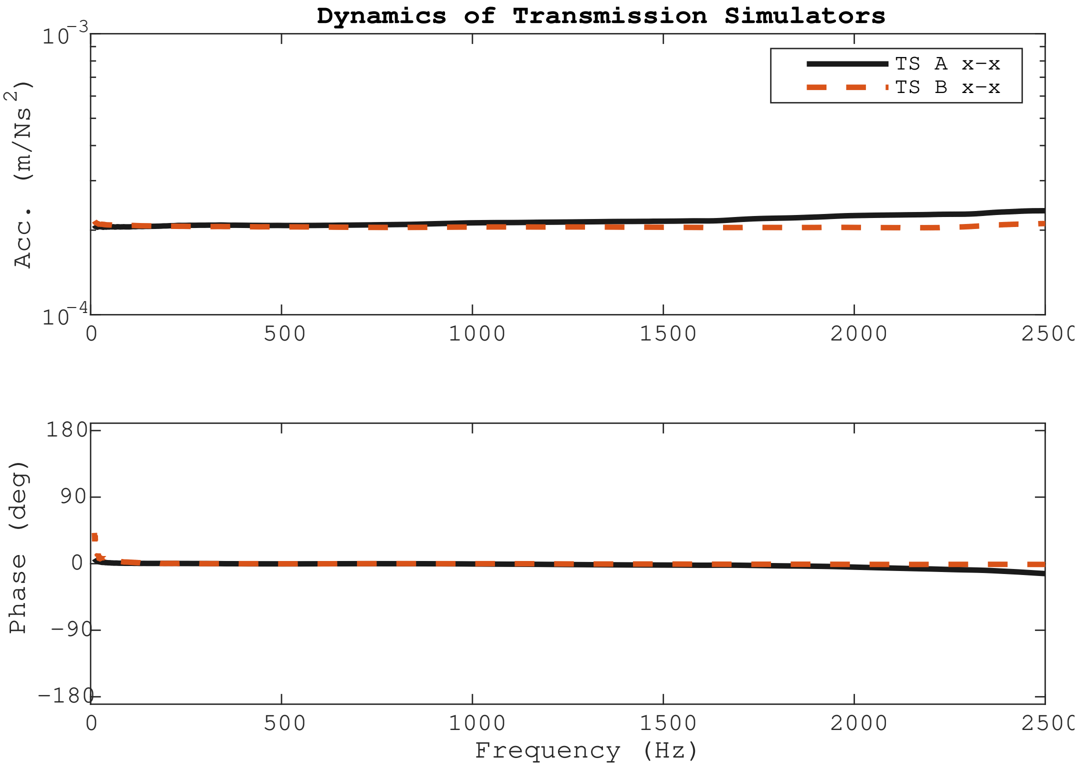

FIGURE 4.10: Accelerance of the TS in translational x-direction. No dynamics in the frequency range of interest are observed.

Which can be seen to be true for both transmission simulators A and B.

### 4.4.2 Dynamics of the rubber vibration isolator

In this section the dynamics of the rubber isolator are obtained by decoupling the dynamics of the TM from the assembly. Three FRF-matrices are required for this operation namely the FRF-matrix of the assembly, (isolator with transmission simulators), and the FRF-matrices of the two transmission simulators as explained in section 4.2.1. The decoupling procedure using virtual points is explained in section 2.3. After decoupling, one obtains the Fully Decoupled FRF matrix of the rubber isolator. In this thesis it is compared with the Inverse Substructured and the Improved Inverse Substructured variant. How these variants are obtained is explained in section 2.4.2.

But first things first. It is required to check if the measurement campaign was caried out carefully with concise impacts and sensor locations. A way to check this is to assume a symmetric assembly and see if the driving point accelerances of **A** and **B**, and the transfer accelerances from **A** to **B** and **B** to **A** are similar. An example of a comparison can be seen in figure 4.11.

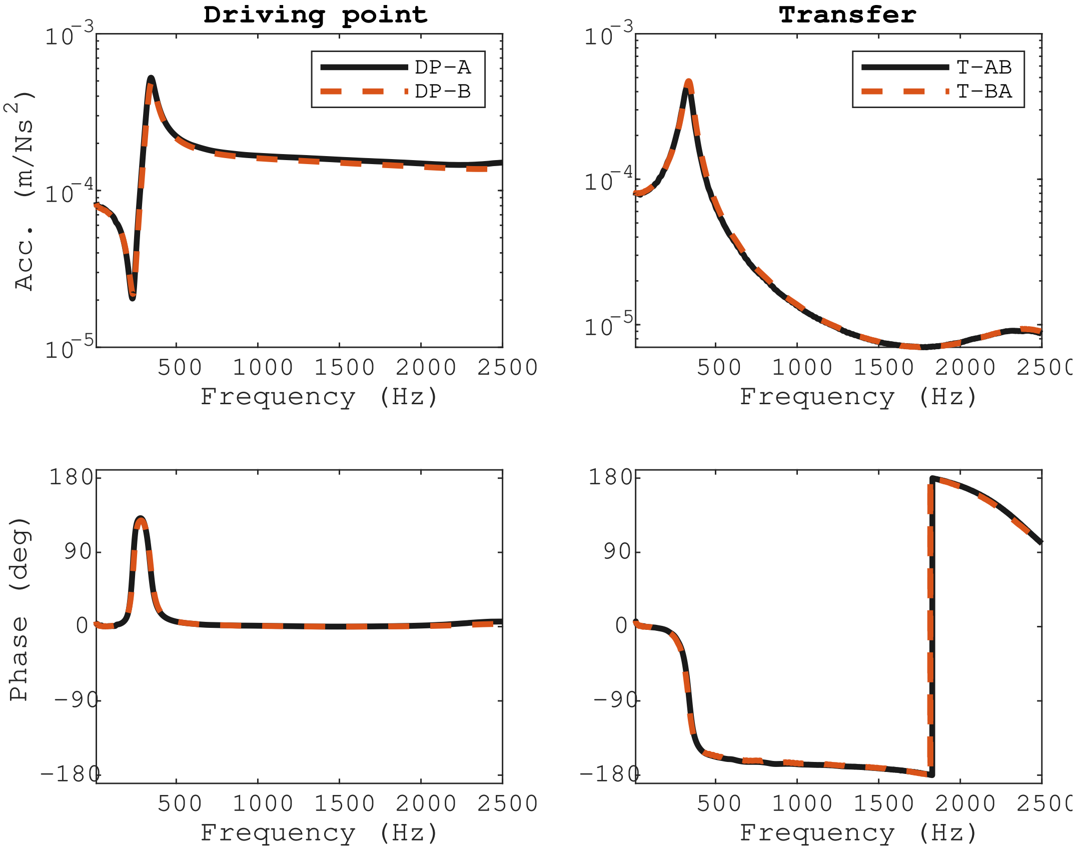

FIGURE 4.11: Accelerance of the Assembly in translational y direction. Driving point A and B, and Transfer accelerance from A to B and B to A is checked to check if these measurements do overlap as expected for this symmetric assembly.

With this consistency checked, one can perform the decoupling procedure. A quality check to see if this decoupling procedure is carried out correctly the dynamic stiffness of the vibration isolator is inspected in directions which are symmetric: x and y. If these plots overlap the decoupling procedure is carried out succesfully.

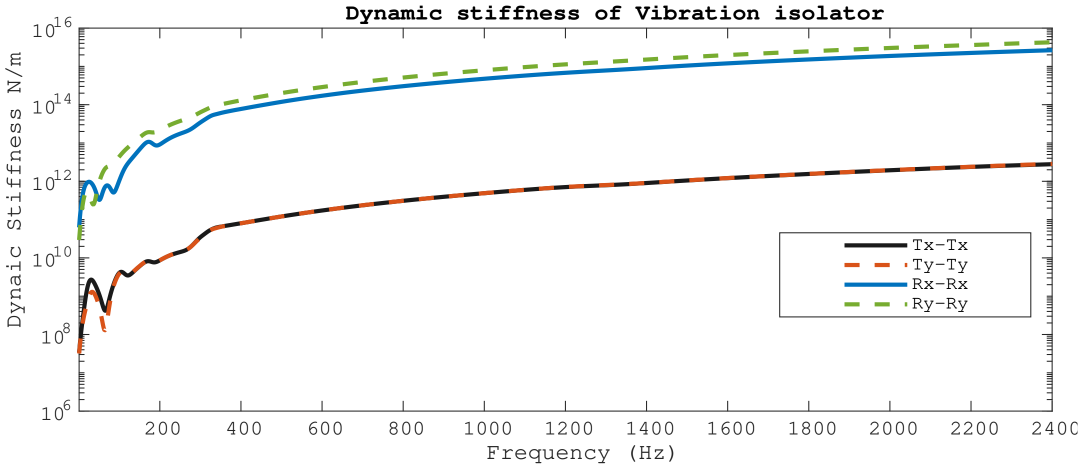

FIGURE 4.12: Dynamic stiffness of the vibration isolator in symmetric translational and rotational directions.

### 4.4.3 Dynamics of the A-structure

To get a feeling for the dynamics of the A-structure a FRF is plotted. However by just glancing over an FRF the quality of the measurement is not ensured yet. To check the quality it is not possible to use symmetry of this object because it is not symmetric. To ensure the quality of this measurement two other metrics are inspected: sensor and impact consistency to ensure a good quality virtual point.

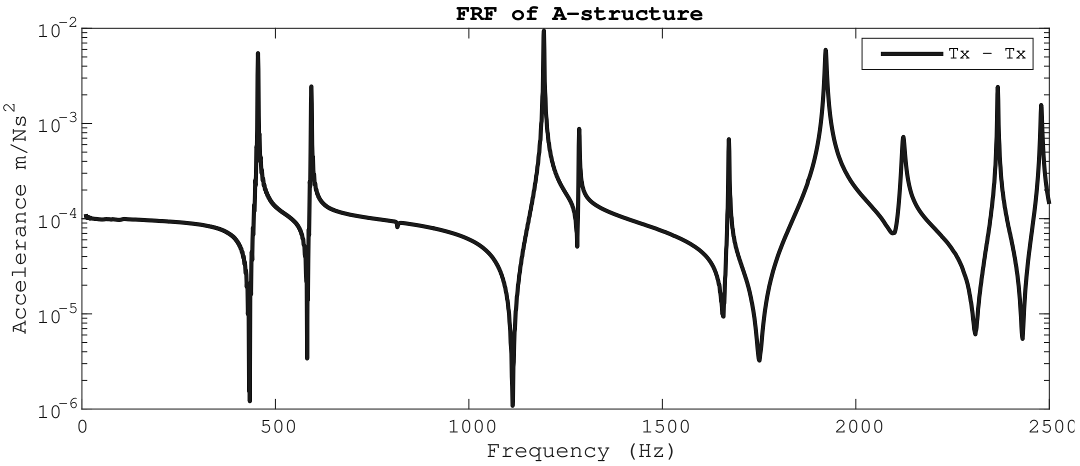

FIGURE 4.13: Dynamic stiffness of the vibration isolator in symmetric translational and rotational directions.

To perform the virtual point transformation one requires suitable sensor and impact locations. This metrics can be quantified in a value called the impact and sensorchannel consistency. This metric will take a value between zero and one. A one indicates that the sensor can describe the dynamics of the virtual point very well, while a zero means that it is not contributing to improving the dynamics of the virtual point. For calculation of this consistency metric refer to [19].

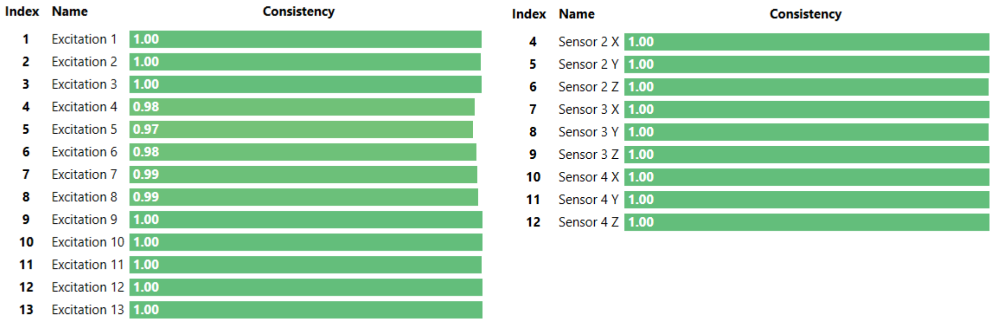

| Index | Name | Consistency |
|---|---|---|
| 1 | Excitation 1 | 1.00 |
| 2 | Excitation 2 | 1.00 |
| 3 | Excitation 3 | 1.00 |
| 4 | Excitation 4 | 0.98 |
| 5 | Excitation 5 | 0.97 |
| 6 | Excitation 6 | 0.98 |
| 7 | Excitation 7 | 0.99 |
| 8 | Excitation 8 | 0.99 |
| 9 | Excitation 9 | 1.00 |
| 10 | Excitation 10 | 1.00 |
| 11 | Excitation 11 | 1.00 |
| 12 | Excitation 12 | 1.00 |
| 13 | Excitation 13 | 1.00 |

| Index | Name | Consistency |
|---|---|---|
| 4 | Sensor 2 X | 1.00 |
| 5 | Sensor 2 Y | 1.00 |
| 6 | Sensor 2 Z | 1.00 |
| 7 | Sensor 3 X | 1.00 |
| 8 | Sensor 3 Y | 1.00 |
| 9 | Sensor 3 Z | 1.00 |
| 10 | Sensor 4 X | 1.00 |
| 11 | Sensor 4 Y | 1.00 |
| 12 | Sensor 4 Z | 1.00 |

FIGURE 4.14: Left: Impact consistencies. Right: Sensorchannel consistencies.

These sensor consistencies show that the measurement is carried out in a careful manner with sensors on correct locations securely fastened. These impact consistencies show that the impacts were intended and placed on correct locations without much variation due to the human nature of executing an impact.

### 4.4.4 Comparing FD, InvSub, and ImInvSub to a validation measurement

To compare the three variants of substructuring to a validation measurement, several mathematical operations in the form of decoupling and coupling of substructures is required. Firstly, the TS crosses are decoupled from the isolator to obtain the dynamic stiffness of solely the isolator.

Next, the isolator needs to be coupled to one transmission simulator and the A structure.

In this coupling procedure is where the difference between different methods of modelling the isolator is implemented as can be seen in figure 4.15. For the model of I, the three variants of FD, InvSub and ImInvSub are used.

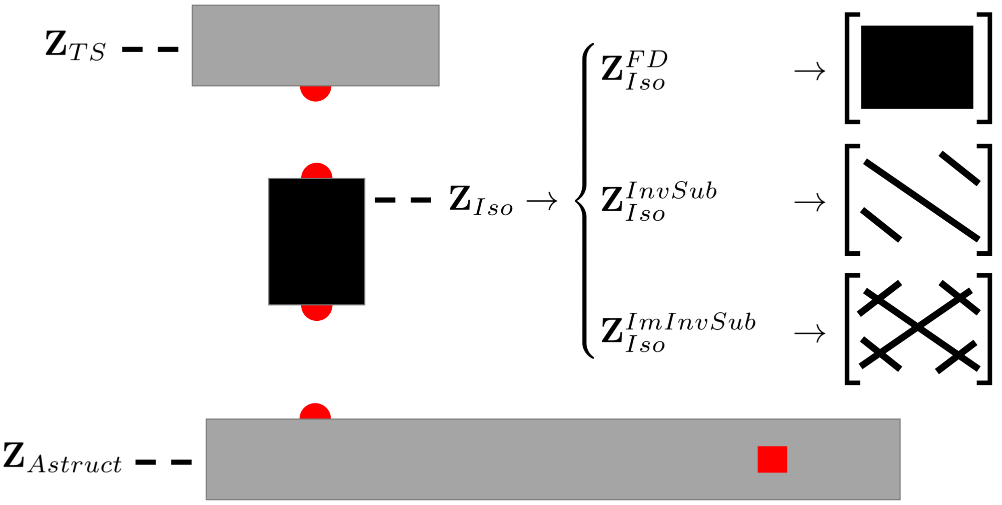
$\mathbf{Z}_{TS}$
$\mathbf{Z}_{Iso} \rightarrow$
$\mathbf{Z}_{Iso}^{FD} \rightarrow$
$\mathbf{Z}_{Iso}^{InvSub} \rightarrow$
$\mathbf{Z}_{Iso}^{ImInvSub} \rightarrow$
$\mathbf{Z}_{Astruct}$

FIGURE 4.15: The substructures used in the validation assembly. For the dynamic stiffness of the isolator three models are used and the sparsity of the dynamic stiffness matrices is displayed.

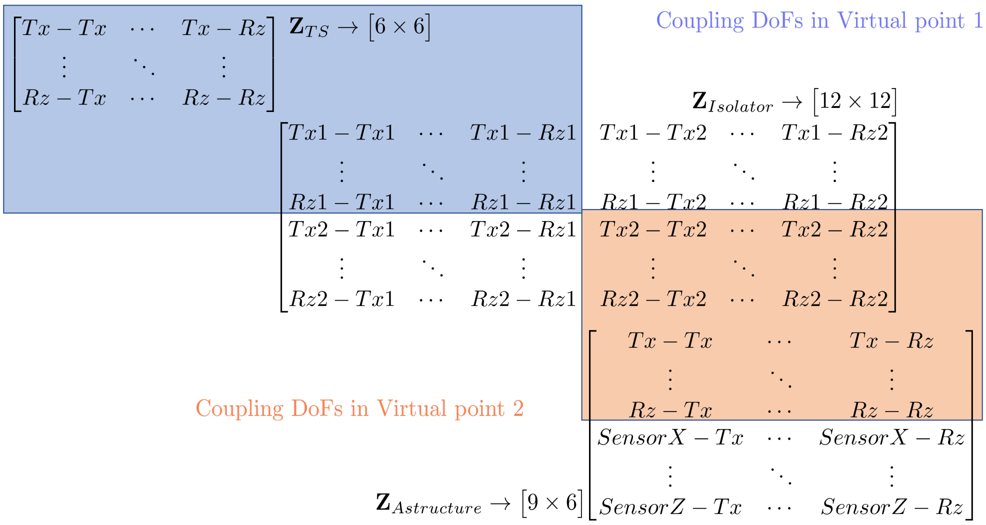
Coupling DoFs in Virtual point 1
Coupling DoFs in Virtual point 2
$\mathbf{Z}_{TS} \rightarrow [6 \times 6]$
$\mathbf{Z}_{Isolator} \rightarrow [12 \times 12]$
$\mathbf{Z}_{Astructure} \rightarrow [9 \times 6]$
$Tx - Tx$ … $Tx - Rz$
$Rz - Tx$ … $Rz - Rz$
$Tx1 - Tx1$ … $Tx1 - Rz1$ $Tx1 - Tx2$ … $Tx1 - Rz2$
$Rz1 - Tx1$ … $Rz1 - Rz1$ $Rz1 - Tx2$ … $Rz1 - Rz2$
$Tx2 - Tx1$ … $Tx2 - Rz1$ $Tx2 - Tx2$ … $Tx2 - Rz2$
$Rz2 - Tx1$ … $Rz2 - Rz1$ $Rz2 - Tx2$ … $Rz2 - Rz2$
$SensorX - Tx$ … $SensorX - Rz$
$SensorZ - Tx$ … $SensorZ - Rz$

FIGURE 4.16: The three **Z** matrices with overlapping rectangles for coupling DoFs used for dynamic substructuring.

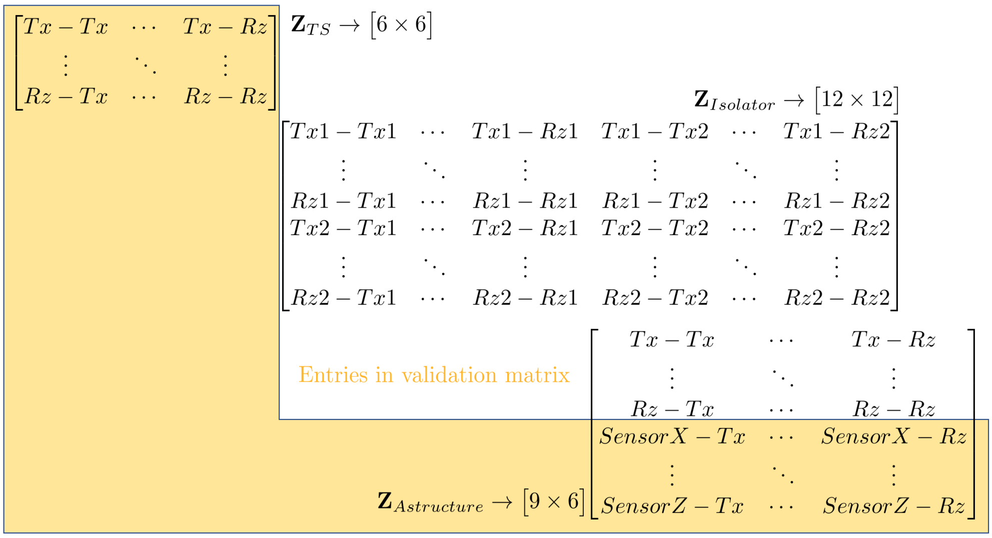
$\mathbf{Z}_{TS} \rightarrow [6 \times 6]$
$\mathbf{Z}_{Isolator} \rightarrow [12 \times 12]$
$\mathbf{Z}_{Astructure} \rightarrow [9 \times 6]$
Entries in validation matrix
$Tx - Tx$ … $Tx - Rz$
$Rz - Tx$ … $Rz - Rz$
$Tx1 - Tx1$ … $Tx1 - Rz1$ $Tx1 - Tx2$ … $Tx1 - Rz2$
$Rz1 - Tx1$ … $Rz1 - Rz1$ $Rz1 - Tx2$ … $Rz1 - Rz2$
$Tx2 - Tx1$ … $Tx2 - Rz1$ $Tx2 - Tx2$ … $Tx2 - Rz2$
$Rz2 - Tx1$ … $Rz2 - Rz1$ $Rz2 - Tx2$ … $Rz2 - Rz2$
$SensorX - Tx$ … $SensorX - Rz$
$SensorZ - Tx$ … $SensorZ - Rz$

FIGURE 4.17: The three substructures. The yellow rectangle shows what the validation matrix consists of.

### 4.4.5 Observations for translational input in x and y direction

In this section the resulting FRFs with different coupling techniques are observed for virtual translational input.

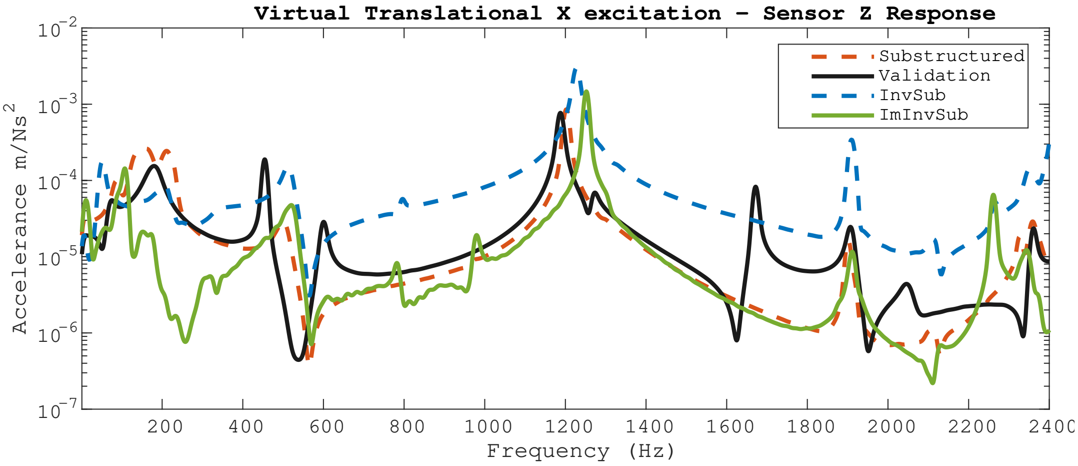

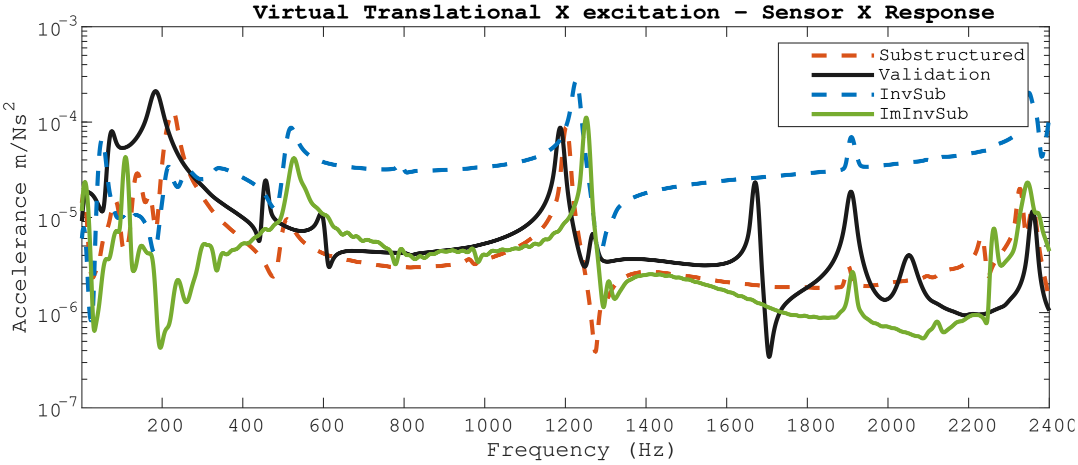

### Inverse substructuring overestimates accelerance

The inverse substructuring response 'measures' higher accerelance accros almost the whole frequency range.

**Explanation** The fact that inverse substructuring overestimates accelerance can be attributed to the fact that some relevant stiffness entries are removed from the $\mathbf{Z}$ matrix due to the operation of assuming diagonality. This reduced stiffness will result in a higher accelerance response accross the whole frequency range.

### Missing dynamics in substructuring

In the validation measurement more resonance and anti-resonance peaks show than in all substructured responses for example around 1650 Hz. This is not only true for the inverse substructuring methods but also for full decoupling.

**Explanation** There exist multiple reasons why certain dynamics are missed when constructing dynamics using FBS. In this case the assembly is too complicated to pinpoint to a certain mode or modeshape so a guess must be made. It is for example possible that a the rigidifying around an interface by using a virtual point is not justified and dynamics because of this flexibility are not present in substructured responses.

### Resonance peak shifts of inverse substructuring

One can see that the fully substructured response predicts resonance peaks the most accurate, while the inverse substructuring techniques predict a slightly higher frequency for the resonances.

**Explanation** Resonance peak shifts are discussed in section 4.4.1 and it was discovered that it is caused by either a difference in mass of the system or a difference in stiffness. If one firstly compares InvSub and ImInvSub to FD and can see that the resonance peaks shift to the right, so to a higher frequency. Physically this indicates a difference in the relation of mass to stiffness in which the mass is lower or the stiffness is higher as one can see in the relation to calculating resonance peaks:

$$\omega_n = \sqrt{\frac{k}{m}} \tag{4.4}$$

With $\omega_n$ the frequency at which resonance occurs. Both quantities are encapsulated in the dynamic stiffness quantity $\mathbf{Z}$ as shown by equation 3.1. Because for InvSub and ImInvSub the $\mathbf{Z}$ is drastically altered and it is tried that most important values are only taken into account this can slightly alter the solution for eigenvalues in and shift resonance peaks.

### Dynamics solely found in ImInvSub

Around 800 and 980 Hz the improved inverse substructured respons shows resonance peaking which is not present in the validation nor the fully substructered and inverse substructered response.

**Explanation** To find some dynamics only present in ImInvSub while it is not present in InvSub, FD or the validation is surprising and physically not expected. However, due to the mathematical operations, especially matrix inversion, small deviations can lead to miscalculated resonance peaks. This is most likely the case for unexpected dynamics in ImInvSub.

### Differences for low frequencies

For frequencies lower than 200 Hz the validation measurement does not remotely come close to the substructured techniques.

**Explanation** The used sensors are sensitive devices however it is possible that a desired signal to noise ratio is not achieved. This is because of the design of the accelerometers. The sensors contain a piezoelectric element that converts strain to a difference in electric potential. A known mass in the sensor moves around creating strain inside the piezo material causing a difference in electric potential which is detected by the data acquisition system. This sensor is best for measuring vibrations at higher frequencies because more changes in acceleration happen. At low frequency relatively more noise is present in the signal because less accelerations happen.

### 4.4.6 Observations for translational input in z direction

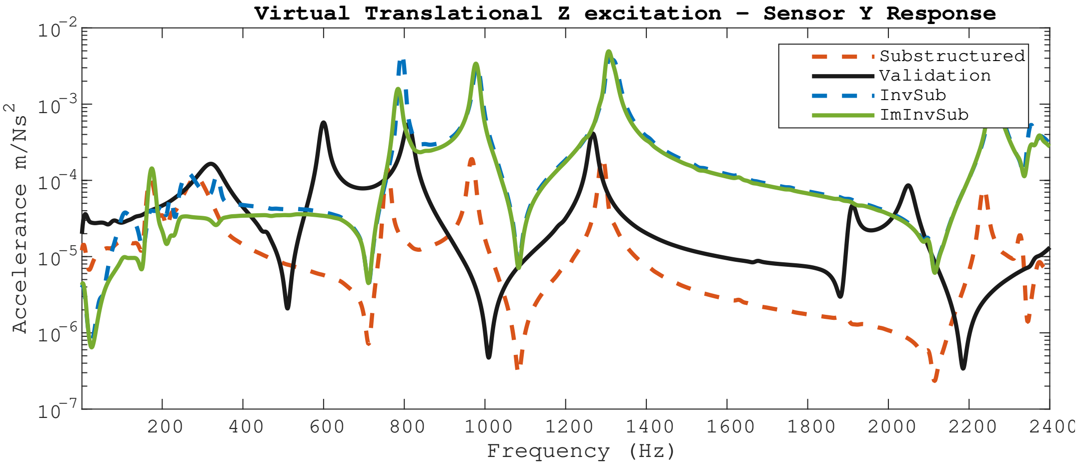

#### Inaccurate results for substructuring

The shape of the substructuring curve somewhat resembles the same shape of the validation measurement however across the whole frequency range the results are inaccurate. Resonances and antiresonances are miscalculated and the overall accelerance is not similar.

**Explanation** The substructured result does not come close to the validation because of multiple errors in executing the experiment presumably. It is so far off that not a single source can be pointed out but it is a combination of effects described in section 4.5.

**ImInvSub similar to InvSub** It is interesting to see that for excitation in Z direction, the ImInvSub response is more similar to InvSub than to FD or the validation compared to excitations in x and y direction.

**Explanation** This can be explained if one inspect the difference in stiffness matrices for InvSub and ImInvSub closely. One can see in the sparsity pattern that for the row of x and y excitations the crosscoupling term is added to the matrix for ImInvSub but for the row of the z excitation there is no crosscoupling term added so it is expected that these responses are quite similar.

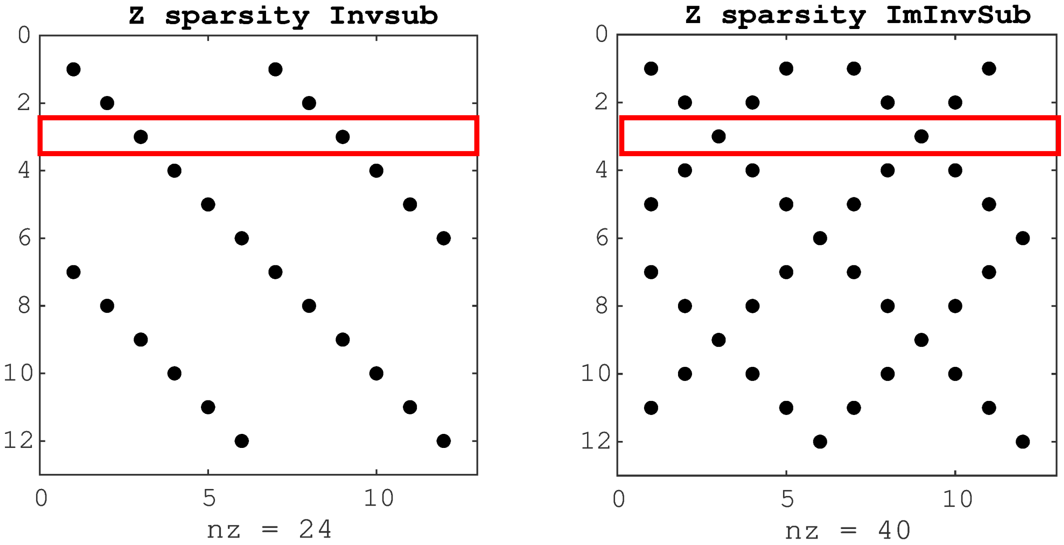

FIGURE 4.18: The sparsity pattern for InvSub and ImInvSub with the row for the impact in the Z-direction highlighted.

### 4.4.7 Observations for rotational input

In this section the resulting FRFs with different coupling techniques are observed for virtual rotational input.

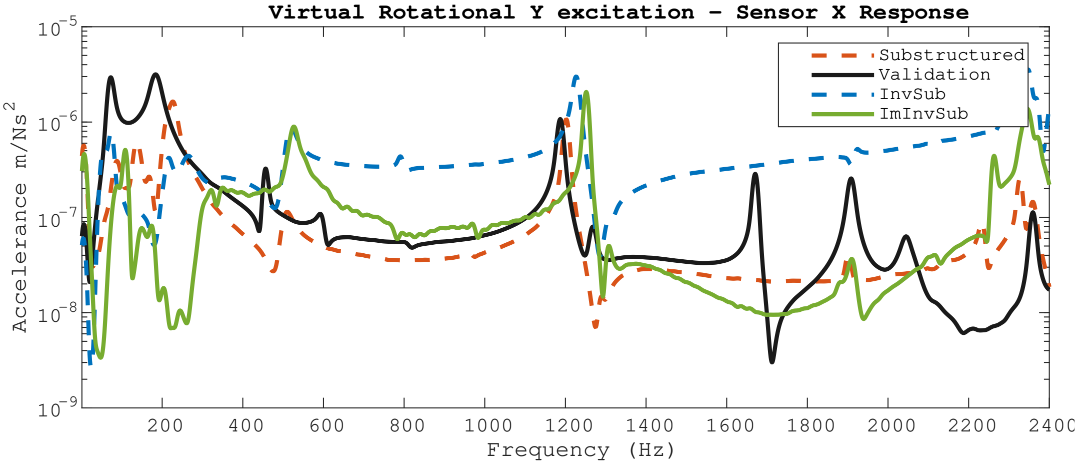

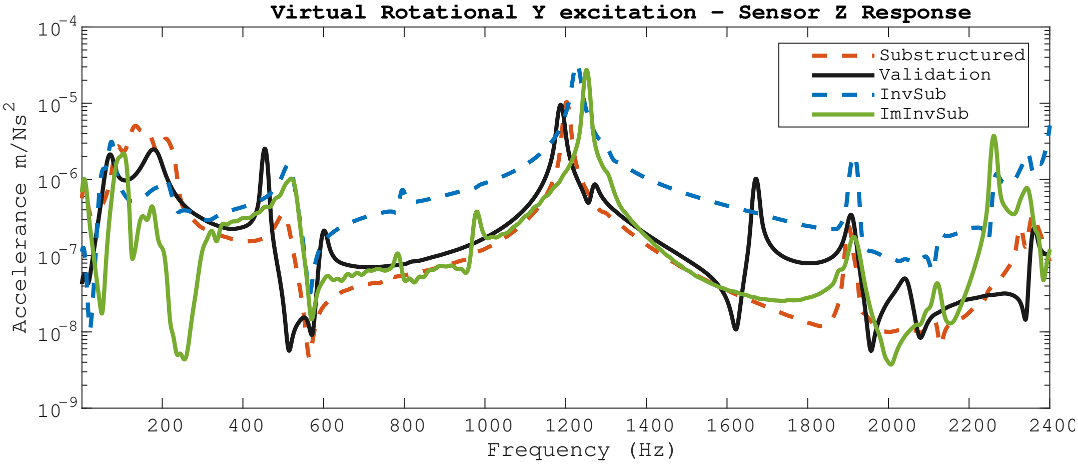

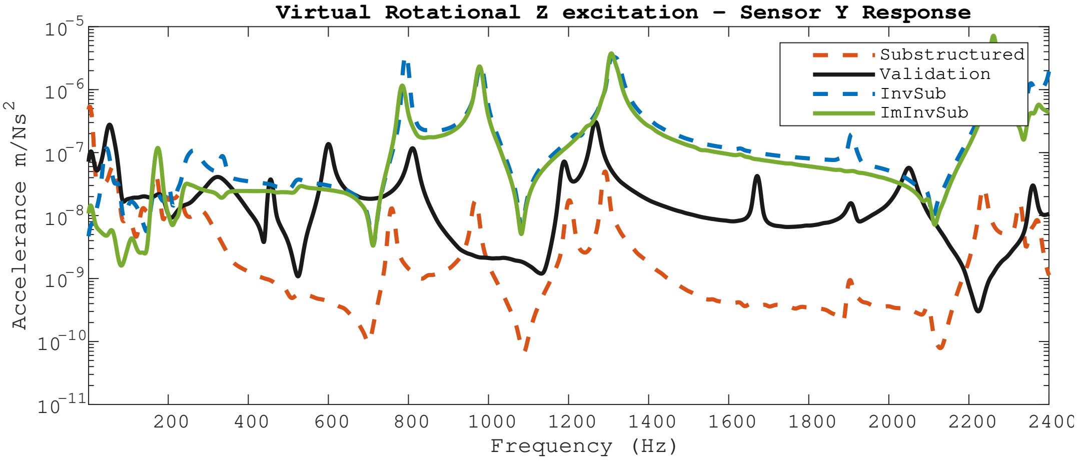

### Inverse Substructuring overestimates accelerance response in x and y direction

For the two graphs relating rotational excitation to sensor output in x and y direction, inverse substructuring overestimates accelerance.

**Explanation** This phenomenon can be expected because of the missing crosscoupling stiffness terms which makes the constructed rubber model not stiff enough which in turn shows as higher accelerance over almost the whole frequency range.

### Improved Inverse Substructuring over estimates accelerance response in z direction

While Improved Inverse Substructuring does a better way of predicting dynamic behaviour for response channels in x and y direction, it is closer to the overestimated InvSub response when checked for the z direction.

**Explanation** As mentioned at the section on translational excitations, the row for z rotational excitations in the **Z** matrix also does not differ between InvSub and ImInvSub which explains the close similarities between these responses.

## 4.5 Discussion

In this section the possible flaws of the research are discussed which are divided in two categories: practical and theoretical.

### 4.5.1 Practical

For performing dynamic substructuring, one has to be very careful in conducting an experiment. Below are listed some common pitfalls in executing such an experiment of which most apply to this thesis.

#### Imperfect impacts

The impact hammer method is a beautiful and practical method to excite structure, however it is done by a human hand. This means that each impact is slightly different so usually an average of multiple impacts on the same location is used. Still this average can be different from the intended impact resulting in an inaccurate FRF. In this thesis great care is taken to make the impacts as accurate as possible by conducting the experiment in high concentration and checking the response coherence after every impact in the measuring software as seen in figure 4.19.

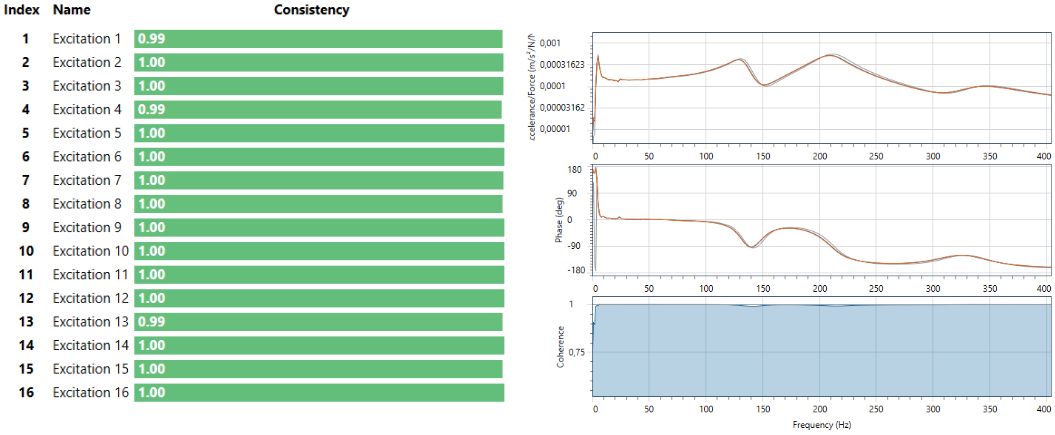

| Index | Name | Consistency |
|---|---|---|
| 1 | Excitation 1 | 0.99 |
| 2 | Excitation 2 | 1.00 |
| 3 | Excitation 3 | 1.00 |
| 4 | Excitation 4 | 0.99 |
| 5 | Excitation 5 | 1.00 |
| 6 | Excitation 6 | 1.00 |
| 7 | Excitation 7 | 1.00 |
| 8 | Excitation 8 | 1.00 |
| 9 | Excitation 9 | 1.00 |
| 10 | Excitation 10 | 1.00 |
| 11 | Excitation 11 | 1.00 |
| 12 | Excitation 12 | 1.00 |
| 13 | Excitation 13 | 0.99 |
| 14 | Excitation 14 | 1.00 |
| 15 | Excitation 15 | 1.00 |
| 16 | Excitation 16 | 1.00 |

FIGURE 4.19: Left: Consistency indicator of different for the VP transformation. Right: Example of two impacts on the same spot. The response quite similar indicating a consistent impact location

.

#### Imperfect sensor mounting

Similar to what is discussed in section 4.5.1, the mounting of sensors can also be inconsistent. If a sensor is used for the virtual point transformation, its exact location must be known. It can be however, that a sensor is not exactly placed on the desired location. To remedy this issue one can choose strategic mounting options. An example is to not place a sensor on the middle of a structure, but to line up the corners of a sensor with a structure to ensure it is placed precisely. This is not always a possibility but in this thesis it was put in to practice. The experiment was also conducted multiple times including re glueing the sensors. This method helps to place the sensor as close as possible to the same positions as previously used, however deviations are possible.

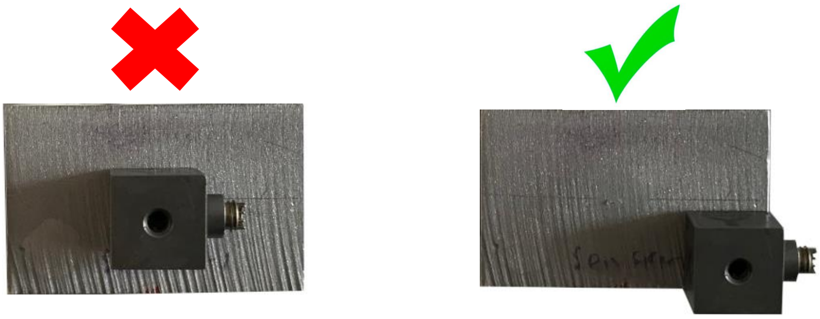

Figure 4.20: Left: A sensor placed in a location hard to measure accurately. Right: A sensor placed in a location that is easy to measure in relation to the component it is placed upon.

### Bookkeeping errors

Bookkeeping errors can always sneak in. If one has weak concentration during a measurement, one can connect the wrong cables to the wrong sensor or exert the wrong side of a symmetric structure or save impacts under the wrong index and so on. Humans make mistakes, but software can help to minimize these errors. For this thesis the in-house software Dirac is used the execute the measurement campaign. This revolutionary software in experimental dynamics has a built in 3d environment for visualizing impacts and sensors on the test structures and built in graphing tools to quality check the measurement which can indicate a bookkeeping error in an early stage.

### Physical connection between substructures

In this thesis, the connection between the substructures is assumed to be rigid while in the real world this might not be the case. Care has been taken to make this assumption as tight as possible however it can not be guarenteed. In this thesis the transmission simulators are connected to the rubber isolator with a bolted connection torqued down with a torquewrench to ensure consistend connection forces. Due to geometrical constraints the isolator is glued to the A-structure with X60 glue. This is a cold curing adhesive intended for strain gauge and other experimental applications.

### Stiffness of sensor mounting

Not only the physical connection between substructures is of importance, the connection between sensor and substructure also requires attention. Multiple methods of adhering a sensor to a substructure can be applied. For this thesis, three methods were considered:

1. 1. Using bee wax to directly mount the sensor to a substructure.
2. 2. Glueing a sensor mount of type 1 to the substructure and screwing the sensor on.
3. 3. Glueing a sensor mount of type 2 to the substructure and screwing the sensor on.

All methods have there advantages and disadvantages. For method 1 an advantage is that is quick and can be corrected easily if a sensor is misplaced. A disadvantage is that the sensor is easily displaced unintentionally. It is even a possibilty that a sensor moves slightly while it is unnoticed resulting in inaccurate measurements. Method two does not suffer from these disadvantages as it can be adhered very securely to the substructure with loctite or x60 adhesive. A disadvantage of this method is that the mount adds significant mass (and perhaps stiffness) to the assembly. A second disadvantage is that one needs to take into account the mounting offset in processing the measurement data. The third method is the method used in this thesis. In this method a mount is used, however this one is greatly reduced in size compared to method two as can be seen in figure 4.21. The advantage is less added mass and less offset from the assembly so it can be adhered close to a potential virtual point.

FIGURE 4.21: Left: A sensor mount of type 1. Right: A sensor mount of type 2, used in the measurement campaigns for this thesis

### Influence of sensor cables

The sensors are connected to the data acquisition device by cables which will add mass, stiffness and damping to a system. This will influence the response of the system. During an experiment cable management is an important consideration, not only for safety of the measuring equipment, but also for the results of the measurement campaign. It is best to attach the cable to a surrounding structure in a manner that it exerts the least force on the sensor and thereby on the structure. This is up to the interpretation of the executer of the experiment. In the case of this thesis a surrounding aluminium box from where the structures-to-be-measured where suspended provided suitable positions to adhere the sensor cables in a style that minimized the influence of measurement cables.

### Suspension of the object for testing

To do measurements on objects it needs to be decoupled from all surroundings called a free-free condition. The solution is suspending the test object from a suspension where the eigenfrequency of this system is not anywhere near the frequency range of interest. A rule of thumb is to suspend an object by creating a system that resonates around one Hertz in all directions, or atleast a factor of ten from the frequency region of interest. This is not always easily achieved and this suspension can add unwanted and unaccounted for stiffness and damping to a system.

## 4.5.2 Theoretical

### Virtual point: Sensor consistency

To perform the virtual point transformation one requires suitable sensor locations. This metric can be quantified in a value called the sensor consistency. This metric will take a value between zero and one. A one indicates that the sensor can describe the dynamics of the virtual point very well, while a zero means that it is not contributing to improving the dynamics of the virtual point. The sensor consistency is defined for every frequency point relating every sensor channel to every impact. During a measurement campaign it is possible to encounter low sensor consistency. This is mostly caused by incorrect sensor placement so the kinematics around the sensor are not compatible with the defined IDM matrices. Another problem can be that the interface between the sensors is flexible such that flexible deformations modes are present on the interface, while these are not defined in the IDM.

### Virtual point: Impact consistency

Not only the sensors need to be placed correctly around the virtual point but also the applied forces. This metric also takes value between 0 and 1. As can be seen in the left side of figure 4.19 the Dirac software can give live feedback on this number which makes executing a measurement campaign and especially the post processing less cumbersome.

### Virtual point: Rigid transformation matrices

For the virtual point transformation a rigid transformation from sensor location to the virtual point is used. This rigidity is an assumption and is not correct if there exist flexibility between sensors and the location of the virtual point. To remedy this the sensors must be placed close to the virtual point and the impacts must be exerted close to the virtual point to minimize the possibility of flexibility.

### Nonlinearity of the rubber material

The anaylsis in this thesis is conducted in the frequency domain but measurements are done in the time domain. To convert time domain signals to the frequency by a fourier transform one takes a harmonic load ot have a synchronous response. This poses assumptions on the measured structures, namely:

1. The structure is linear
2. The structure is time invariant
3. The structure is at steady state

Assumption two requires a structure to have steady **M**, **C** and **K** matrices which is not a problem. Assumption three requires that all transient effects have faded out which is also not a concern for this thesis. However assumption 1, linearity of the structure, can be a problem. The rubber material is not a linear material. However in appendix A the properties of this material is discussed and it can be concluded that for small displacements in this thesis linearity can be assumed.

### Repeating the experiment

A common practice in scientific research is to perform experiments multiple times to remove random errors. In this research random error sources can be sensor noise, environmental noise, roundoff errors in analog to digital conversion and the aforementioned misplaced sensors and impacts. Great care has been taken to minimize these random errors by already analyzing the measurement data while performing the measurement effectively doing the measurement already multiple times. To exclude even more uncontrollable factors it the same experiment can be repeated and compared.

### Signal to noise ratio for low frequencies

By nature of the used equipment the signal to noise ratio for frequencies below approximately 50 Hz can be insufficient [3]. A solution can be to assume that for this low frequencies the stiffness of the rubber is constant and perform an extrapolation from 50-100 Hz to the 0 to 50 Hz range as suggested by aforementioned literature. In this thesis the low frequent responses seem unaccurate till higher frequencies up to 200 Hz. An explanation for inaccuracies for low frequenct measurements can be found in the nature of the workings of an accelerometer. The used accelerometer is a PCB356 A32. This is a piezo-electric accelerometer in which a known mass is suspended and accelerations move the mass inside causing strain inside the measuring channels affecting electrical flow which is registered by the data acquisition system. This sensor construction is suitable for picking up changes in acceleration. Higher frequencies mean more changes means more data to measure. Assuming that noise is frequency independent, the signal to noise ratio is lower for lower frequencies which can even be too low to procuce accurate measurements.

### Matrix inversions on experimental data

For performing dynamic substructuring and inverse substructuring the inversion of FRF matrices is inevitable. As already discussed experimental data is highly likely to contain errors from different sources. Due to the nature of the mathematical operation of matrix inversion, even small random errors can be significantly enlarged in practices as substructure coupling and inverse substructuring. This is why great care is taken to get a clean as possible dataset (by practises discussed in this sectoin) before matrix inversions are performed. However it is assumed that an experimental dataset set is not perfected and errors by matrix inversions are enlarged in the final results.

### Different shapes of isolators

Not all isolators are beam-like shaped. In the case of this thesis a simple cylinder was used. As can be seen in figure 4.22 alternative shapes for isolators exist and can perhaps not be described by a stiffness matrix resembling a beam. For these shapes different stiffness matrices (which will not be as symmetric as a beam or cylinder matrix) should be used. It is very possible that by just assuming crosscouplings between translational and rotational DoFs will not be sufficient to improve the inverse substructuring method.

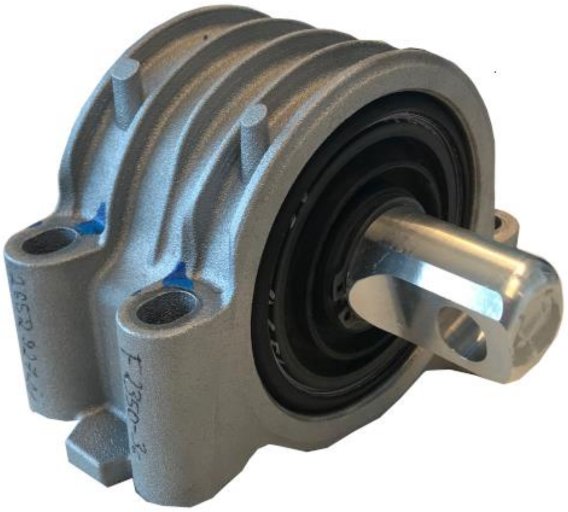

FIGURE 4.22: A differently shaped vibration isolator to which this thesis not applies.

# Chapter 5

# Conclusions

The goal of this thesis is to improve the method of Inverse Substructuring to make it suitable for use in practice. Therefore basic dynamics as changing system matrices and checking the influence is studied as well as more advanced concepts as Frequency Based Substructuring using Virtual Point Transformations and Inverse Substructuring. After this knowledgde was ammassed an educated proposition on improving the state-of-the-art concept of Inverse Substructuring could be made. This proposition of including crossoupling terms in the dynamic stiffness matrix based on the geometrical properties was carried out in a comprehensive experiment. From the results of this experiment two conclusions can be drawn:

1. Improved Inverse Substructuring does improve the prediction of coupled dynamics in most directions over Inverse Substructuring
2. ImInvSub can only be implemented with care

## 5.1 Improved Inverse Substructuring does improve the prediction of coupled dynamics in most directions over Inverse Substructuring

From theory one expects an improvement in prediction of dynamics by adding stiffness terms in the dynamic stiffness matrix by making use of the geometrical properties of the vibration isolator. The results in section 4.4 prove that by including expected crosscouplings between rotational x and translational y and vice versa does improve the prediction dynamics while not complicating the measurement procedure. Excitations in translational and rotational z direction do still produce overestimated accelerance results. This is attributed to the fact that the stiffness matrix chosen in this thesis does not alter the rows of z translation and rotation compared to Inverse Substructuring.

## 5.2 ImInvSub can only be implemented with care

The improvements of ImInvSub over InvSub are significant but a dynamicist should be hesitant with using this method in practice. Due to the nature of inverse substructuring and its matrix inversions, it is very possible to produce artifacial dynamics which are not present in the real structure. Also it can be seen in section 4.4 that some dynamics are not predicted. In general it can be stated that the Full Decoupling method will provide better results so the dynamicist should make the trade off decision between a simple and quick measurement with a possibility of inaccurate results and a more cumbersome procedure which is likely more accurate.

# Appendix A

# Properties and modelling of Rubber

## A.1 Properties and modelling of Rubber

To gain insight in the underlying physical processes that result in the dynamic properties, in this chapter the rubber material is researched and the key properties are dissected. It is key to know that rubber is not *one* material, but the name rubber is widely used to indicate a wide variety of materials used for different purposes. If rubber is mentioned in this document, a carbon black filled vulcanized rubber is assumed, suited for vibration damping. Usually the loading history of a rubber component can be split in two sections and this also applies to a vibration damper. The first section is a static preload. A part of an assembly or machine is 'resting' on the rubber vibration damper. Under this loading condition already some interesting phenomena appear such as the non-linear stress strain behaviour and stress relaxation. The second section of the loading history is of the dynamic kind. A damper experiences cyclic loads and attempts to dissipate the vibration energy. Rubber has excellent dynamic properties to achieve the desired result because of its viscoelastic behaviour.

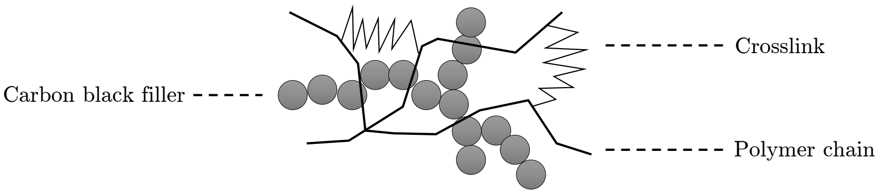

FIGURE A.1: Microstructure of carbon filled vulcanized rubber. The grey dots represent the carbon filler particles, the fat lines are polymer chains and the thin zigzag lines are crosslinks created by vulcanizing.

### A.1.1 A brief history

Rubber is produced from the sap of rubber trees in tropical climates. The famous explorer Columbus discovered ancient tribes in South and Central America using this exotic material and brought it to Europe where it caught the attention of scientists but was deemed not of any engineering value because of its poor mechanical properties. A few hundred years later, during the industrial revolution, this was all to change when Charles Goodyear discovered the process of vulcanization. Vulcanization is a the chemical process in which the natural rubber is heated with sulfur to form crosslinks between the rubber polymer chains. This operation creates a vastly more durable material that has good tensile strength, resilience, resistance to oxidation and solvents and it is useful in a broader temperature range. For nearly all engineering applications a rubber is not only vulcanized, but also a reinforcing filler is added. The filler particles create a physical and chemical bond with the polymer chains.

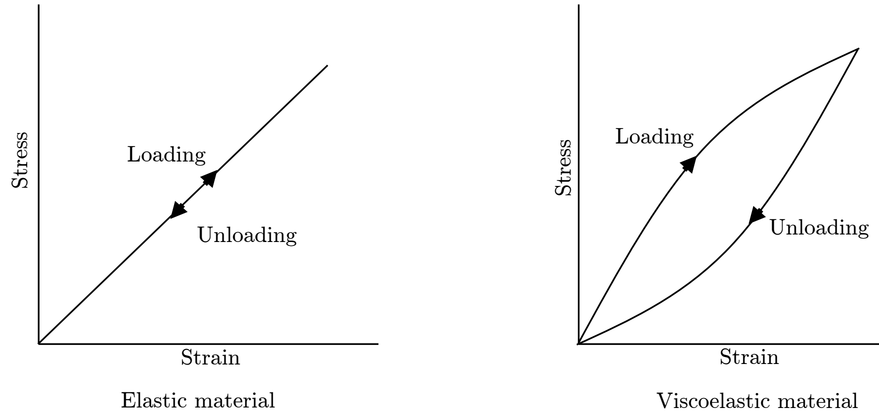

Figure A.2: The loading and unloading curve of an elastic and viscoelastic material

Different fillers can be used for different purposes as increasing stiffness, abrasion resistance or improved damping performance [14].

### A.1.2 Strain rate dependent stiffness

Rubber is a unique material in that it is both viscous and elastic. This so called viscoelastic material is a little trickier to understand than just elastic solids or viscous fluids. When undergoing deformation, an elastic material will return to its original shape when the load is removed. A viscous material resists strain with time when a stress is applied. It is interesting to compare the loading unloading curve of an elastic material and a viscoelastic material in figure A.2.

In the figure of the elastic material, the unloading part exactly matches the loading part. This means no energy is lost. The viscoelastic graph shows a difference in loading and unloading also known as a hysteresis loop. The area between the loading and unloading curve is energy lost as heat. In the case of rubber vibration damping this is excellent because the goal of a damper is the dissipation of (kinetic or potential) energy.

### A.1.3 Non linear stress-strain relation

A linear elastic model does not accurately describe the stress strain relation of rubber. As seen in section A.1.2 the stress and strain are time dependent, but their relation is also non linear. To model this non-linearity the concept of hyperelasticity is used. In the concept of hyperelasticity the concept of a strain energy density function is used. A strain energy density function is defined as the work that must be done on unit volume of the material in the reference state to deform it to the current configuration [6]. A strain energy density function can take many forms to suit the occasion. The most common approaches are discussed in section A.1.7.

### A.1.4 Effects of temperature and frequency

Temperature has a significant effect on the mechanical properties of rubber. Non-linear behaviour occurs at strain levels above certain thresholds. We have three regions in which the material will behave differently . The region of the lowest temperature is the glassy region. For rubber-like materials region is small, often below room temperature. In the glassy region the material is stiff and has a low energy loss under deformation. In the transition region,

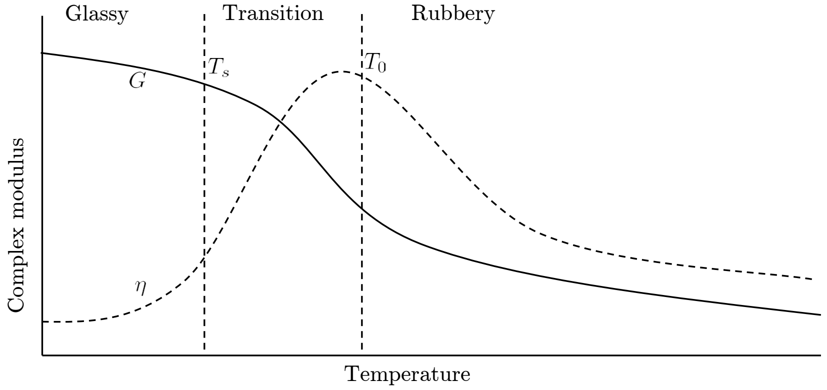

FIGURE A.3: The effect of temperature on complex modulus behaviour

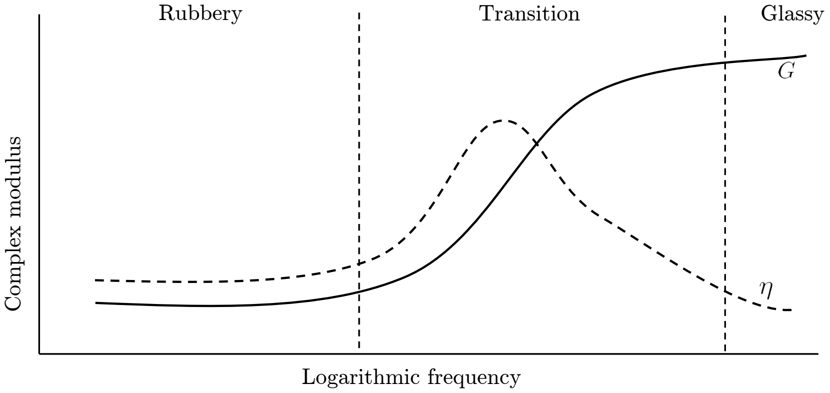

FIGURE A.4: The effect of frequency on complex modulus behaviour

the stiffness decreases rapidly en the energy loss increases to a maximum. At even higher temperatures, the stiffness decreases slowly just as the energy loss.

The effects of frequency are typically low for elastic solids. However for rubber-like materials the effects can be significant. In a way, it is the exact opposite of what the effect of temperature does. However, the effect of frequency occurs on a larger frequency scale.

### A.1.5 Stress softening

The stiffness of filled-rubber decreases with increasing displacement amplitude. There a two effects responsible for this property: the Mullins effect and the Payne effect [20]. The Mullins effect is the phenomenon in which when a rubber specimen is subjected to cyclic loading, the load required to produce a given stretch during the second loading cycle is smaller than that required to produce the same stretch during the primary loading cycle. [9]. The Mullins effect is dependent on the maximum previous strain. If the rubber specimen reaches a new maximum strain, the effect will take place again in this unreached region of strain. This effect is instantaneous and irreversible (or takes more than 24 hours to reverse).[7] The Payne effect is an other amplitude dependent non-linear stress softening property. The Payne effect describes decreasing stiffness with increasing strain amplitude and is attributed to the physical breaking of bonds in the filler of the rubber. In contrast to the Mullins effect, the Payne effect is reversible and is reversed in seconds.

### A.1.6 Viscoelastic models

In the following subsections the observed properties of rubber are incorporated in material models. For the static and dynamic modelling rubber a combination of two material models is required. To model the strain rate dependent stiffness and the effects of frequency (and temperature) a viscoelastic modelling approach is suitable. To include the non-linear stress-strain behaviour, hyperelastic properties are added.

As discussed in section A.1.2 of part **??**, rubber materials exhibit viscoelastic behaviour. In the nineteenth century there is a great expansion of effort on research on viscoelasticity. They discovered that rubber polymers that are homogeneous and isotropic have very similar behaviour compared to elastic materials. However, the behaviour changes drastically with temperature and somewhat with frequency, but the most important difference is that the damping levels in the rubber materials is much higher. This phenomenon is what makes the material suitable for vibration mitigation [6]. In this section several approaches for describing this somewhat complicated material behaviour are described.

#### The complex modulus model

A common way to describe the properties of rubber is in terms of a complex modulus first introduced by Myklestad [12]. If we know that in elastic materials the stress and strain occur in phase and in a viscous material this happens 90 degrees out of phase, and viscoelastic materials are a combination of the two, we can see that a viscoelastic behaviour is *somewhat* out of phase as shown in figure A.5.

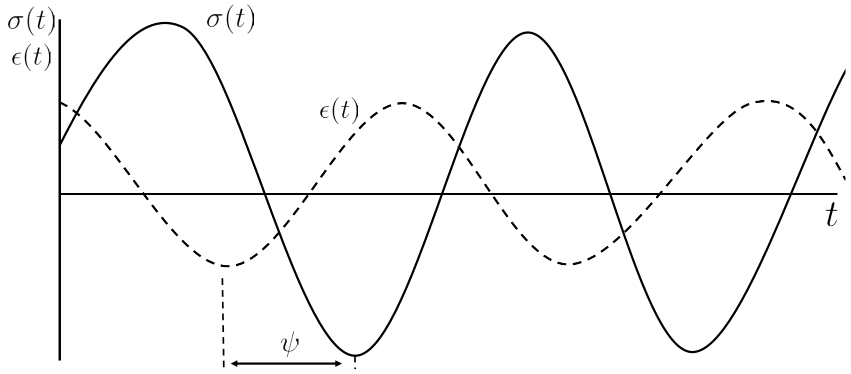

FIGURE A.5: Harmonic excitation and response of a viscoelastic solid

This behaviour can be described by combinations of $\sin \omega t$ and $\cos \omega t$. However when the problem gets complicated, for example in non-harmonic response, it is difficult to describe the problem using real numbers so in the complex modulus model a representation in terms of complex numbers is used. To convert the real sinusoids from the real to the complex number space equation A.1 is used:

$$\cos \omega t + i \sin \omega t = e^{i\omega t} \tag{A.1}$$

With this mathematical trick in mind, lets derive the equations for viscoelastic stresses in the complex modulus model. For an elastic solid we know the stress and shear stress are defined as:

$$\sigma = E\epsilon \quad \text{and} \quad \tau = G\phi \tag{A.2}$$

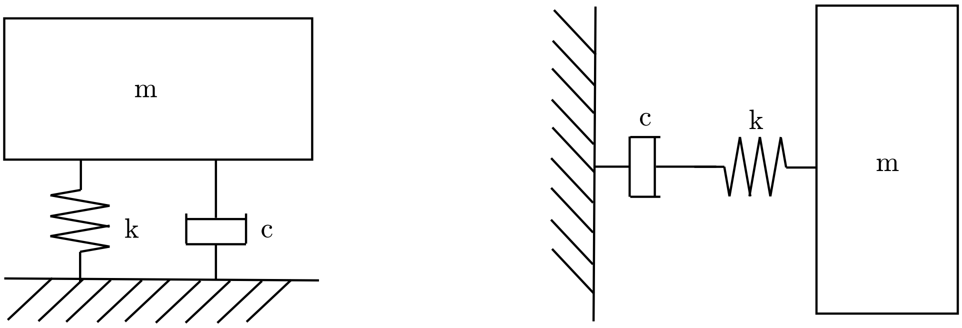

Maxwell element

Kelvin-Voigt element

FIGURE A.6: Configurations of springs and dashpots to represent viscoelasticity

Where $\sigma$ is the direct stress, $E$ is the Young's modulus, $\epsilon$ is the extensional strain, $\tau$ is the shear stress, $G$ is the shear modulus and $\phi$ is the shear strain. For rubber like materials, the equation A.2 is not as simple. As discussed in section A.1.2 a phase lag between stress and strain applies. This implies that a velocity dependent term should be present in the relationship. By incorporating this velocity term and rewrite our equations in the frequency domain we arrive at the final the following useful equations:

$$\sigma = E(1 + i\eta)\epsilon \quad \text{and} \quad \tau = G(1 + i\eta)\phi \tag{A.3}$$

In which $\eta$ is defined as the loss factor defined as the ratio of the imaginary and real part of the complex modulus. Equation A.3 represents the complex modulus form for extensional and shear deformation. it can be observed that we have three parameters: $G$, $E$ and $\eta$. These vary with temperature, frequency and differ from material to material.

A way to express the complex modulus is as follows:

$$G = G' + G'' \tag{A.4}$$

With:

$$G' = \frac{\sigma}{\epsilon}\cos\delta \quad \text{and} \quad G'' = \frac{\sigma}{\epsilon}\sin\delta \tag{A.5}$$

In which $G'$ represents the storage modulus and $G''$ represents the loss modulus.

### Spring-dash pot representation

Another common way to describe a viscoelastic material is to create a mechanical equivalent consisting of spring and dash pot elements. Depending on how these mechanical elements are arranged, the behaviour of the network changes. Three arrangements are highlighted: the Maxwell arrangement, the Kelvin-Voigt and the standard model.

In a Maxwell element (as depicted in figure A.6 the linear spring and linear dash pot are placed in series. The governing constitutive equation is thus a summation of the two elements:

$$\dot{\epsilon} = \frac{d\sigma}{Edt} + \frac{\sigma}{\eta} \tag{A.6}$$

With $E$ and $\eta$ are Young's modulus and the viscosity and $\sigma$ and $\epsilon$ are stress and strain. If a Maxwell element is put under a constant strain, the stresses gradually fade. Evenso, if the

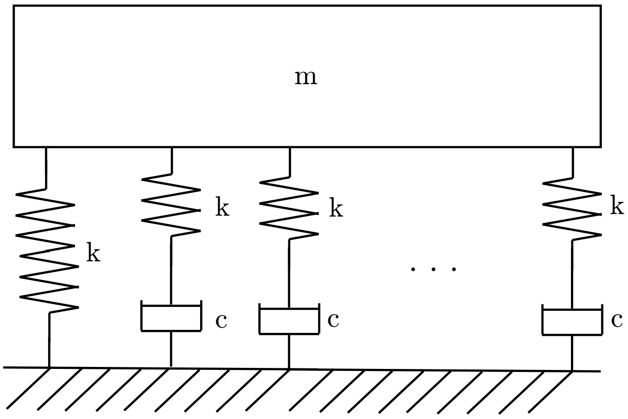

Figure A.7: Several Maxwell elements in parallel with a spring, also called a Generalized Maxwell model

Maxwell element is put under stress and the stress is released it will decay exponentially with time which corresponds somewhat to reality.

The Kelvin-Voigt model consists also of a spring and a dash pot, but now they are configured in parallel. This will show a constitutive equation:

$$\dot{\epsilon} = \frac{\sigma}{\eta} - E\frac{\epsilon}{\eta} \tag{A.7}$$

The Kelvin-Voigt approach is accurate for modelling creep behaviour at is predicts a strain gradually going to a value of $\sigma/E$ as time goes to infinity for a constant stress.

The standard model is a combination of a Maxwell element in parallel with a spring, combining the properties of the Maxwell and Kelvin-Voigt properties.

However, rubber materials show more complex behaviour than a standard model can predict. It is possible to create a more general model by placing several Maxwell elements in parallel as in figure. The stress response in this configuration is:

$$\sigma = E\epsilon - \sum_{i=1}^{N} E_i \epsilon_{vi} \tag{A.8}$$

### A.1.7 Hyperelastic models

In the event of large deformations the linear elastic model will not be accurate anymore as depicted in figure A.2. Hyperelastic material models use a strain energy density function to define the relationship between stress and strain. The strain energy density function (SEDF) is a function that relates the strain energy density of a material to the deformation gradient.

since the rubber engine mounting will not experience large deformations, it is unnecessary to include hyperelastic effects in an attempt to define dynamic properties.

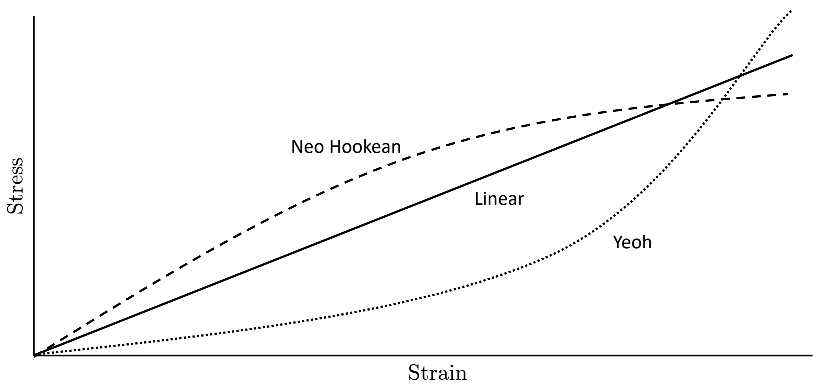

FIGURE A.8: Comparison of the stress-strain relationship two Hyperelastic models and a simple linear relationship

# Appendix B

# Construction of the 12x12 FRF matrix

To illustrate how one creates a 12x12 FRF matrix of a rubber isolator assembly, a finite element model is created in Ansys software. This assembly is exported to to Matlab and anaylzed using the VIBES.technology toolbox. Impacts are placed on the crosses and accelerations are measured by accelerometers as described in 2.3.1 and can be seen in figure 2.10. To fully describe the dynamics on the interfaces between $A$ and $I$ as well as $B$ and $I$, eight tri-axial accelerometers are used and 32 impacts are exerted resulting in the $24 \times 32$ matrix:

$$\mathbf{Y}^{AIB} = \begin{bmatrix} \mathbf{Y}_{1-1} & \mathbf{Y}_{1-2} & \mathbf{Y}_{1-3} & \dots & \dots & \mathbf{Y}_{1-32} \\ \mathbf{Y}_{1-1} & \ddots & & & & \\ \mathbf{Y}_{1-1} & & \ddots & & & \\ \mathbf{Y}_{2-1} & & & \ddots & & \\ \vdots & & & & \ddots & \\ \mathbf{Y}_{8-1} & \dots & \dots & \dots & \dots & \mathbf{Y}_{8-32} \end{bmatrix} \tag{B.1}$$

The values in this matrix are built up as follows. If one takes as an example $\mathbf{Y}_{a-b}$, $a$ indicates the sensor channel (for a tri-axial channel, a sensor contains three channels: one for each direction) and $b$ is the impact number.

As can be seen in figure 2.10, the accelerometers are placed nearby the interfaces between the substructures $A$, $I$ and $B$. The impacts are placed in a way that every direction of every accelerometer is excited to fill the whole matrix in equation B.1. The virtual points are created using the geometrical relation from the virtual point, the accelerometers and the impacts as described in section 2.3.2. From this measurement setup FRFs are created and transformed to virtual points using theory from section 2.3.2.

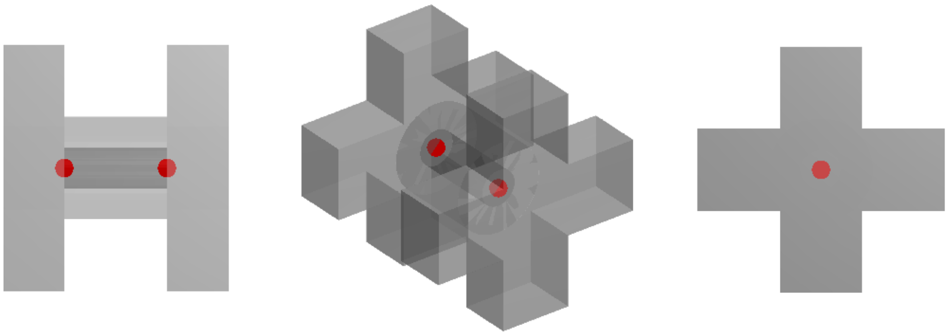

FIGURE B.1: Locations of the virtual points visualized as red dots. Left: Side view. Middle: Isometric view. Right: Top view.

In these Virtual Points (VPs) 6 DoFs are defined: three translational($x, y$ and $z$) and three rotational ($\theta_x, \theta_y$ and $\theta_z$). This results in a $12 \times 12$ virtual FRF matrix composed of four $6 \times 6$ matrices:

$$\mathbf{Y}^{11}_{\mathbf{qm}} = \begin{bmatrix} \mathbf{Y}^{11}_{x_1,x_1} & \mathbf{Y}^{11}_{y_1,x_1} & \mathbf{Y}^{11}_{z_1,x_1} & \mathbf{Y}^{11}_{\theta x_1,x_1} & \mathbf{Y}^{11}_{\theta y_1,x_1} & \mathbf{Y}^{11}_{\theta z_1,x_1} \\ \mathbf{Y}^{11}_{x_1,y_1} & \mathbf{Y}^{11}_{y_1,y_1} & \mathbf{Y}^{11}_{z_1,y_1} & \mathbf{Y}^{11}_{\theta x_1,y_1} & \mathbf{Y}^{11}_{\theta y_1,y_1} & \mathbf{Y}^{11}_{\theta z_1,y_1} \\ \mathbf{Y}^{11}_{x_1,z_1} & \mathbf{Y}^{11}_{y_1,z_1} & \mathbf{Y}^{11}_{z_1,z_1} & \mathbf{Y}^{11}_{\theta x_1,z_1} & \mathbf{Y}^{11}_{\theta y_1,z_1} & \mathbf{Y}^{11}_{\theta z_1,z_1} \\ \mathbf{Y}^{11}_{x_1,\theta x_1} & \mathbf{Y}^{11}_{y_1,\theta x_1} & \mathbf{Y}^{11}_{z_1,\theta x_1} & \mathbf{Y}^{11}_{\theta x_1,\theta x_1} & \mathbf{Y}^{11}_{\theta y_1,\theta x_1} & \mathbf{Y}^{11}_{\theta z_1,\theta x_1} \\ \mathbf{Y}^{11}_{x_1,\theta y_1} & \mathbf{Y}^{11}_{y_1,\theta y_1} & \mathbf{Y}^{11}_{z_1,\theta y_1} & \mathbf{Y}^{11}_{\theta x_1,\theta y_1} & \mathbf{Y}^{11}_{\theta y_1,\theta y_1} & \mathbf{Y}^{11}_{\theta z_1,\theta y_1} \\ \mathbf{Y}^{11}_{x_1,\theta z_1} & \mathbf{Y}^{11}_{y_1,\theta z_1} & \mathbf{Y}^{11}_{z_1,\theta z_1} & \mathbf{Y}^{11}_{\theta x_1,\theta z_1} & \mathbf{Y}^{11}_{\theta y_1,\theta z_1} & \mathbf{Y}^{11}_{\theta z_1,\theta z_1} \end{bmatrix} \tag{B.2}$$

$$\mathbf{Y}^{12}_{\mathbf{qm}} = \begin{bmatrix} \mathbf{Y}^{12}_{x_1,x_2} & \mathbf{Y}^{12}_{y_1,x_2} & \mathbf{Y}^{12}_{z_1,x_2} & \mathbf{Y}^{12}_{\theta x_1,x_2} & \mathbf{Y}^{12}_{\theta y_1,x_2} & \mathbf{Y}^{12}_{\theta z_1,x_2} \\ \mathbf{Y}^{12}_{x_1,y_2} & \mathbf{Y}^{12}_{y_1,y_2} & \mathbf{Y}^{12}_{z_1,y_2} & \mathbf{Y}^{12}_{\theta x_1,y_2} & \mathbf{Y}^{12}_{\theta y_1,y_2} & \mathbf{Y}^{12}_{\theta z_1,y_2} \\ \mathbf{Y}^{12}_{x_1,z_2} & \mathbf{Y}^{12}_{y_1,z_2} & \mathbf{Y}^{12}_{z_1,z_2} & \mathbf{Y}^{12}_{\theta x_1,z_2} & \mathbf{Y}^{12}_{\theta y_1,z_2} & \mathbf{Y}^{12}_{\theta z_1,z_2} \\ \mathbf{Y}^{12}_{x_1,\theta x_2} & \mathbf{Y}^{12}_{y_1,\theta x_2} & \mathbf{Y}^{12}_{z_1,\theta x_2} & \mathbf{Y}^{12}_{\theta x_1,\theta x_2} & \mathbf{Y}^{12}_{\theta y_1,\theta x_2} & \mathbf{Y}^{12}_{\theta z_1,\theta x_2} \\ \mathbf{Y}^{12}_{x_1,\theta y_2} & \mathbf{Y}^{12}_{y_1,\theta y_2} & \mathbf{Y}^{12}_{z_1,\theta y_2} & \mathbf{Y}^{12}_{\theta x_1,\theta y_2} & \mathbf{Y}^{12}_{\theta y_1,\theta y_2} & \mathbf{Y}^{12}_{\theta z_1,\theta y_2} \\ \mathbf{Y}^{12}_{x_1,\theta z_2} & \mathbf{Y}^{12}_{y_1,\theta z_2} & \mathbf{Y}^{12}_{z_1,\theta z_2} & \mathbf{Y}^{12}_{\theta x_1,\theta z_2} & \mathbf{Y}^{12}_{\theta y_1,\theta z_2} & \mathbf{Y}^{12}_{\theta z_1,\theta z_2} \end{bmatrix} \tag{B.3}$$

$$\mathbf{Y}^{21}_{\mathbf{qm}} = \begin{bmatrix} \mathbf{Y}^{21}_{x_2,x_1} & \mathbf{Y}^{21}_{y_2,x_1} & \mathbf{Y}^{21}_{z_2,x_1} & \mathbf{Y}^{21}_{\theta x_2,x_1} & \mathbf{Y}^{21}_{\theta y_2,x_1} & \mathbf{Y}^{21}_{\theta z_2,x_1} \\ \mathbf{Y}^{21}_{x_2,y_1} & \mathbf{Y}^{21}_{y_2,y_1} & \mathbf{Y}^{21}_{z_2,y_1} & \mathbf{Y}^{21}_{\theta x_2,y_1} & \mathbf{Y}^{21}_{\theta y_2,y_1} & \mathbf{Y}^{21}_{\theta z_2,y_1} \\ \mathbf{Y}^{21}_{x_2,z_1} & \mathbf{Y}^{21}_{y_2,z_1} & \mathbf{Y}^{21}_{z_2,z_1} & \mathbf{Y}^{21}_{\theta x_2,z_1} & \mathbf{Y}^{21}_{\theta y_2,z_1} & \mathbf{Y}^{21}_{\theta z_2,z_1} \\ \mathbf{Y}^{21}_{x_2,\theta x_1} & \mathbf{Y}^{21}_{y_2,\theta x_1} & \mathbf{Y}^{21}_{z_2,\theta x_1} & \mathbf{Y}^{21}_{\theta x_2,\theta x_1} & \mathbf{Y}^{21}_{\theta y_2,\theta x_1} & \mathbf{Y}^{21}_{\theta z_2,\theta x_1} \\ \mathbf{Y}^{21}_{x_2,\theta y_1} & \mathbf{Y}^{21}_{y_2,\theta y_1} & \mathbf{Y}^{21}_{z_2,\theta y_1} & \mathbf{Y}^{21}_{\theta x_2,\theta y_1} & \mathbf{Y}^{21}_{\theta y_2,\theta y_1} & \mathbf{Y}^{21}_{\theta z_2,\theta y_1} \\ \mathbf{Y}^{21}_{x_2,\theta z_1} & \mathbf{Y}^{21}_{y_2,\theta z_1} & \mathbf{Y}^{21}_{z_2,\theta z_1} & \mathbf{Y}^{21}_{\theta x_2,\theta z_1} & \mathbf{Y}^{21}_{\theta y_2,\theta z_1} & \mathbf{Y}^{21}_{\theta z_2,\theta z_1} \end{bmatrix} \tag{B.4}$$

$$\mathbf{Y}^{22}_{\mathbf{qm}} = \begin{bmatrix} \mathbf{Y}^{22}_{x_2,x_2} & \mathbf{Y}^{22}_{y_2,x_2} & \mathbf{Y}^{22}_{z_2,x_2} & \mathbf{Y}^{22}_{\theta x_2,x_2} & \mathbf{Y}^{22}_{\theta y_2,x_2} & \mathbf{Y}^{22}_{\theta z_2,x_2} \\ \mathbf{Y}^{22}_{x_2,y_2} & \mathbf{Y}^{22}_{y_2,y_2} & \mathbf{Y}^{22}_{z_2,y_2} & \mathbf{Y}^{22}_{\theta x_2,y_2} & \mathbf{Y}^{22}_{\theta y_2,y_2} & \mathbf{Y}^{22}_{\theta z_2,y_2} \\ \mathbf{Y}^{22}_{x_2,z_2} & \mathbf{Y}^{22}_{y_2,z_2} & \mathbf{Y}^{22}_{z_2,z_2} & \mathbf{Y}^{22}_{\theta x_2,z_2} & \mathbf{Y}^{22}_{\theta y_2,z_2} & \mathbf{Y}^{22}_{\theta z_2,z_2} \\ \mathbf{Y}^{22}_{x_2,\theta x_2} & \mathbf{Y}^{22}_{y_2,\theta x_2} & \mathbf{Y}^{22}_{z_2,\theta x_2} & \mathbf{Y}^{22}_{\theta x_2,\theta x_2} & \mathbf{Y}^{22}_{\theta y_2,\theta x_2} & \mathbf{Y}^{22}_{\theta z_2,\theta x_2} \\ \mathbf{Y}^{22}_{x_2,\theta y_2} & \mathbf{Y}^{22}_{y_2,\theta y_2} & \mathbf{Y}^{22}_{z_2,\theta y_2} & \mathbf{Y}^{22}_{\theta x_2,\theta y_2} & \mathbf{Y}^{22}_{\theta y_2,\theta y_2} & \mathbf{Y}^{22}_{\theta z_2,\theta y_2} \\ \mathbf{Y}^{22}_{x_2,\theta z_2} & \mathbf{Y}^{22}_{y_2,\theta z_2} & \mathbf{Y}^{22}_{z_2,\theta z_2} & \mathbf{Y}^{22}_{\theta x_2,\theta z_2} & \mathbf{Y}^{22}_{\theta y_2,\theta z_2} & \mathbf{Y}^{22}_{\theta z_2,\theta z_2} \end{bmatrix} \tag{B.5}$$

In these matrices a value is built up as follows. If one takes as an example $\mathbf{Y}^{12}_{x_1,\theta y_2}$, the superscript $^{1}2$ indicates the frequency response from virtual point 1 to 2 and the subscript $_{x_1,\theta y_2}$ resembles an excitement in $x$ direction on virtual point 1, and the rotational response around the $y$ axis in virtual point 2. $q$ and $m$ are the generalized forces and displacements respectively. These four matrices from equations B.2-B.5 assemble to one FRF matrix:

$$\mathbf{Y}_{\mathbf{qm}} = \begin{bmatrix} \mathbf{Y}^{11}_{\mathbf{qm}} & \mathbf{Y}^{12}_{\mathbf{qm}} \\ \mathbf{Y}^{21}_{\mathbf{qm}} & \mathbf{Y}^{22}_{\mathbf{qm}} \end{bmatrix} \tag{B.6}$$

From here on the generalized forces and displacements notation is omitted for readability. By inverting the virtual point FRFs, the dynamic stiffness between and in the virtual points are obtained following $\mathbf{Y}^{-1} = \mathbf{Z}$:

$$\begin{bmatrix} \mathbf{Y}_{11} & \mathbf{Y}_{12} \\ \mathbf{Y}_{21} & \mathbf{Y}_{22} \end{bmatrix}^{-1} = \begin{bmatrix} \mathbf{Z}_{11} & \mathbf{Z}_{12} \\ \mathbf{Z}_{21} & \mathbf{Z}_{22} \end{bmatrix} = \begin{bmatrix} \mathbf{Z}^{A}_{11} + \mathbf{Z}^{I}_{11} & \mathbf{Z}^{I}_{12} \\ \mathbf{Z}^{I}_{21} & \mathbf{Z}^{B}_{22} + \mathbf{Z}^{I}_{22} \end{bmatrix} = \mathbf{Z}^{AIB} \tag{B.7}$$

With the dynamic stiffness of the structure now obtained, one can compare different methods for obtaining the dynamic stiffness of the isolator. As shown in section 2.4, one can decouple the dynamics of cross $A$ and $B$ as:

$$\begin{bmatrix} \mathbf{Z}^A_{11} + \mathbf{Z}^I_{11} & \mathbf{Z}^I_{12} \\ \mathbf{Z}^I_{21} & \mathbf{Z}^B_{22} + \mathbf{Z}^I_{22} \end{bmatrix} - \begin{bmatrix} \mathbf{Z}^A_{11} & 0 \\ 0 & \mathbf{Z}^B_{22} \end{bmatrix} = \begin{bmatrix} \mathbf{Z}^I_{11} & \mathbf{Z}^I_{12} \\ \mathbf{Z}^I_{21} & \mathbf{Z}^I_{22} \end{bmatrix} = \mathbf{Z}^I \tag{B.8}$$

Because this decoupling procedure is done virtually, the experiment is conducted perfectly. There are no misplaced excitations or measurement errors and noise. Therefore the dynamic stiffness of $A$ and $B$ can be determined and decoupled perfectly. This full decoupling method results are therefore suited as validation.

# Bibliography

[1] G. M.L. Gladwell. “Branch mode analysis of vibrating systems”. In: *Journal of Sound and Vibration* 1.1 (1964), pp. 41–59. ISSN: 10958568. DOI: `10.1016/0022-460X(64)90006-9`.

[2] M Haeussler, S Klaassen, and D J Rixen. “Comparison of Substructuring based techniques for dynamic property identification of rubber isolators”. In: (), p. 1.

[3] M Haeussler, S W B Klaassen, and D J Rixen. “Experimental models for rubber isolator elements in substructuring assemblies Experimental modeling”. In: ().

[4] Michael Haeussler and Daniel J. Rixen. “Optimal transformation of frequency response functions on interface deformation modes”. In: *Dynamics of Coupled Structures, Volume 4. Conference Proceedings of the Society for Experimental Mechanics Series* (2017), pp. 225–237.

[5] Bjorn Jetmundsen, Richard L. Bielawa, and William G. Flannelly. *Generalized Frequency Domain Substructure Synthesis*. Vol. 33. 1988, pp. 55–64. DOI: `10.4050/JAHS.33.55`.

[6] David Jones. *Handbook of viscoelastic vibration damping*. 2001. DOI: `ISBN047149248`.

[7] Fredrik Karlsson and Anders Persson. “Modelling non-linear dynamics of rubber bushings - Parameter Identification and validation”. In: (2003). ISSN: 0281-6679. DOI: `6679`.

[8] D. De Klerk, D. J. Rixen, and S. N. Voormeeren. “General Framework for Dynamic Substructuring: History, Review and Classification of Techniques”. In: *AIAA Journal* 46.5 (2008), pp. 1169–1181. ISSN: 0001-1452. DOI: `10.2514/1.33274`. URL: `http://arc.aiaa.org/doi/10.2514/1.33274`.

[9] Shankar Krishnaswamy and Millard F. Beatty. “Mullins effect in compressible solids”. In: *International Journal of Engineering Science* 38.13 (2000), pp. 1397–1414. ISSN: 00207225. DOI: `10.1016/S0020-7225(99)00125-1`.

[10] Kenneth G Mcconnell. “The Elusive Free-Free Boundary Condition by”. In: ().

[11] L. Nieuwenhuijse. “Robust Experimental Dynamic Substructuring: Enhanced quality indicators & Application of SEMM to an Industrial Case”. PhD thesis. Delft, University of Technology, 2018.

[12] NO Myklestad. “The concept of complex damping”. In: *Journal of applied mechanics* 19.3 (1952), pp. 284–286.

[13] J C O’CALLAHAN. “System Equivalent Reduction Expansion Process”. In: *Proc. of the 7th Inter. Modal Analysis Conf., 1989* (1989). URL: `https://ci.nii.ac.jp/naid/10015640027/en/`.

[14] Anders K Olsson. *Finite Element Procedures in Modelling the Dynamic Properties of Rubber*. 2007. ISBN: 9789162871307.

[15] Lu Ean Ooi and Zaidi Mohd Ripin. “Dynamic stiffness and loss factor measurement of engine rubber mount by impact test”. In: *Materials and Design* 32.4 (2011), pp. 1880–1887. ISSN: 02641275. DOI: `10.1016/j.matdes.2010.12.015`. URL: `http://dx.doi.org/10.1016/j.matdes.2010.12.015`.

[16] Daniel J. Rixen. “Engineering Dynamics - Lecture Notes”. In: (2008), p. 146. URL: http://medcontent.metapress.com/index/A65RM03P4874243N.pdf.

[17] R.P. Hoogeboom. “Department of Precision and Microsystems Engineering”. In: (2016), pp. 5–7.

[18] H A Schwarz. *Gesammelte mathematische Abhandlungen von H.A. Schwarz Bd. 1, 2. TT - LK*. Duits. Berlin: Springer.

[19] M. van der Seijs et al. “an Improved Methodology for the Virtual Point Transformation of Measured Frequency Response Functions in Dynamic Substructuring”. In: *Proceedings of the 4th International Conference on Computational Methods in Structural Dynamics and Earthquake Engineering (COMPDYN 2013)* June (2014), pp. 4334–4347. DOI: 10.7712/120113.4816.C1539. URL: http://www.eccomasproceedia.org/conferences/thematic-conferences/compdyn-2013/4816.

[20] Mattias Sjöberg. “On dynamic properties of rubber isolators”. In: (2002). URL: http://www.diva-portal.org/smash/record.jsf?pid=diva2:9268{\&}dswid=-778.

[21] Barry F Smith, Petter E Bjørstad, and William. Gropp. *Domain decomposition : parallel multilevel methods for elliptic partial differential equations TT -*. Engels. Cambridge ; Cambridge University Press, ISBN: 052149589X 9780521495899. URL: http://catdir.loc.gov/catdir/toc/cam023/95042362.html.

[22] D. J. Thompson, W. J. Van Vliet, and J. W. Verheij. “Developments of the indirect method for measuring the high frequency dynamic stiffness of resilient elements”. In: *Journal of Sound and Vibration* 213.1 (1998), pp. 169–188. ISSN: 0022460X. DOI: 10.1006/jsvi.1998.1492.